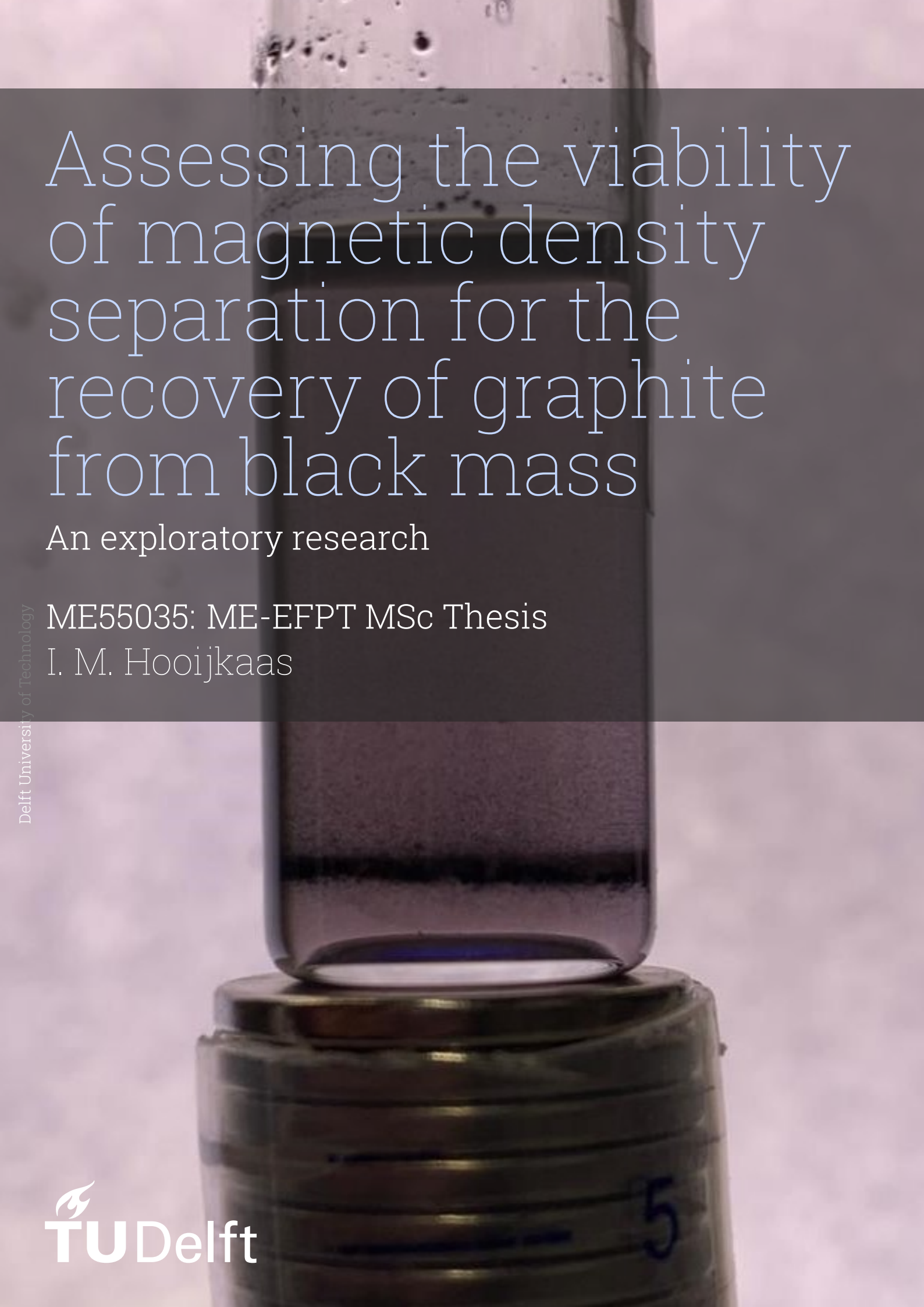

Assessing the viability of magnetic density separation for the recovery of graphite from black mass

An exploratory research

ME55035: ME-EFPT MSc Thesis

I. M. Hooijkaas

Delft University of Technology

TU Delft

Assessing the viability of magnetic density separation for the recovery of graphite from black mass

An exploratory research

by

I. M. Hooijkaas

Master Thesis

in partial fulfilment of the requirements for the degree of

Master of Science

in Mechanical Engineering

at the Department Process & Energy of Faculty Mechanical Engineering of Delft University of Technology
to be defended publicly on November 19, 2024 at 9:30 AM.

Student number:	4747925	
MSc Track:	Energy, Flow & Process Technology	
Version:	November 4, 2024	
Project duration:	March, 2024 – November, 2024	
Thesis committee:	dr. L. Botto,	TU Delft, Chair
	dr.ir. W.P. Breugem	TU Delft, Committee member
	dr. H.B. Eral	TU Delft, Committee member
	dr.ir. N. Valle Marchante	TU Delft, Committee member
	J.J.M.M. van de Ven MSc	TU Delft, Committee member
Cover:	Magnetic Levitation of anodic graphite powder in a $MnCl_2$ solution.	

An electronic version of this thesis is available at http://repository.tudelft.nl/.

TU Delft

Preface

Before you lies my thesis ”Assessing the viability of magnetic density separation for the recovery of graphite from black mass”, submitted in fulfillment of the requirements for the master’s degree in Mechanical Engineering at Delft University of Technology. This exciting topic was proposed by my supervisor, Lorenzo Botto. From the outset, I was encouraged to explore many challenges related to the battery materials and separation method, pulling me out of my comfort zone. As the experimental setup took shape, Lorenzo guided me in ensuring the reliability and repeatability of my work. Thanks to his valuable insights and our productive discussions, I am very pleased with the results I was able to conceive.

I would like to thank Suriya and Maurice from Lorenzo’s research group for their guidance in the lab. They were not only consistently available to help with the experimental setup, but also ready with words of encouragement whenever I encountered a setback. Additionally, I would like to thank Joep from the Materials Science and Engineering department, who was always available to help me with the chemical issues I faced. It has been very fascinating to watch him literally dissolve my problems before my eyes.

Last but not least, I would like to thank my boyfriend, family, and friends for their unwavering support and encouragement, and for helping me unwind and clear my mind whenever I needed a break from the project.

I. M. Hooijkaas
Delft, November 2024

Abstract

The demand of the lithium ion battery (LIB) is increasing exponentially, as it is the state-of-the-art solution to achieve electrification of the mobility sector and to ensure the stability of the electricity grid. The anode and cathode of these batteries consist of graphite and a lithium transition metal oxide (LTMO), respectively, which have both been designated as critical raw materials and face serious supply risks. At present, only a small amount of cathode material can be recovered through chemical separation processes, which are expensive and energy-intensive and produce a lot of waste. Direct physical recycling of these materials is a far more efficient approach, but no scalable direct recycling routes are currently available. Sink-float separation using dense media had been successfully performed, indicating that density is a suitable differentiating property. However, dense media are associated with serious drawbacks due to their high viscosity, toxicity and cost, making them unsuitable for large-scale application. Therefore, the objective of this research is to evaluate whether magnetic density separation (MDS), which applies a magnetic liquid subjected to a magnetic field to create an artificial density gradient within the liquid, can be applied in practice for the separation between anode and cathode materials from spent LIBs. This is achieved through magnetic field simulations, developing and executing a method for measuring the magnetic susceptibility, and Magnetic Levitation (MagLev) experiments.

Following from the magnetic field simulations, an array of permanent disc magnets, stacked into one larger cylindrical magnet, was selected as the optimal magnetic configuration. Further, samples of paramagnetic $MnCl_2$ solutions were prepared at different concentrations, up to the saturation concentration. Their densities and magnetic susceptibilities had to be determined in order to be able to estimate the achievable apparent densities. From the literature it became clear that the magnetic susceptibility is a property that cannot be easily measured and a very wide range of values was used by different sources. Because of this, a new method was developed to measure the magnetic susceptibility of a liquid: the magnetic pendant drop method. The deformation of the drop was studied as it was brought into proximity of the magnets. The results from this experiment were of the same order of magnitude as the reported magnetic susceptibilities found from the literature, which were quite dispersed.

Finally, MagLev experiments were performed with anode and cathode materials. The cathode material sunk to the bottom for each concentration. On the other hand, MagLev of anode material was achieved in samples of high $MnCl_2$ concentration. From their levitation heights, the magnetic susceptibility was once again calculated, and was even closer to the value reported in one of the sources. The equilibrium height at which the anode material levitated was at approximately 6 mm above the magnet's surface. This means that careful design considerations will need to be taken in the design of a continuous process, and possibly a different option of magnets and paramagnetic medium should be selected. Nonetheless, the fact that levitation of graphite can be achieved, offers a positive prospect for separation by MDS on lab-scale.

Contents

Nomenclature

AAM anode active material
BM black mass
CAM cathode active material
FF froth flotation
ICP-OES inductively coupled plasma-optical emission spectrometry
IFT interfacial tension
LCO lithium cobalt oxide, $LiCoO_2$
LFP lithium iron phosphate, $LiFePO_4$
LIB lithium ion battery
LMO lithium manganese oxide, $LiMn_2O_4$
LTMO lithium transition metal oxide
MagLev Magnetic Levitation
MDS magnetic density separation
MRI magnetic resonance imaging
NCA lithium nickel cobalt aluminium oxides, $LiNi_{1-x-y}Co_xAl_yO_2$
NMA lithium nickel manganese aluminium oxide, $LiNi_{1-x-y}Mn_xAl_yO_2$
NMC lithium nickel manganese cobalt oxide, $LiNi_{1-x-y}Mn_xCo_yO_2$
NMP n-methyl pyrrolidone
PVDF polyvinylidene fluoride
SEM scanning electron microscope
XRD X-ray diffraction
XRF X-ray fluorescence

List of Variables

Symbol	Definition	Unit
$\overrightarrow{B}$	Magnetic flux density	[T]
$(\overrightarrow{B} \cdot \overrightarrow{\nabla})\overrightarrow{B}$	Gradient magnetic field intensity	$[\mathrm{T^2\,m^{-1}}]$
$\overrightarrow{F_g}$	Force of gravity	[mN]
$\overrightarrow{F_{\mathrm{mag}}}$	Magnetic force	[mN]
$\overrightarrow{g}$	Gravitational constant	$9.81\,\mathrm{m\,s^{-2}}$
V	Volume	$[\mathrm{mm^3}]$
μ_0	Vacuum permeability	$4\pi \cdot 10^{-7}\mathrm{N\,A^{-2}}$
ρ_m	Density of paramagnetic medium	$[\mathrm{g\,cm^{-3}}]$
ρ_s	Density of suspended particle	$[\mathrm{g\,cm^{-3}}]$
χ_m	Magnetic susceptibility of paramagnetic medium	[–]
χ_s	Magnetic susceptibility of suspended particle	[–]
F_{IFT}	Surface tension force	[mN]
R_x	Radius of curvature on drop surface	[mm]
V_d	Drop volume	$[\mathrm{mm^3}]$
γ	Interfacial tension	$[\mathrm{mN\,m^{-1}}]$
Bo	Bond number	[–]
$\mathrm{Bo_{mag}}$	Magnetic Bond number	[–]

List of Figures

List of Tables

1

Introduction

1.1. Motivation

The lithium ion battery (LIB) is the state-of-the-art technology of electrochemical energy storage, due to its low self-discharge rate, high rate capacity, high cycling capacity, high energy density and long life time, and are being applied for portable electronic devices, for stationary energy storage systems, and more recently for electrical vehicles. Figure 1.1 shows the tremendous increase in demand of automotive LIBs over the past years. Overall, a five-fold increase in global battery consumption was predicted between 2020 and 2030 [65, 90] and in the following two decades an increase of at least 12 times is expected [23, 71].

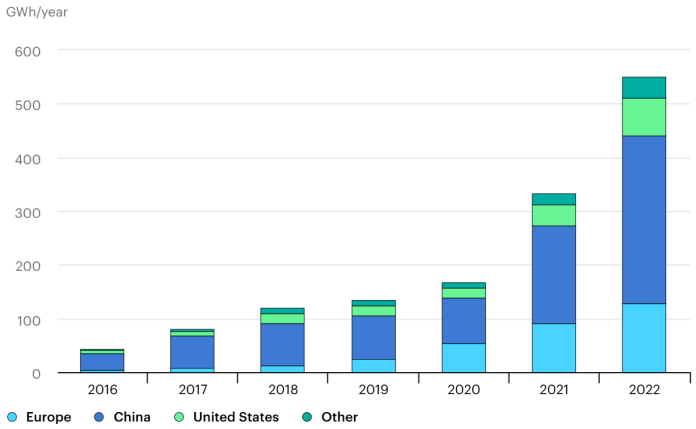

Figure 1.1: Automotive battery demand by region, 2016-2022. Reprinted from the International Energy Agency [1].

As a result of the increase in LIB demand, the demand for the raw materials from which batteries are produced is also increasing. For the cathode, there exists a large number of lithium transition metal oxides (LTMOs) that can be used. In contrast, there is only one option for the anode material: graphite [4, 53]. The supply of graphite could potentially become at risk as no graphite is produced in Europe. Figure 1.2 displays the global natural graphite production distribution. It can be observed that 62% of the graphite used, is imported from China. Even more so, 90% of all spherical graphite produced, which is the required form of graphite for LIBs, originates from China [76, 77]. Due to new regulations, export of graphite from China has become government-controlled since December 2023 [8, 22].

Lithium (Li), Cobalt (Co) and Nickel (Ni) have previously been designated as critical raw materials and strategic elements in the UK, EU and US, but more recently also graphite (C) has been designated as a critical raw material. While graphite is not the most expensive or scarce material, it does face major risks in resource security, due to geographical and geopolitical factors [3, 23, 72].

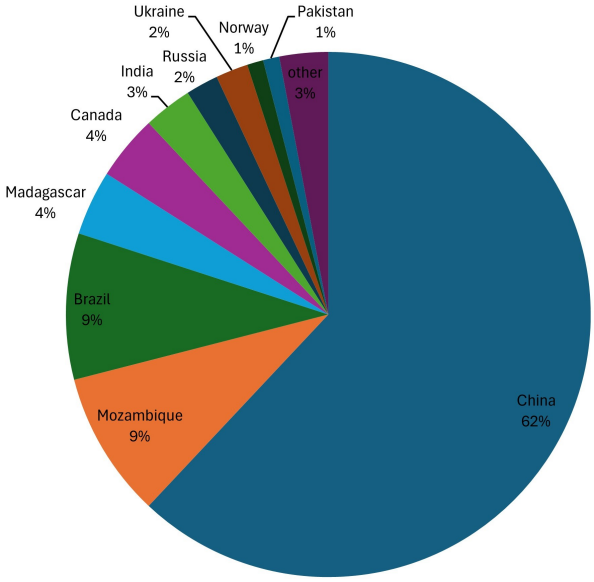

Figure 1.2: Natural Graphite production distribution by country in 2019, the total amount about 1 130 000 tons. Reproduced from Abdollahifar et al. [3].

On the other hand, the waste streams of spent LIBs is also increasing. End-of-life LIBs are most commonly found in one of the following three destinations: municipal solid waste landfill, waste-to-energy facilities and specialized recycling facilities. In 2016 95% of all LIBs still ended up in landfill sites, and still only 5% of LIBs were recycled in the EU in 2019 [72]. Current recycling methods are very energy and cost-intensive, and are thus only aimed towards the recovery of certain transition metals from the cathode, since these are most valuable.

However, as graphite is the common denominator among all battery chemistries, it makes sense to develop a separation method focused on the extraction of graphite, instead of separation methods geared towards recovering materials for one specific cathode chemistry. Further, by removing the graphite at an earlier stage, inflow of the energy-intensive extraction methods for recovering the cathode material can be strongly diminished, resulting in lower cost, reagent and energy consumption, waste generation and greenhouse gas emissions [49].

In order to ensure there is sufficient graphite available to meet future demand for the production of LIBs, and to not be dependent on foreign supply of this material, the strategy proposed for this research is the direct recycling of graphite from spent LIBs. The objective of this research is to improve the recycling of graphite from LIBs.

1.2. Literature review

A literature review was conducted to identify the materials which need to be separated from the spent LIBs, what separation methods for direct recycling of two solid, micron-sized materials are available, and what their opportunities and limitations are.

1.2.1. Overview of black mass materials

The material that remains from spent LIBs, once most other components have been extracted, consists of a mixture of anode active material (AAM) and cathode active material (CAM), commonly referred to as black mass (BM). In order to find a selective separation method that distinguishes between these two materials, it is important to understand which materials are contained in both active materials and what their properties are.

For the negative electrode, graphite is used as AAM and coated onto a current collector of copper (Cu, $6-10\mu m$) [38, 78]. Before being suitable for use in LIBs, the natural flake graphite need to be rolled into a spheroidal shape by mechanical methods. After this, the final product is a 'potato'-shaped particle with a purity above 99.9 wt.% carbon, referred to as spheroidal graphite [4, 53, 74].

Spheroidized graphite particles allow for fast and extensive lithium intercalation, enhancing the electrochemical performance of the material [53, 55, 59]. A narrow particle size distribution of approximately $8-30\mu m$ is desired for optimal performance. Figure 1.3 shows SEM images of natural flake graphite before and after spheroidization, and a schematic view of the altered structure.

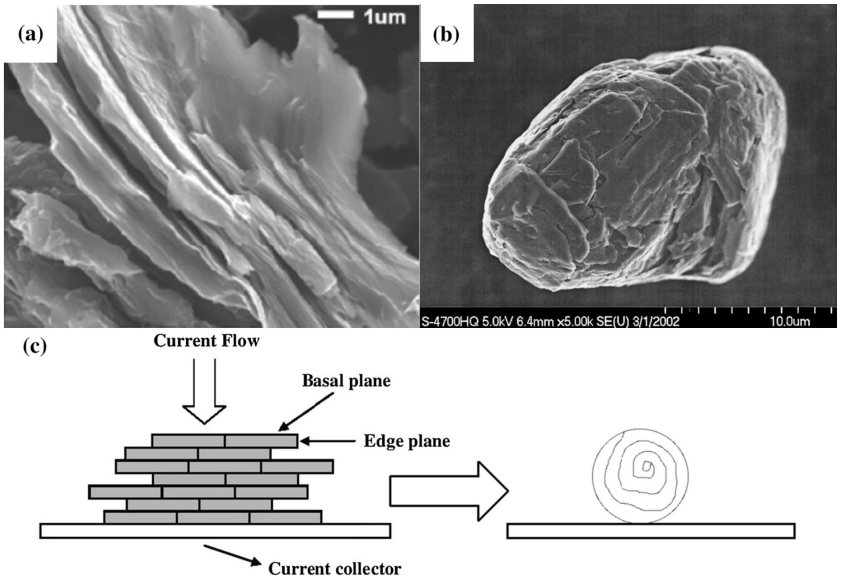

Figure 1.3: (a) SEM image showing basal and edge planes and flake graphite. (b) SEM image of individual potato-shape natural graphite. (c) Schematic views of raw natural graphite flakes, spread on a current collector, parallel to the basal planes, and how the flakes are altered by spheroidization: the flakes are folded concentrically to form potato-shape graphite. Adjusted and reprinted from Moradi et al. [53].

For the positive electrode, the CAM can be made up of a variety of LTMOs, classified as layered oxides ($LiNiCoMnO_2$, $LiNiCoAlO_2$, $LiCoO_2$), spinels ($LiMn_2O_4$) and olivines ($LiFePO_4$) [38, 40, 44, 47]. The current collector of the cathode is typically aluminium ($12-20\mu m$ thick) [38, 78].

The electrodes are produced by extruding a slurry of active electrode material, conductive additives and binder, dissolved in a solvent, onto a current collector. To form a uniform slurry and to facilitate the coating of the material onto the current collector, the most commonly used binder is polyvinylidene fluoride (PVDF), which needs to be processed with n-methyl pyrrolidone (NMP) [38, 44, 74], which is toxic and has strict emission regulations [78]. More recently these materials have sometimes been replaced with less expensive carboxymethyl cellulose (CMC) mixed with styrene butadiene rubber (SBR), which can be dissolved in water, providing substantial advantages concerning cost and sustainability [4, 38, 40, 44, 74, 78].

Further, conductive additives are added, for which nanosized carbon, carbon black, graphene or carbon nano-tubes are employed most often [37, 78]. Additives serve to improve the formation of the solid electrolyte interface, protect the electrodes, stabilize the electrolyte salt, improve safety, improve the deposition of Li, enhance solvation, inhibit Al corrosion and improve wettability [74].

Material-related challenges

Due to the material properties of the BM, there are some challenges identified which complicate separation for any of the proposed separation methods:

- **Variety of cathode chemistries:** There exists a variety of different cathode materials, each with their own respective material properties. Certain separation methods may be more effective on one specific cathode type than another, but no distinction is made between the different chemistries upon collection of spent LIBs.
- **Health, Safety and Environment (HSE) concerns:** There are certain environmental risks concerned with materials contained in LIBs, for instance, the release of metals into the environment, polluting the land and groundwater. Further, toxic fumes can be formed upon the heating of electrolyte. Release of these substances should be prevented.
- **Agglomeration:** After liberation of the active materials, micron-sized particles remain. These very small particles tend to form aggregates, or become entrained/entrapped in larger particles or agglomerates. Due to this mechanism, the particles are not fully liberated anymore, and the mixed anode and cathode materials within agglomerates cannot be successfully separated.
- **Processability in water:** For most separation methods, the material needs to be dispersed in water. Certain elements might dissolve in water due to high reactivity of the material. Further, little is known about the effect on particle agglomeration of BM upon dispersion in water.

1.2.2. Current recycling methods of black mass

Most current recycling methods have been focused towards the recovery of the more valuable metals of the cathode, such as Ni, Co and Cu [3, 23]. These materials only make up a small fraction of the total weight of the BM, as can be seen in figure 1.4. On the other hand, graphite makes up approximately 44 wt.% of the total mass, but is considered to be an impurity from the spent battery material in these processes, and is discarded as waste. Apart from the metals originating from the spent cathode, the recovery of graphite is becoming more relevant. For instance, it should be considered that a lithium ion cell contains at least 11 times more graphite than lithium, adding up to approximately 50 kg in an electrical vehicle's battery pack [23, 43, 53].

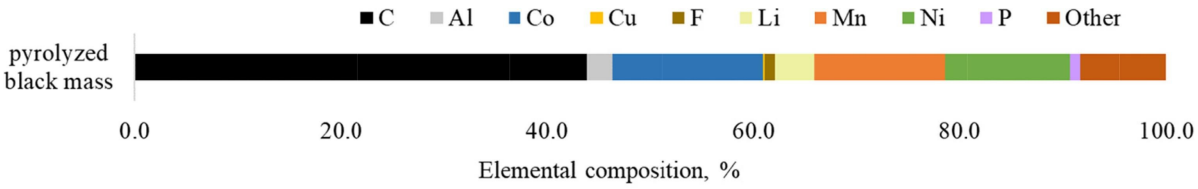

Figure 1.4: Elemental composition of BM obtained with XRF. Light elements such as Li, F, and C were measured by ICP-OES, IC, and carbon analysis, respectively. Reprinted from Salces et al. [69].

There are three types of recycling methods: hydrometallurgy and pyrometallurgy, which are chemical methods requiring chemical reactions, and direct recycling, which is a physical process where no chemical conversion takes place. In pyrometallurgy transition metals like Co and Ni are reduced from oxides to metals at high temperatures. These are recovered in a mixed metal alloy, which can be further separated from each other. Hydrometallurgy makes use of acids to dissolve ions out of a solid, producing a mixture of metal ions in solution, which can be further recovered to produce new cathode material [20, 23, 72]. These methods are associated with multi-unit operation, high energy consumption and high cost, rendering it an uneconomical recycling approach [43]. Further, the electrode active materials are altered structurally and chemically, so that they cannot be directly re-used for the production of new cells [16].

Direct recycling is based on differences in physical properties between materials. Since the materials do not undergo any chemical conversion, these separation processes are usually less energy-intensive. Separation methods exist for various differentiating properties, of which the following will be covered in this research: wettability-based separation (froth flotation), magnetic susceptibility-based separation (magnetic separation) and density-based separation (magnetic density separation). While some of these methods have been explored in separating BM, no industrially applicable process has been developed yet. The focus of this literature review lies in the separation between AAM and CAM from BM by these methods, and their associated opportunities and challenges.

1.2.3. Wettability-based separation

Wettability is the relative adhesion of a fluid to a solid surface [14]. Materials that are *hydrophilic* prefer to be surrounded with water, while *hydrophobic* materials would rather minimize their contact with water and are thus repelled by water. Thus, hydrophobic particles prefer to attach to air bubbles, while hydrophilic particles prefer to remain dispersed in water.

Separation setup

The first, and most widely studied separation method that will be described in this section is one based on difference in wettability: froth flotation (FF). This is a method to separate heterogeneous mixtures of finely subdivided solid phases, based on a difference in wettability. Thus, the separation relies on the difference in attachment of the hydrophobic particles to the air bubbles in a water tank, which move to the top, and the hydrophilic particles, which remain in the liquid and sink to the bottom. A schematic of the process is displayed in figure 1.5.

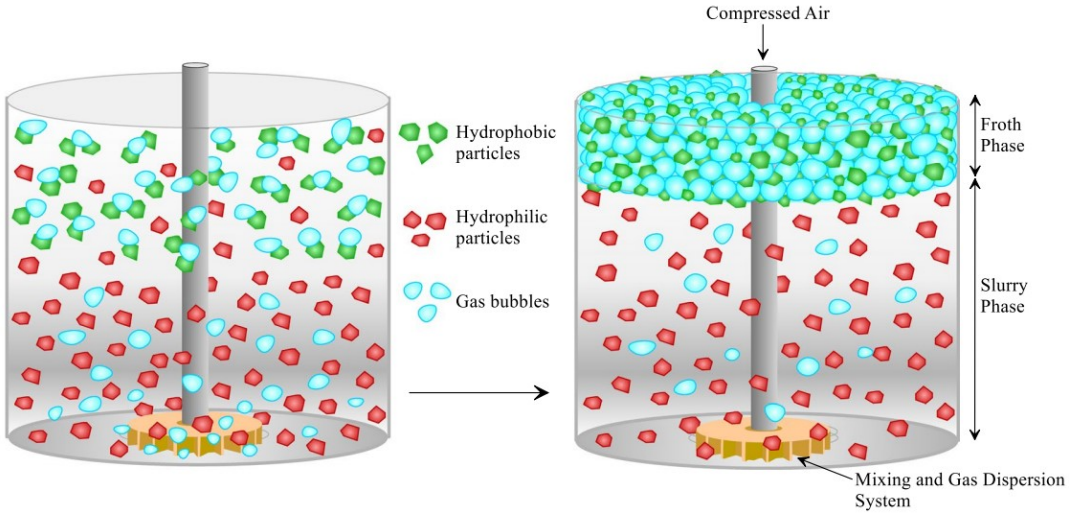

Figure 1.5: Schematic illustration of separation of mineral particles by froth flotation (FF). Reprinted from Pawlik [60].

Battery material wettability properties

The AAM and CAM are intrinsically known to be hydrophobic and hydrophilic, respectively. However, these active materials are coated with a PVDF binder during electrode production, which affects the wettability properties. This fact is clearly illustrated in the research by Vanderbruggen et al. [75]. This research investigates the wettability using the 'captive bubble technique', for which the electrode materials are pressed onto a tab and immersed in water. A tiny air bubble is deposited onto the surface, after which the three-phase line interface is measured.

The experiment was conducted for pristine anode and cathode material (not processed with binder), and anode and cathode material taken from a battery, and the results are displayed in table 1.1 and figure 1.6. Pristine lithium cobalt oxide (LCO) and lithium nickel manganese cobalt oxide (NMC) have a very large contact area with water, while graphite minimizes its contact with water, indicating a large difference in wettability. Unfortunately, the active materials from spent batteries have very similar contact angles.

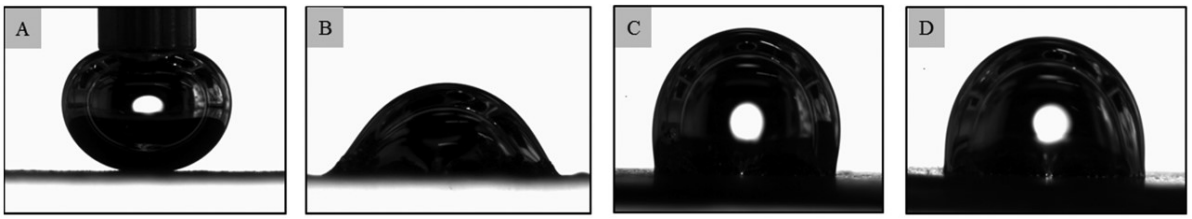

Figure 1.6: Captive bubble technique measurements of A: LCO, B: natural spheroidized graphite, C: cathode electrode made of LCO particles coated on with binder on Al foil, D: electrode made of graphite particles coated with binder on a Cu foil. Reprinted from Vanderbruggen et al. [75].

Material	Contact angle with captive bubble method
LCO	$14 \pm 1.8°$ (A)
NMC	$14.8 \pm 3.3°$ (-)
Natural spheroidized graphite	$138.8 \pm 5.4°$ (B)
Cathode electrode - LCO coated with binder	$74.5 \pm 7.9°$ (C)
Anode electrode - Graphite coated with binder	$81.2 \pm 4.4°$ (D)

Table 1.1: Results for estimating the wetting behavior of battery materials, with an interval confidence of 90%. Reproduced from Vanderbruggen et al. [75].

Pretreatment methods for binder removal

From these results, it is clear that binder contamination strongly limits the selectivity of FF of AAM and CAM. Therefore, several treatment options are available to remove the PVDF binder from the surface of the particles and improve separation by FF: solvent treatment, thermal treatment or mechanical treatment.

Solvent treatment is usually performed with NMP to dissolve the binder. While this method is effective, the biggest drawbacks of NMP are its toxic nature and high cost. Another solvent that can be used is Fenton's reagent, but this generates a layer of $Fe(OH)_3$ on the particle surfaces, which also deteriorates the separation and is difficult to clean [57, 80, 88].

Pyrolysis and roasting are types of heat treatment that can also be carried out for binder removal and are known to be very effective. However, the products and fumes that are formed in this process, amongst which HF gas, are hazardous and pose strong limitations on the viability and applicability, as they are difficult to clean [25, 84, 89, 86, 87, 91].

Finally, binder can be removed by mechanical treatment: grinding the BM. On the one hand, new surfaces are exposed, which are not covered with the binder, on the other hand, under cryogenic conditions, the binder will break from the surface during grinding due to embrittlement. The required particle size suitable for FF should fall between $10 - 300 \mu m$, such that the available adhesion between particle and bubble is sufficient, while also ensuring the particles will become levitated by the buoyancy of the bubble [62]. Unfortunately, the grade and recovery that can be obtained of the products is limited, significant loss of material may occur, and the process of fine grinding is energy-intensive [42, 62, 76, 83].

Challenges associated with wettability-based separation

Removal of binder material is a key requirement to ensure proper selectivity for the separation of BM by FF. For the pretreatment methods of binder removal, the following limitations have been identified:

- **Solvent treatment:** NMP, the solvent most capable of dissolving the binder, is known to be very toxic and very expensive. Because of this, NMP treatment cannot be applied on large scale, as release of toxic substances and cost should be minimized. Further, this treatment method generates a large waste stream.
- **Heat treatment:** Toxic products and fumes, such as HF gas, are generated upon heating of BM. Furthermore, heating is associated with a high energy-consumption and therefore high cost.
- **Mechanical treatment:** Under ambient temperature, the binder contamination of the particle's

surface is not fully removed. Cryogenic grinding enhances the binder removal, but also requires additional energy for cooling, while grinding in itself is already an energy-intensive process. Finally, the range of particle sizes required for FF is narrow, thus significant material losses may occur upon excessive grinding.

1.2.4. Magnetic susceptibility-based separation

The magnetic susceptibility (χ) of materials can be classified into three categories: ferromagnetic, paramagnetic or diamagnetic. Ferromagnetism is a very uncommon property and only occurs in a few materials, causing them to be very strongly attracted to magnetic fields. Apart from these rare materials, all other materials exhibit some magnetic effects, and are either weakly attracted by a magnetic field (positive χ), or weakly repelled (negative χ). They are referred to as paramagnetic and diamagnetic, respectively [18].

This property is used in magnetic separation to steer materials of different magnetic susceptibility in a different direction by attracting or repelling them through the application of a magnetic field. In order to be able to separate small, very weakly magnetic particles, high gradient magnetic separation is required, which is designed to maximize the magnetic field intensity.

Separation setup

Two conventional methods are displayed in figure 1.7 below: induced roll magnetic separation and high gradient magnetic separation. Both methods have been applied on LIB material in the research by Hu et al. [31], as well as in the patent by Ellis and Montenegro [16]. In the drum type separator (induced roll magnetic separation, figure 1.7a) the dry feed material is introduced at the top of a rotating drum. The diamagnetic particles will fall in the left department due to gravity, while the paramagnetic particles are attracted to the drum and carried across the magnetic section of the drum, and afterwards deposited in the right department [58].

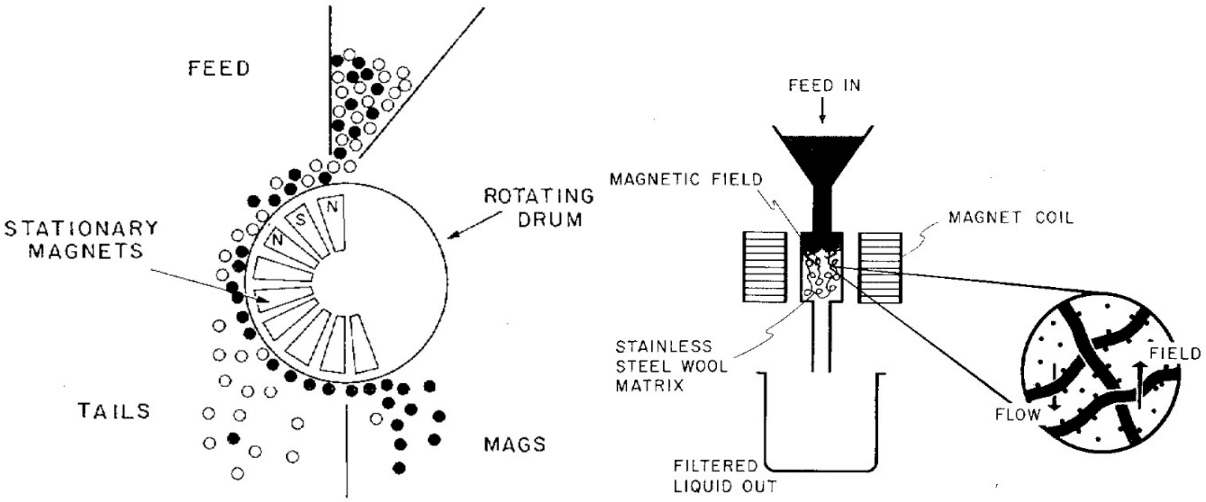

(a) Induced roll magnetic separation, dry.

(b) High gradient magnetic separation, wet.

Figure 1.7: Schematic of conventional magnetic separation methods. Reprinted from Oberteuffer [58].

In the research of Hu et al., this method was performed, using a product of manually extracted current collector sheets, cut into small pieces. While the selectivity for this product was very high, manually extracting the sheets and cutting them to pieces is very labor-intensive, and therefore infeasible to apply on large-scale.

The high gradient magnetic separation in figure 1.7b consists of a canister packed with ferromagnetic filament, surrounded by a strong, adjustable magnetic field. Feed material is introduced in the form of an aqueous slurry and passed down the canister. The fluid and diamagnetic particles pass through the canister, while paramagnetic particles are trapped in the filament, even if they are very small and only weakly magnetic. Once the diamagnetic material has passed through, the magnetic field is removed and the paramagnetic particles can be easily washed out from the canister [58]. The grade and recovery

achieved from Hu et al. using high gradient magnetic separation was lower than that of induced roll magnetic separation.

Another configuration for magnetic separation of LIB material which has been researched, is waterflow-magnetic separation. In this wet separation method, BM materials are dispersed in solution and flowed down a magnetic plate with a small incline. The paramagnetic particles remain stuck at the top of the plate, while the diamagnetic particles flow down to the filter tank, where they are collected by a filter screen. A schematic of the forces acting on the different particles and the resulting particle trajectories is displayed in figure 1.8.

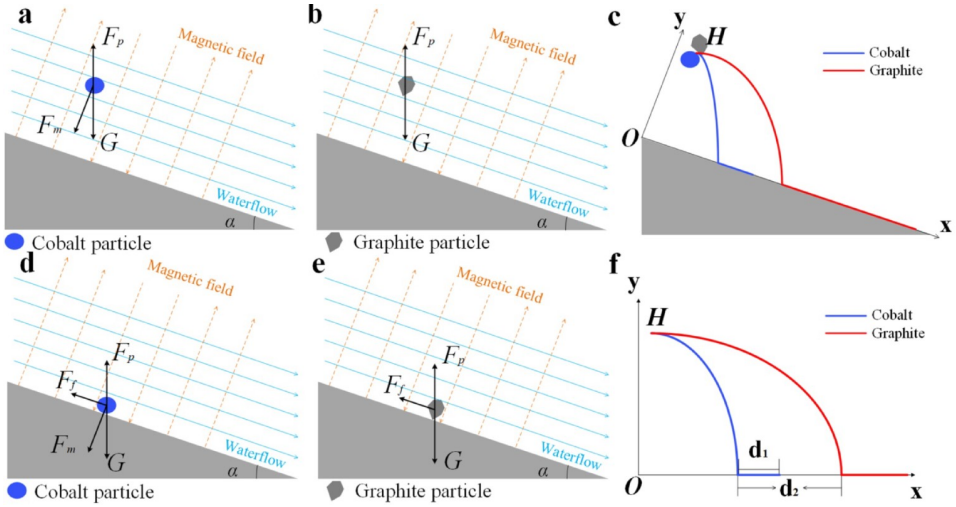

Figure 1.8: Schematic of particle trajectories in waterflow-magnetic separation. Reprinted from Huang et al. [32].

Battery material magnetic properties

Magnetic susceptibility is a dimensionless proportionality constant, which can be described either by volume ($-$), by moles ($\mathrm{m^3\,mol^{-1}}$) or by mass ($\mathrm{m^3\,kg^{-1}}$). The values of the magnetic susceptibility of battery materials, found in literature [16, 31], are shown in table 1.2.

Material	**Reported susceptibility** by [16], [$\mathrm{m^3\,kg^{-1}}$]	**Reported susceptibility** by [31], [$\mathrm{m^3\,kg^{-1}}$]
$LiFePO_4$	$4.82 \cdot 10^{-3}$	$7.41 \cdot 10^{-7}$
$LiMn_2O_4$	$3.52 \cdot 10^{-3}$	-
$LiMnO_2$	-	$5.74 \cdot 10^{-6}$
$LiNiCoMnO_2$	$2.26 \cdot 10^{-3}$	-
$LiNi_{1/3}Co_{1/3}Mn_{1/3}O_2$	-	$3.31 \cdot 10^{-7}$
$LiNi_{0.8}Co_{0.15}Al_{0.05}O_2$	-	$2.51 \cdot 10^{-7}$
$LiNiO_{0.833}Co_{0.170}O_2$	$1.34 \cdot 10^{-3}$	-
$LiCoO_2$	$8.91 \cdot 10^{-5}$	$1.7 \cdot 10^{-8}$
Al (cathode current collector)	-	$8.15 \cdot 10^{-9}$
C	-	$-8.4 \cdot 10^{-8}$
Cu (anode current collector)	-	$-1.12 \cdot 10^{-9}$

Table 1.2: Magnetic susceptibility of materials in LIBs, taken from Ellis and Montenegro, and Hu et al. [16, 31].

It is clear that the reported values differ by three to four orders of magnitude. However, qualitatively the reported values seem to represent approximately the same trend of susceptibilities. These differences indicate that this material property cannot be determined straightforwardly, and thus have to be further investigated. Altogether, from this information it is assumed that the AAM and its corresponding current collector material are very weakly diamagnetic, while the CAM and their respective current collector are all weakly paramagnetic to some extent.

As graphite can occur in a variety of structures, and due to the intercalation of lithium ions during battery operation, its magnetic susceptibility may be altered. The magnetic susceptibility of graphite upon intercalation of lithium ions was investigated by Mukai et al. [54]. It was found that a transition from diamagnetic to paramagnetic took place once a small amount of lithium remained within the graphite structure. More researchers [17, 36, 52] have reported ferromagnetic behavior of graphite, for instance due to structural defects and vacancies [12, 81]. Because the exact structure of graphite retrieved from spent anodes may vary, so may its magnetic susceptibility.

The advantage of this separation method is that no chemicals are used, making it a cost-saving solution with low (hazardous) waste-production. However, a limitation that is often encountered, is that the method works well for CAMs of strong magnetic susceptibility, but not for the BM materials of weaker magnetic susceptibility. Further, aggregation can occur, deteriorating the selectivity [31, 33, 32, 39].

Challenges associated with magnetic susceptibility-based separation

For the separation of BM by magnetic susceptibility, the following difficulties have been found:

- **Weakly paramagnetic cathode material:** The magnetic susceptibility of the cathode materials is only very weakly positive, especially that of LCO. Therefore, very high gradient magnetic fields are required to achieve adequate separation.
- **Entrainment of dry particles:** Magnetic separation can be performed on a slurry or on dry powder. Especially dry powder is expected to be highly sensitive to aggregation and entrainment of small particles in larger particles, leading to misplacement of the mixed materials.
- **Magnetic susceptibility of graphite:** Different values of magnetic susceptibility have been reported, resulting from a difference in the structure of graphite, intercalation of lithium ions, and vacancy defects. The actual magnetic susceptibility should be first determined, to assess the viability of this separation method.

1.2.5. Density-based separation

Finally, density-based separation is investigated, since density is an intrinsic material property that is not (significantly) altered during the processing and lifetime of the active electrode materials. The most basic density-based separation method is the conventional sink-float method: particles dispersed in a liquid will either move to the top or bottom of the tank, depending on whether their density is lower or higher than that of the liquid. This method allows for one single cut-density between which materials can be separated, and was already successfully performed for the separation between anode and cathode, using lithium metatungstate (LMT) [85] or sodium polytungstate (SPT) [71]. These are dense liquids, which are very expensive, toxic and viscous, and are therefore not suitable for large-scale operation. Instead, a magnetic liquid could be used, in which a density gradient can be generated by applying a magnetic field.

Separation setup

Magnetic density separation (MDS) is similar to conventional sink-float separation techniques, but it offers the opportunity to separate multiple materials of different densities in one step. This is achieved by creating an artificial density gradient within a magnetic process medium by applying a magnetic field. The magnetic liquid will not only be subjected to the gravity and buoyancy forces, but also to a magnetic force. The resultant force on the magnetic liquid will vary according to its proximity to the magnet(s), as visualized in figure 1.9.

The forces acting on a particle suspended in a paramagnetic liquid within a magnetic field are described in equation 1.1, as formulated by Ge and Whitesides, and by Mirica et al. [21, 50]. The gravity scales with the difference in density of the particle (ρ_s) and the density of the paramagnetic liquid (ρ_m). The magnetic force scales with the difference in magnetic susceptibility between the particle (χ_s) and the magnetic susceptibility of the paramagnetic liquid (χ_m). The particle will find its equilibrium position at the height corresponding to the particle's density. Different materials of different densities will be stratified at their own equilibrium height.

$$\overrightarrow{F}_g + \overrightarrow{F}_{mag} = (\rho_s - \rho_m)V\overrightarrow{g} + \frac{(\chi_s - \chi_m)}{\mu_0}V(\overrightarrow{B}\cdot\overrightarrow{\nabla})\overrightarrow{B} = 0 \tag{1.1}$$

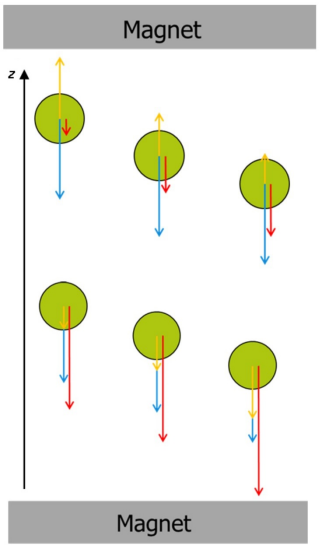

Figure 1.9: Forces on magnetic liquid in a magnetic field. Yellow arrow is magnetic force; blue arrow is gravity; red arrow is total resultant force. Reproduced from Hu et al. [28].

The most prevalent liquid that is used for MagLev experiments in literature, is a solution of $MnCl_2$ [13, 15, 21, 50, 51], due to its relatively low cost and high magnetic susceptibility. A common magnetic configuration for this method is the 'anti-Helmholtz configuration', using two magnets with facing like-poles. A 2D representation of the magnetic field that is created by this configuration is shown in figure 1.10a. By this configuration MagLev of liquid drops of densities up to $3.73\,\mathrm{g\,cm^{-3}}$ in $MnCl_2$ solution has been achieved by Ge and Whitesides [21], and even MagLev of precious metals (Silver, Copper, Gold, Platinum) of densities up to $21.5\,\mathrm{g\,cm^{-3}}$ in a $MnCl_2$ solution has been achieved by Miura et al. [51].

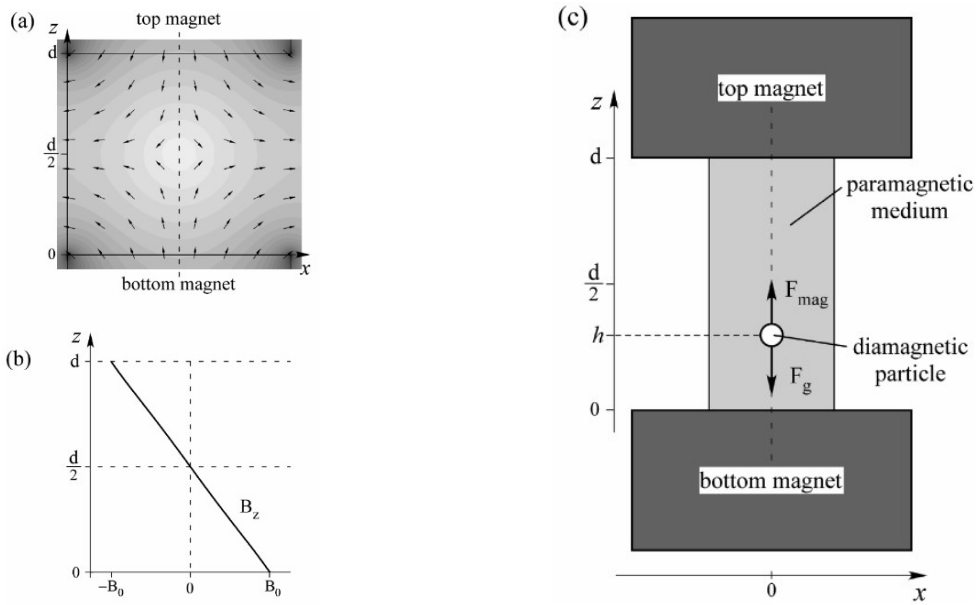

Figure 1.10: (a) 2D numerical simulation of the magnetic field between two equal magnets, with like-facing poles. (b) Magnitude of the magnetic field along the centreline. (c) Schematic illustration of the experimental setup. Reprinted from Mirica et al. [50].

This principle has also been implemented in a continuous setup for the separation of plastic waste materials. A schematic of such a continuous MDS process is shown in figure 1.11.

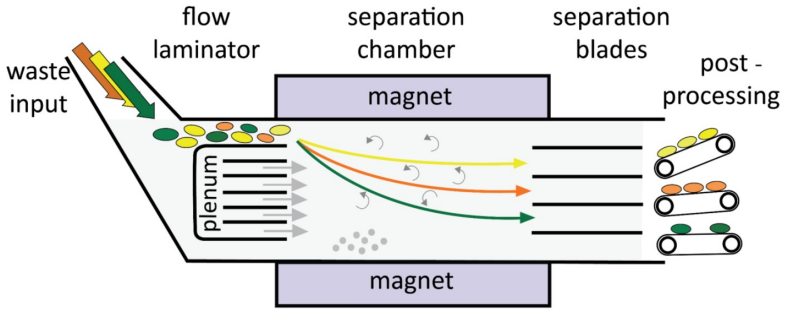

Figure 1.11: Schematic of the magnetic density separation (MDS) machine. Note that different colors represent different mass densities of plastics. Reprinted from Dellaert [13].

Reported material properties

The densities of the active electrode materials were collected from the literature review by van Rooijen [66] and research by Al-Shammari and Farhad [71], their results are displayed in table 1.3

Grain type	**Particle density** $[\mathrm{g\,cm^{-3}}]$, [71]	**Particle density** $[\mathrm{g\,cm^{-3}}]$, [66]
LFP ($LiFePO_4$)	3.600	$3.0 - 3.6$
LMO ($LiMn_2O_4$)	4.280	–
NCA ($LiNi_{0.8}Co_{0.15}Al_{0.05}O_2$)	4.450	–
LCO ($LiCoO_2$)	5.050	$4.5 - 5.1$
NMC(-111)	4.770	$4.0 - 5.0$
Graphite	2.200	$2.2 - 2.3$
Carbon Black	–	$1.5 - 1.9$

Table 1.3: Density of the different materials present in black mass. Reproduced from Al-Shammari and Farhad, and Van Rooijen [71, 66].

There are some challenges associated with MDS: Generally, MDS shows a good selectivity for larger particles, that do not aggregate, while BM has very small size, for which aggregation is much more likely to occur. The apparent densities that have been achieved with permanent magnets in the literature are only a bit higher than that of AAM, and not larger than that of most CAMs. Scaling to continuous separation can be challenging due to the high magnetic field intensity required, as well as due to turbulence. Finally, the solutions of $MnCl_2$ will be contaminated and thus need to be partially refreshed every few separation cycles [6, 13, 21, 28, 29, 30, 50, 51, 56, 70].

Challenges associated with density-based separation

Magnetic levitation offers additional flexibility for the separation of BM, as it can separate multiple materials of different densities within one stage. The following challenges have been identified:

- **High density of anode and cathode materials:** The process medium is required to have an intermediate density, thus a liquid of (apparent) density between approximately $\rho = 2.5{-}3.0\,\mathrm{g\,cm^{-3}}$ is required.
- **Magnetic field configuration:** Permanent magnets are limited in the magnetic field intensity that they can generate. Higher intensities would require the use of either superconducting magnets, which need energy for cooling, or electromagnets, which consume even more energy.
- **Paramagnetic liquid:** In order to obtain a sufficient apparent density, a high magnetic susceptibility of the liquid is required. Concentrations close to the saturation concentration of $MnCl_2$ are needed to obtain this susceptibility. However, the $MnCl_2$ is a hazardous substance, and should thus be carefully handled and disposed, especially at large scale.
- **Scalability:** In order to turn the static MagLev into a continuous MDS process, issues come to play related to maintaining a constant magnetic field intensity over the height of the MDS, turbulence, and the large amount of $MnCl_2$ required.

1.3. Research objective and research questions

The aim of this thesis research is to assess the feasibility of a new method for the direct recycling of LIBs using a hydro-mechanical separation method. From the separation methods discussed in the previous section, each method is associated with its own challenges. However, since the wettability of the materials is strongly altered and cannot easily be restored, and because the magnetic susceptibility of the materials is very weak and is reported to have both positive and negative values for certain alterations to the graphite, density seems to be the most promising property to separate both materials.

Thus, magnetic density separation (MDS) is selected as the separation method to be investigated in this research. It will be investigated whether static MagLev of AAM (and CAM) can be achieved in a paramagnetic $MnCl_2$ solution using permanent magnets, as a proof of concept for MDS as a scalable separation method.

Research objective

Assess whether MDS can be employed as an affordable, scalable/continuous and selective method for the separation between anode and cathode materials, by experimentally investigating whether static MagLev of battery materials can be achieved.

The applicability of the method relies on the gradient magnetic field intensity that can be achieved, and the magnetic susceptibility of the paramagnetic liquid, which both need to be precisely determined. Chapter 3 shows that ambiguous values of the magnetic susceptibility were reported in the literature, and no accurate method is in place to measure this property. Therefore, a novel method has been developed to measure the magnetic susceptibility of the paramagnetic liquid.

Following from this research objective, the research question is formulated as:

Research question

Can a sufficiently high apparent density be obtained by static MagLev for the levitation of graphite, indicating MDS to be a promising separation method for the separation between AAM and CAM?

To answer this research question, several subquestions have to be addressed:

- SQ1: What gradient magnetic field intensities can be generated using permanent NdFeB magnets and what is the optimal configuration?
- SQ2: What density and magnetic susceptibility of $MnCl_2$ solutions are reported in the literature, are these sufficient for MagLev of graphite?
- SQ3: What methods are required to prepare a transparent solution that does not precipitate, what issues related to the material are encountered, and what is the elemental composition and density of the solution?
- SQ4: What method can be developed to measure the magnetic susceptibility of the solution, do the measured magnetic susceptibilities agree well with the values reported in literature, and what magnetic susceptibility of the solutions can be achieved?
- SQ5: What apparent densities can be achieved in a static MagLev setup, and can levitation of graphite be achieved?
- SQ6: Will the graphite particles themselves be attracted or repelled by the magnetic field significantly, overshadowing the effect of magnetic buoyancy?
- SQ7: What opportunities and limitations have been identified for scaling the method into a continuous process?

1.4. Structure of the research

The range of densities that can be levitated in a magnetic liquid, depends on the force of gravity and the magnetic force that act on the liquid and on the particles suspended in the liquid. These forces were described in equation 1.1. The equation can be rewritten to describe the particle density that can be levitated in the liquid, the achievable 'apparent density', as follows:

$$\rho_s = \rho_m + \frac{\chi_m - \chi_s}{g\mu_0}(\vec{B} \cdot \vec{\nabla})\vec{B} \tag{1.2}$$

From this formula it becomes clear that the attainable apparent density of a suspended particle in the liquid, ρ_s, is a function of the gradient magnetic field intensity $(\vec{B} \cdot \vec{\nabla})\vec{B}$, the density and magnetic susceptibility of the paramagnetic liquid, ρ_m and χ_m, and the magnetic susceptibility of the suspended particles, χ_m. As these individual properties play a role in the viability of MDS of BM, these properties are evaluated in separate chapters.

$$\rho_s = \rho_m + \frac{\chi_m - \chi_s}{g\mu_0}(\vec{B} \cdot \vec{\nabla})\vec{B}$$

The chapters will address the different properties as follows: In chapter 2 the attainable gradient magnetic field intensity will be identified through simulations. Next, the properties of the magnetic solution will be investigated from literature research in chapter 3, and the resulting achievable apparent density will be calculated. Chapter 4 first discusses practical implications of handling the material and preparing the solution samples, and then the elemental composition and density of the samples will be determined experimentally. In chapter 5 a new method is developed to measure the magnetic susceptibility of a solution, which will be conducted for all samples and compared to the values from literature. Finally, in chapter 6 the resulting apparent density from the experimentally determined properties will be calculated, and Magnetic Levitation (MagLev) experiments will be conducted to validate the calculations, and to see whether graphite can indeed be levitated.

Investigated property	Chapter		Subquestion
$(\vec{B} \cdot \vec{\nabla})\vec{B}$	2	Magnetic field simulations for the optimization of the magnetic force	SQ1
ρ_m, $\chi_m \rightarrow \rho_s$	3	Estimated solution properties and apparent density from literature data	SQ2
ρ_m	4	Preparation of the solution, experimental characterization and density measurements	SQ3
χ_m	5	Magnetic pendant drop method for measuring the magnetic susceptibility	SQ4
$\rightarrow \rho_s$, χ_s	6	Estimation of the apparent density & validation using Magnetic Levitation	SQ5, SQ6, SQ7

2

Magnetic field simulations for the optimization of the magnetic force

In this chapter the magnetic field intensities that can be achieved through various magnetic field configurations will be studied. The objective of this research is to identify the gradient magnetic field intensity, $(\vec{B} \cdot \vec{\nabla})\vec{B}$, in the apparent density equation:

$$\rho_s = \rho_m + \frac{\chi_m - \chi_s}{g\mu_0}(\vec{B} \cdot \vec{\nabla})\vec{B}$$

Permanent neodymium magnets were selected for this research, since these do not have any operational costs, in contrast to electromagnets and superconducting magnets. In order to obtain a high apparent density, this intensity should be sufficiently large to realize the magnetic levitation of graphite. The subquestion that will be addressed in this chapter is the following:

> SQ1: What gradient magnetic field intensities can be generated using permanent NdFeB magnets and what is the optimal configuration?

2.1. Magnetic field evaluation methods

For the analysis of the magnetic fields generated by permanent magnets, two programs were used: Matlab for one-dimensional calculation of the magnetic flux density along the symmetry axis of a permanent magnet, and COMSOL Multiphysics for 3-dimensional simulations of the magnetic fields surrounding permanent magnets in several configurations. For each configuration the resulting gradient magnetic field intensity is evaluated.

For the one-dimensional magnetic flux density along the symmetry axis of a magnet, there only exists a magnetic field component in the direction of the symmetry axis. Thus, when aligning the symmetry axis with the z-axis, the gradient magnetic field intensity $(\vec{B} \cdot \vec{\nabla})\vec{B}$ from equation 1.1 reduces to the following:

$$(\vec{B} \cdot \vec{\nabla})\vec{B} = B_x\frac{\partial B_z}{\partial x} + B_y\frac{\partial B_z}{\partial y} + B_z\frac{\partial B_z}{\partial z} = B_z\frac{\partial B_z}{\partial z}$$

The magnetic flux density along the symmetry axis of a magnet B_z can be calculated for several magnets. Cylindrical magnets were selected, since these are easily commercially available, simpler to handle than spherical magnets, and can achieve a slightly higher magnetic flux density than magnets of other geometries of the same material grade. The field along the symmetry axis of a cylindrical magnet can be described by the following formula [27, 64]:

$$B_z = \frac{B_r}{2}\left(\frac{t+z}{\sqrt{R^2+(t+z)^2}} - \frac{z}{\sqrt{R^2+z^2}}\right) \tag{2.1}$$

In this formula, B_r [T] is the magnetic remanence of a magnet, which is a material property described by the grade of a permanent magnet, t [m] is the thickness of the magnet, R [m] is the radius and z [m] is the distance from the surface of the pole of the magnet. The gradient $\frac{\partial B_z}{\partial z}$ can be calculated as follows:

$$\frac{\partial B_z}{\partial z} = \frac{B_r R^2}{2}\left(\frac{1}{(R^2+(t+z)^2)^{3/2}} - \frac{1}{(R^2+z^2)^{3/2}}\right) \tag{2.2}$$

Permanent NdFeB disc magnets of a radius of $R = 10\,\mathrm{mm}$ and a thickness of $t = 2\,\mathrm{mm}$ were purchased from supermagnete [27], at a cost of €0.99 per piece. The grade of the magnets was N52, indicating a magnetic remanence of $B_r = 1.42\,\mathrm{T}$, which is the highest commercially available grade of NdFeB magnets. Disc magnets were the only geometry that were available at the N52 grade, and $20\,\mathrm{mm}$ was the largest diameter available. These thin, disc magnets can be stacked into an array, after which a longer cylindrical magnet is obtained. Matlab was used to evaluate the gradient magnetic field intensity $B_z\frac{\partial B_z}{\partial z}$ along the symmetry axis, as a function of the distance from the magnet's surface

To obtain the magnetic flux density around magnets in 3D, COMSOL Multiphysics can be used to perform 'Finite Element Method Magnetic' simulations. This software was not only applied to study the magnetic field around the array of the commercially available disc magnets, but also to several other magnetic configurations, which will be discussed in the following section.

The simulations in COMSOL were setup as follows: a component was created, in which the geometry of the magnet was defined. From the 'AC/DC' package in the material library, 'BMN-52' was selected from the 'NdFeB' folder. Around the magnet geometry, a larger box was created, to which 'air' was assigned as the material, which has a magnetic susceptibility very close to zero. Next, the physics package 'Magnetic Fields (mf)' was added, and the designated surfaces for the north and south poles were assigned. The magnet was given a very fine tetrahedral mesh, whereas the mesh of the surrounding air was slightly coarser. Finally, a stationary study was performed to solve the problem, resulting in a 3D visualization of the magnetic flux density.

Further, for a given cutline through the geometry, the values of B_z and $\frac{\partial B_z}{\partial z}$ can be calculated, and plotted along the cutline. This way, the gradient magnetic field intensity $B_z\frac{\partial B_z}{\partial z}$ can be more precisely determined at different distances from the magnet's surface. For each configuration two cutlines are evaluated: one through the symmetry axis of the magnet, and another one at a distance of $0.5\,\mathrm{mm}$ from the side of the magnet, parallel to the symmetry axis.

2.2. Resulting magnetic fields

In this section the magnetic flux density simulations are displayed, as well as the gradient magnetic field intensity along a cutline through the center of the magnetic configuration, and the gradient magnetic field intensity along a cutline near the edge of the magnets.

Individual cylindrical magnet

In figure 2.1 the resulting field from an array of the purchased disc magnets is shown, for both an array of 10 magnets ($t = 20\,\mathrm{mm}$) and an array of 25 magnets ($t = 50\,\mathrm{mm}$), as calculated by Matlab. The vertical lines indicate the surface of the poles of the magnet, the blue graph represents the z-component of the flux density B_z [T] around the magnet. Apart from the absolute flux density around the magnet, the gradient of the flux density was also plotted in the red, continuous line.

Since the goal of the method is to maximize the gradient magnetic field intensity to obtain a high apparent density, this quantity is also plotted in the red, dashed line. By increasing the number of magnets in the array by a factor 2.5, the magnetic product is only increased by 20%: from $-41.05\,\mathrm{T^2\,m^{-1}}$ to $-49.05\,\mathrm{T^2\,m^{-1}}$. Thus, increasing the length of the array by a lot, will eventually only lead to a relatively

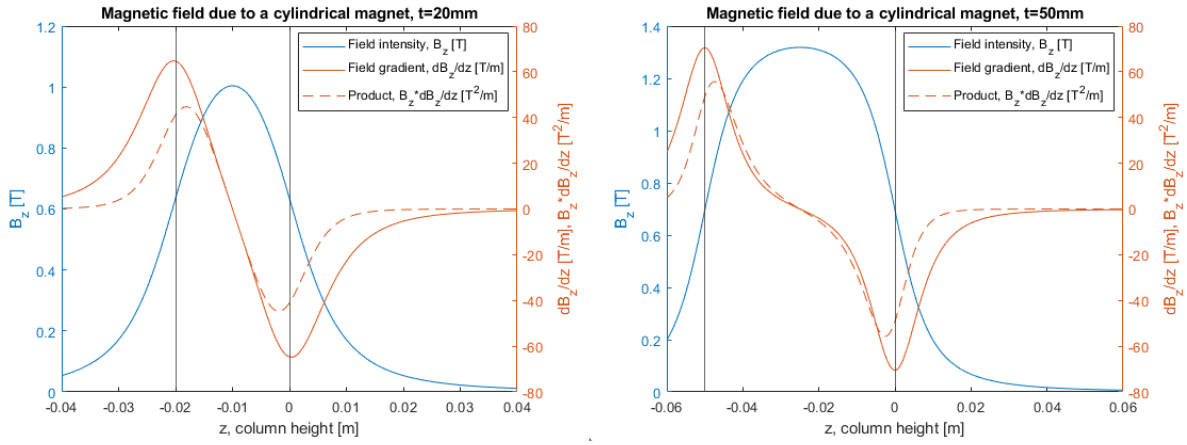

(a) Array of 10 disc magnets, $t = 20\,\mathrm{mm}$.

(b) Array of 25 disc magnets, $t = 50\,\mathrm{mm}$.

Figure 2.1: Magnetic flux density, gradient, and gradient magnetic field intensity around a cylindrical N52 neodymium magnet of a radius of $20\,\mathrm{mm}$ and thickness of $2\,\mathrm{mm}$.

small increase in the gradient magnetic field intensity, thus it will not be worthwhile to increase the number of magnets in the array much further than 10.

The array of 10 magnets was further simulated in COMSOL, represented by a single cylindrical magnet of a thickness of $20\,\mathrm{mm}$. In figure 2.2 the magnetic flux density is displayed in a color scale, both from a sideview to the magnet, and from an isometric view.

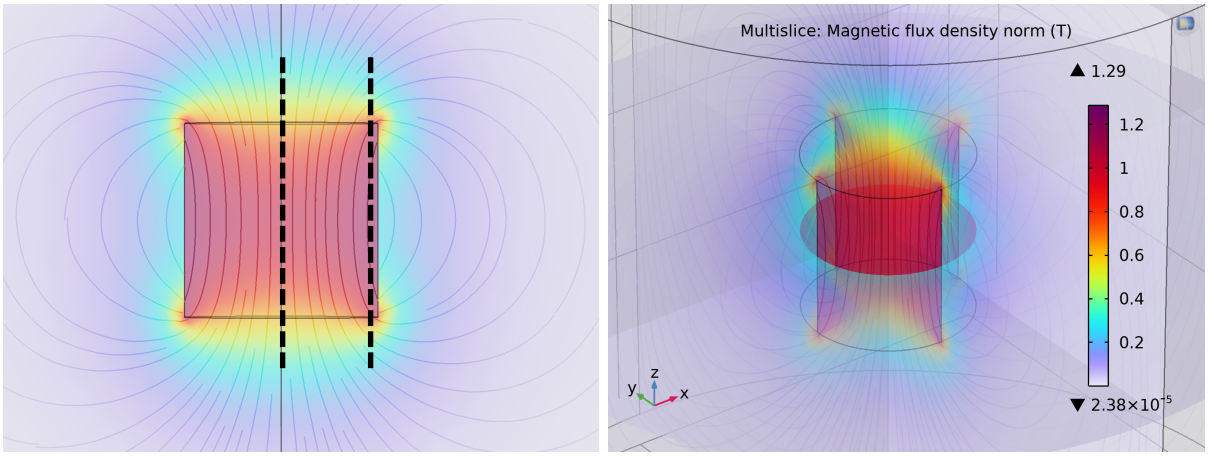

Figure 2.2: Single cylindrical magnet ($d = 20\,\mathrm{mm}$, $t = 20\,\mathrm{mm}$) magnetic field.

Within the magnet and far outside of the magnet, the color seems to indicate a relatively uniform flux density, indicating a small field gradient. Close to the poles, and especially near the edges of the magnet, the color changes rapidly over a very small distance, indicating a larger field gradient. However, it is difficult to quantify the magnetic flux density and gradient from the color-scale. Therefore, the magnetic flux density, gradient, and the gradient magnetic field intensity were further evaluated along the 'cutlines', which are displayed in the black, dashed lines in figure 2.2.

In figure 2.3a the z-component of the magnetic flux density (blue), its gradient (green), and the gradient magnetic field intensity (red) along the cutline through the symmetry axis of the magnet are shown. The magnet is located between $[0.04, 0.06]\,\mathrm{m}$ on the arc length on the horizontal axis in the graph. This graph strongly resembles the graph of figure 2.1a, providing a validation of the simulation model. In the second subfigure the same properties are displayed, but this time through the cutline close to the side edge of the magnet.

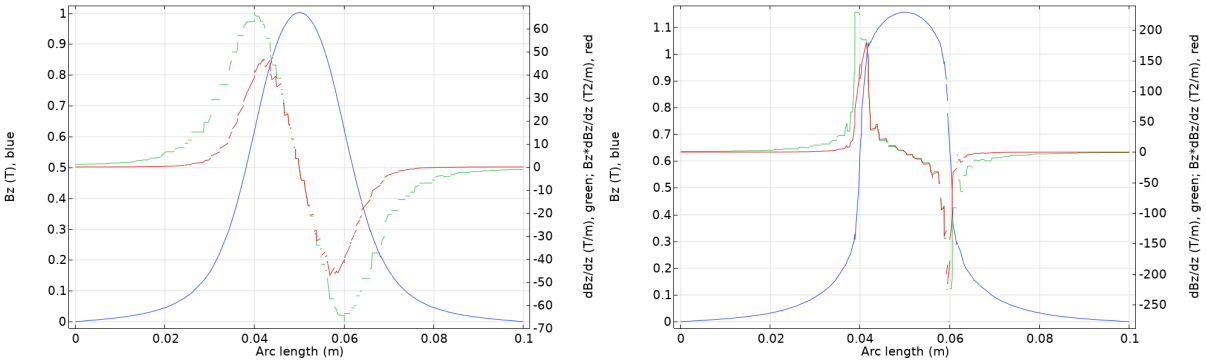

(a) Along the symmetry axis.

(b) Just inside the side surface of the magnet.

Figure 2.3: Z-component of magnetic flux density B_z, [T] (blue), gradient $\frac{\partial B_z}{\partial z}$, [$\mathrm{T\,m^{-1}}$] (green), and the gradient magnetic field intensity $B_z \frac{\partial B_z}{\partial z}$, [$\mathrm{T^2\,m^{-1}}$] (red) of a single cylindrical magnet. The magnet is located between $[0.04, 0.06]$ m along the arc length on the horizontal axis.

The absolute maximum values of the gradient magnetic field intensity are approximately $40\,\mathrm{T^2\,m^{-1}}$ and $140\,\mathrm{T^2\,m^{-1}}$, at the center and at $0.5\,\mathrm{mm}$ to the inside of the edge of the magnet, respectively. However, the decay of the gradient magnetic field intensity close to the side of the magnet happens much more rapidly. To quantify this, two characteristics of the field intensity will be described for each configuration: the maximum gradient magnetic field intensity at the surface of the magnet, and the distance from the surface for which the gradient magnetic field intensity becomes smaller than $10\,\mathrm{T^2\,m^{-1}}$.

Magnetic Configuration	**Maximum $B_z \frac{\partial B_z}{\partial z}$ on magnet surface [$\mathrm{T^2\,m^{-1}}$]**	**Distance from surface for which $B_z \frac{\partial B_z}{\partial z}$ > $10\,\mathrm{T^2\,m^{-1}}$, [mm]**
Cylindrical (t =20 mm), at center	41.1	6.8
Cylindrical (t =20 mm), near edge	143	2.3

Ultimately, it is expected that the magnetic force that can be generated on the surface of the magnet, is larger at the side than at the center of the magnet. However, since the red graph near the side of the magnet decays much more rapidly than towards the center of the magnet, the working distance over which the magnetic force is available, is very small near the side of the magnet. Therefore, using the field above the side of the magnet might have more stringent limitations.

Anti-Helmholtz configuration

The second configuration that was evaluated, is known as the 'Anti-Helmholtz' configuration, in which two magnets are opposing one another with facing like-poles. This configuration is known to possibly enhance the magnetic field gradient available between two magnets, compared to a single magnet.

Since the principle of superposition holds for magnetic fields, the magnetic field resulting from two cylindrical magnets, with the same dimensions as described in the previous section in an Anti-Helmholtz configuration, can be calculated through the addition of their two individual magnetic fields. Thus, a Matlab calculation was once again performed to determine the magnetic flux density along the symmetry axes of the cylindrical magnets. For the calculation, a distance of $20\,\mathrm{mm}$ between both magnets was taken.

The individual magnetic flux densities along the symmetry axes of two cylindrical magnets in Anti-Helmholtz configuration, located between $[-0.03, -0.01]$ m (blue), and between $[0.01, 0.03]$ m (red) are displayed in figure 2.4. In yellow, the total flux density resulting from both magnets combined is displayed.

Figure 2.5 shows the flux densities around both magnets in a color scale. It is clear that the field lines between the magnets are squeezed closer together, than at the other ends of the magnets, indicating an increased flux density gradient. However, due to superposition it should be noted that the absolute field intensities are also able to cancel one another, resulting in a smaller absolute value of the flux density. Again, the dashed, black lines represent the cutlines along which the magnetic flux density and gradient will be further evaluated.

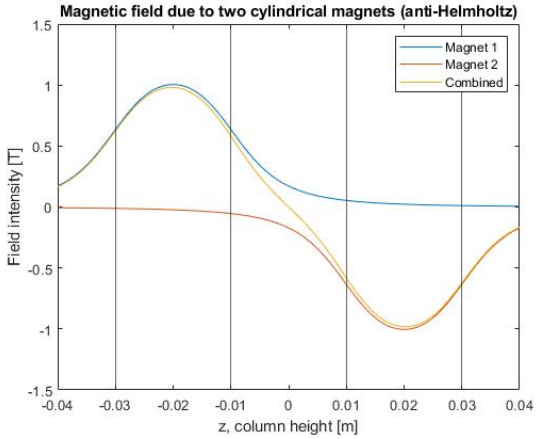

Figure 2.4: Field arising from two cylindrical magnets with facing like-poles, located between $[-0.03, -0.01]$ and $[0.01, 0.03]$ m.

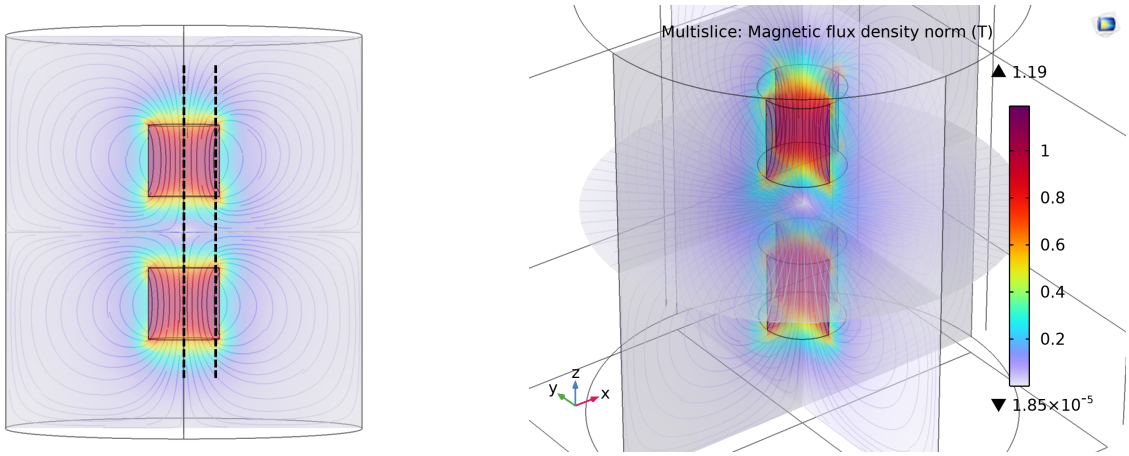

Figure 2.5: Anti-Helmholtz cylindrical magnets (d =20 mm, t =20 mm) magnetic field.

In figure 2.6 the resulting flux density from the anti-Helmholtz configuration is displayed in blue, the gradient in green, and the gradient magnetic field intensity in red. The magnets are located between $[0.02, 0.04]$ and $[0.06, 0.08]$ m along the arc length on the horizontal axis in the graph. The left figure is evaluated along cutline through the symmetry axes of the magnets, while the right figure is evaluated along the second cutline, at 0.5 mm inside the edge of the magnets.

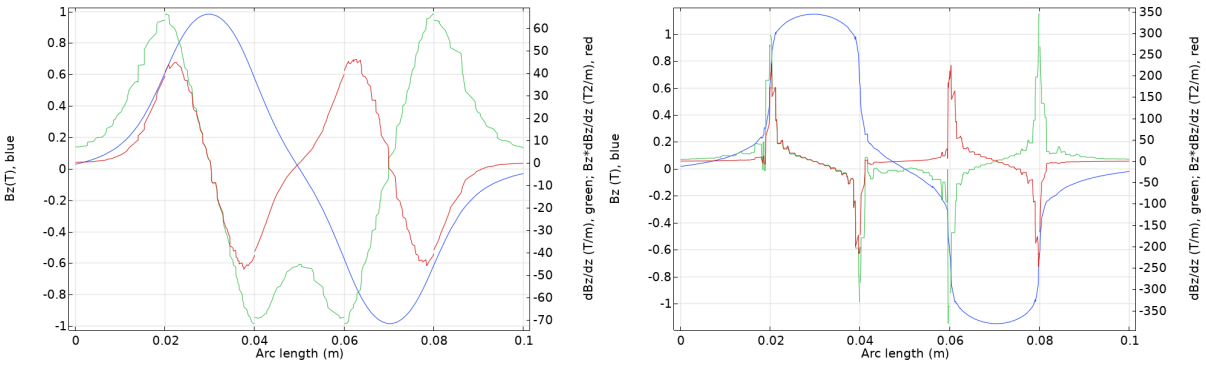

(a) Along the symmetry axis.

(b) 0.5 mm to the inside of the side surface of the magnet.

Figure 2.6: Magnetic flux density (blue), gradient (green), and the gradient magnetic field intensity (red) of an anti-Helmholtz configuration of two cylindrical magnets. The magnets are located between $[0.02, 0.04]$ and $[0.06, 0.08]$ m along the arc length.

The flux density along the symmetry axis again follows the same graph as previously found in figure 2.4. Close to the edge of the magnet, the gradient of the field is much larger than at the center. This results in larger peaks in the product of the flux density and gradient very close to the edges of the magnet, as we have seen before in the example of the single cylindrical magnet. The resulting maximum available values outside of the magnet are of the same order of magnitude as for the single cylindrical magnet. While the maximum gradient magnetic field intensity at the surface of the magnet is much larger, the available working distance where the intensity is still of significant strength, it once again very short.

Magnetic Configuration	**Maximum $B_z \frac{\partial B_z}{\partial z}$ on magnet surface [$\mathrm{T^2\,m^{-1}}$]**	**Distance from surface for which $B_z \frac{\partial B_z}{\partial z}$ > $10\,\mathrm{T^2\,m^{-1}}$, [mm]**
Anti-Helmholtz, at center	39.6	6.1
Anti-Helmholtz, near edge	200	2.0

Anti-Helmholtz Rings

In the paper presented by Ge and Whitesides [21], following up on the research of Mirica et al. [50], it is proposed to use ring magnets to improve the magnetic force that can be exerted on the liquid. In the simulation, the same dimensions of the magnets that were used by Ge and Whitesides have been applied. The results of the simulation are shown in figure 2.7.

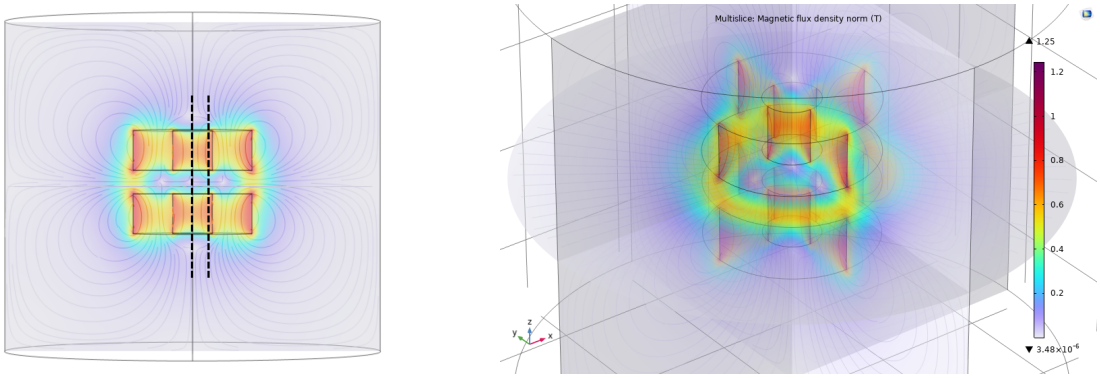

Figure 2.7: Anti-Helmholtz rings, according to the geometry as used by Ge and Whitesides [21] .

From the simulation it can be seen that even within the holes of the magnets, the flux density is still quite large. However, the color gradient is relatively uniform, thus a small gradient is expected at this location. To quantitatively evaluate the flux density and gradient, this is once again evaluated along the black, dashed lines: one through the center of the holes in the magnets, and one at $0.5\,\mathrm{mm}$ to the inside of the inner diameter of the rings.

Figure 2.8 below shows the graphs of the flux density (blue), field gradient (green), and gradient magnetic field intensity (red) for the Anti-Helmholtz rings, which are located between $[0.02, 0.0454]$ and $[0.0604, 0.0858]\,\mathrm{m}$ along the arc length on the horizontal axis of the graph. The left figure is evaluated along the cutline through the center of the holes in the magnets, and the right figure is evaluated just within the inner diameter of the rings.

The absolute values of the gradient magnetic field intensity are much smaller than that of the previous configurations ($<20\,\mathrm{T^2\,m^{-1}}$), and the distance for which the intensity is larger than $10\,\mathrm{T^2\,m^{-1}}$ is even shorter. The advantage of the rings, is that the liquid can be positioned within the holes in the magnet. However, the gradient magnetic field intensity inside the rings is also still lower than that of the previous configurations. Thus, it seems this configuration does not improve the magnetic force that can be induced.

Magnetic Configuration	**Maximum $B_z \frac{\partial B_z}{\partial z}$ on magnet surface [$\mathrm{T^2\,m^{-1}}$]**	**Distance from surface for which $B_z \frac{\partial B_z}{\partial z}$ > $10\,\mathrm{T^2\,m^{-1}}$, [mm]**
Anti-Helmholtz Rings, at center	18.5	2.1
Anti-Helmholtz Rings, near edge	8.8	N/A

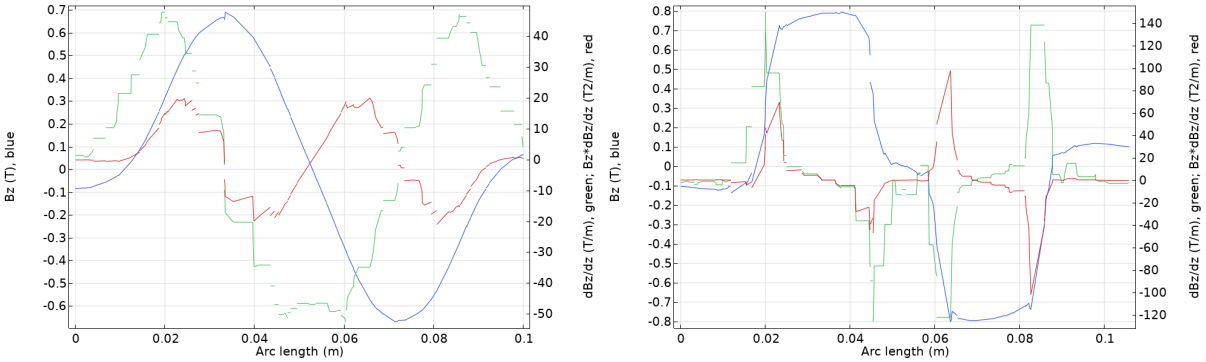

(a) Along the symmetry axis.

(b) $0.5\,\mathrm{mm}$ to the inside of the side surface of the magnet.

Figure 2.8: Magnetic flux density (blue), gradient (green), and the gradient magnetic field intensity (red) of an anti-Helmholtz rings. The magnets are located between $[0.02, 0.0454]$ and $[0.0604, 0.0858]$ m along the arc length.

Furthermore, for some reason the graph is much more jagged for this configuration than the previous ones, especially through the second cutline near the side of the magnet. This might be due to the size of the simulation, requiring a finer mesh to obtain an accurate result. However, by decreasing the mesh size, no significant improvements of the graphs were observed. The results are also not symmetric, as would be expected, and are therefore expected to be less accurate. However, similarly to the findings at the center of the hole, it seems the rings will not be able to generate a stronger magnetic force than the previous configurations.

Halbach Array

The Halbach Array is a special configuration of cubic magnets, each rotated 90° with respect to the previous one, causing the magnetic field to be strengthened at one side, and nearly canceled at the other. Figure 2.9 explains how this field is built up from two separate configurations through superposition.

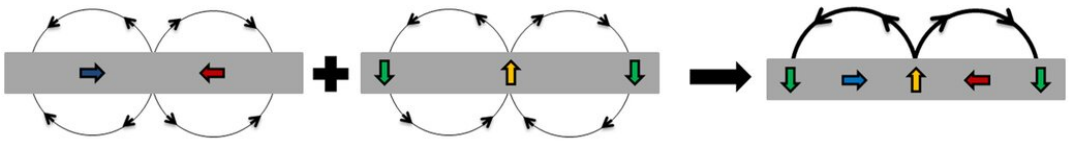

Figure 2.9: Principle of Halbach array through superposition [35].

A 2D simulation of a Halbach array was performed, assuming an infinite depth, such that end effects should not have to be taken into account. To diminish end effects at the sides from occurring, a long array of eleven $20\mathrm{x}20\,\mathrm{mm}$ magnets was created, which is shown in figure 2.10. The flux density is once again displayed with a color scale, but it should be noted that the maximum value on the scale is approximately a factor 1.5 higher than in the previous simulations.

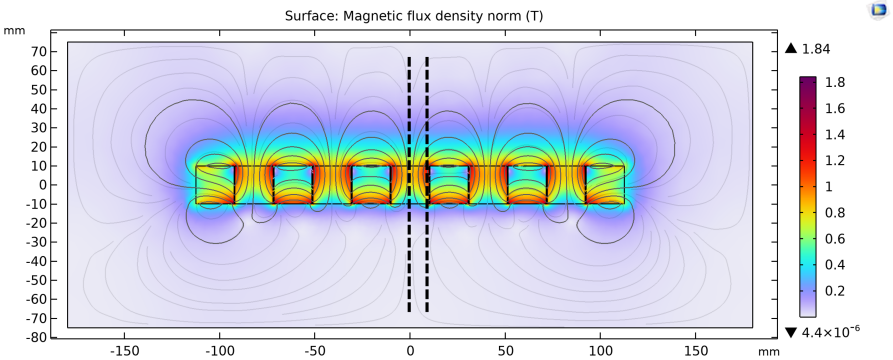

Figure 2.10: flux density in and around Halbach Array (2D).

In this simulation it is clear that the field lines above the array are much more concentrated than below. Also, the colors above the array indicate a higher flux density outside of the magnet above the array, than underneath it. The values were evaluated across the dashed, black cutlines, at the center and near the side of the center magnet.

In figure 2.11a the flux density (blue), gradient (red), and the gradient magnetic field intensity (green), through the center of the middle magnet is shown, and figure 2.11b shows it at $0.5\,\mathrm{mm}$ from the edge of the middle magnet, as previously indicated with the dashed lines in figure 2.10. The magnet is located between [40, 60]mm along the arc length on the horizontal axis.

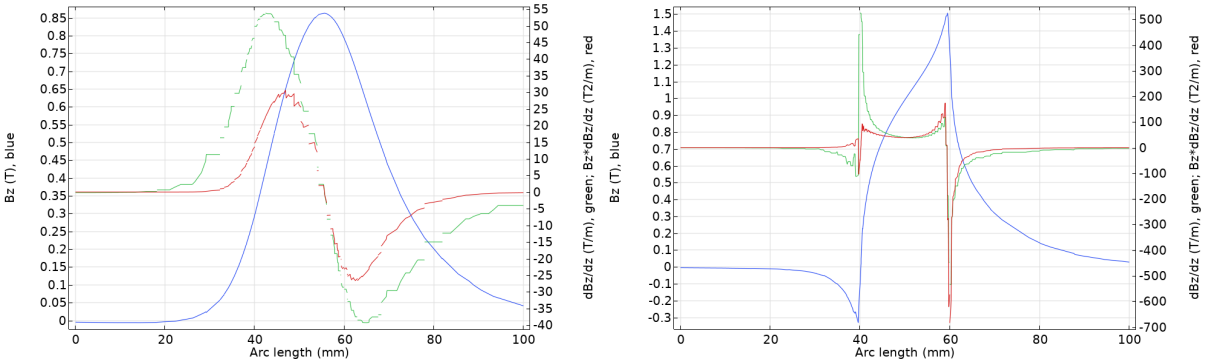

(a) Through the center of the middle magnet.

(b) 0.5mm to the inside of the side edge of the middle magnet.

Figure 2.11: Magnetic flux density (blue), gradient (green), and the gradient magnetic field intensity (red) of a Halbach Array. The magnet's surface is located between $[40, 60]\ \mathrm{mm}$.

It is clear that the peak in magnetic flux density is shifted to the right as compared to the magnet's location, and that the decay in the magnetic flux density is less steep on the right side. The peak of the gradient actually falls outside of the magnet surface, offering a larger gradient than for the previous examples. It can be concluded that the Halbach Array succeeds in increasing the absolute magnetic flux density, but in the left graph it is clear that the gradient magnetic field intensity does not exceed that of a single cylindrical magnet. On the positive side, the working distance is longer than that found for the previous configurations.

In the right figure, near the side of the center magnet, the peaks are very large: the gradient magnetic field intensity at the surface is $682\,\mathrm{T}^2\,\mathrm{m}^{-1}$. The decay is however extremely rapid: at a distance of $1\,\mathrm{mm}$, the remaining gradient magnetic field intensity is already down to $\sim 200\mathrm{T}^2\,\mathrm{m}^{-1}$. Since the decay is very large at this location, the working distance over which the magnetic force can be used is once again relatively shorter.

Magnetic Configuration	**Maximum $B_z \frac{\partial B_z}{\partial z}$ on magnet surface [$\mathrm{T}^2\,\mathrm{m}^{-1}$]**	**Distance from surface for which $B_z \frac{\partial B_z}{\partial z}$ > $10\,\mathrm{T}^2\,\mathrm{m}^{-1}$, [$\mathrm{mm}$]**
Halbach Array, at center	23.1	12.3
Halbach Array, near edge	682	9.0

Dual Halbach Array

The final configuration that will be studied, is a combination of the Halbach array and the Anti-Helmholtz configuration: it employs two Halbach arrays with facing strong sides. The resulting field from this configuration is shown in figure 2.12. Similar to the regular Anti-Helmholtz configuration, it is clear that the streamlines of the magnetic field are squeezed tightly between both arrays, while outside of the arrays, the flux density is very small.

Figure 2.13 shows the flux density (blue), gradient (green) and gradient magnetic field intensity (red) through the Dual Halbach array. The magnets are located at $[20, 40]$ and $[60, 80]\ \mathrm{mm}$ along the arc length on the horizontal axis. The left figure shows the graphs through the center of the middle magnet, while the right graph shows the graphs near the side of the central magnet.

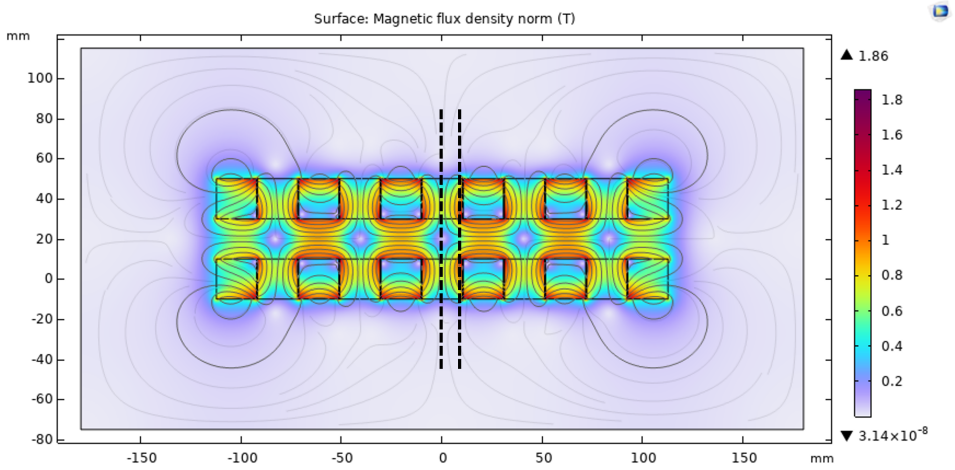

Figure 2.12: Dual Halbach array

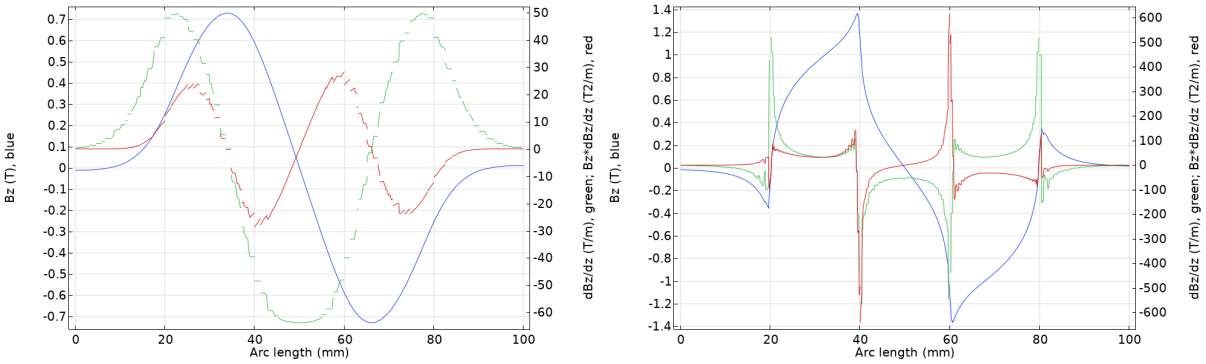

(a) Through the center of the middle magnet.

(b) 0.5mm to the inside of the side edge of the middle magnet.

Figure 2.13: Magnetic flux density (blue), gradient (green), and the gradient magnetic field intensity (red) of a Dual Halbach Array. The magnets are located between $[20, 40]$ and between $[60, 80]$ mm on the arc length.

The outcomes of the gradient magnetic field intensity of the left figure show smaller absolute values than previously found, thus it seems not to improve the magnetic force that can be generated. The right figure shows very slim, tall peaks. While the maximum value at the surface reaches $641\,\mathrm{T^2\,m^{-1}}$, at a distance of $1\,\mathrm{mm}$ from the surface the factor has already decreased to approximately $150\,\mathrm{T^2\,m^{-1}}$. Again, due to rapid decay of the peak, the working distance is more limited towards the side of the magnet.

Magnetic Configuration	**Maximum $B_z \frac{\partial B_z}{\partial z}$ on magnet surface [$\mathrm{T^2\,m^{-1}}$]**	**Distance from surface for which $B_z \frac{\partial B_z}{\partial z}$ > $10\,\mathrm{T^2\,m^{-1}}$, [mm]**
Dual Halbach Array, at center	28.6	7.5
Dual Halbach Array, near edge	641	6.8

2.2.1. Overview of the magnetic field factor

In table 2.1 an overview of the two indicators of all magnetic field configurations is given: the gradient magnetic field intensity on the surface of the magnet, and the distance from the magnet surface for which the gradient magnetic field intensity has decayed to $10\,\mathrm{T^2\,m^{-1}}$, indicating the height up to which the gradient magnetic field intensity is still of large enough value to induce a significant magnetic force.

The Halbach Rings generate the smallest magnetic product, and the shortest working distance. For all other configurations a large difference exists between the gradient magnetic field intensity at the center and close to the edge of the magnet. This difference is smallest for the single cylindrical magnet. The working distance at the center is always longer than near the side of the magnet. The Halbach Array

Magnetic Configuration	Maximum $B_z \frac{\partial B_z}{\partial z}$ on magnet surface [$\mathrm{T^2\,m^{-1}}$]	Distance from surface for which $B_z \frac{\partial B_z}{\partial z} > 10\,\mathrm{T^2\,m^{-1}}$, [mm]
Cylindrical ($t = 20\,\mathrm{mm}$), at center	41.1	6.8
Cylindrical ($t = 20\,\mathrm{mm}$), near edge	143	2.3
Anti-Helmholtz, at center	39.6	6.1
Anti-Helmholtz, near edge	200	2.0
Anti-Helmholtz Rings, at center	18.5	2.1
Anti-Helmholtz Rings, near edge	8.8	N/A
Halbach Array, at center	23.1	12.3
Halbach Array, near edge	682	9.0
Dual Halbach Array, at center	28.6	7.5
Dual Halbach Array, near edge	641	6.8

Table 2.1: Magnetic field factor indicator values for studied configurations.

configurations can generate the largest gradient magnetic field intensity close to the edge of the magnet, but at the cost of a lower intensity at the center. The working distance of this configuration is enhanced compared to the other configurations. The single cylindrical magnet offers a slightly higher gradient magnetic field intensity at the center, and a slightly longer working distance than the Anti-Helmholtz configuration.

2.3. Magnetic field factor for optimal configuration of permanent magnets

For each configuration, except the Anti-Helmholtz Rings, it holds that the gradient magnetic field intensity on the surface is largest near the side edge of the magnet. However, near the sides of the magnet, the decay of this intensity occurs also much more rapidly, resulting in a very small height above the magnet at which the gradient magnetic field intensity is of sufficient size to induce a significant magnetic force. Thus, a trade-off exists between the absolute gradient magnetic field intensity that can be achieved at the magnet surface, and how far from the magnet a sufficient magnetic force can still be induced.

Due to lack of availability of cubic and block magnets of high magnetic grade, and due to the increased complexity of this configuration, this is not the configuration of choice for the small, static MagLev experiments. Thus, disc magnets, stacked in an array to create a cylindrical magnet, will be used in the static MagLev setup. However, it should be noted that the optimal choice of magnetic configuration depends on the scale and application in which the magnets are applied.

Since the field above the center of the magnet and towards the edge of the magnet differs significantly, the gradient magnetic field intensity is not uniform at a certain height above the magnets. Because of this, a custom-designed magnet should be developed to be able to obtain a magnetic field which can be applied in a continuous MDS process, as the magnet in the patent by Polinder and Rem [61] for the MDS of plastic.

Finally, the first subquestion can be answered after this section:

> SQ1: What gradient magnetic field intensity can be generated using permanent NdFeB magnets and what is the optimal configuration?

The optimal configuration depends on the exact application that needs to be performed. For the case of small-scale magnetic levitation, using disc/cylindrical magnets (in an array) is the simplest, most easily available, and cheapest option, generating a gradient magnetic field intensity up to $41\,\mathrm{T^2\,m^{-1}}$.

3

Estimated solution properties and apparent density from literature data

In this chapter the properties of a paramagnetic solution will be discussed, as reported in the literature. The paramagnetic solution of choice is $MnCl_2$, which is used most often in the literature and appears to be capable of achieving an apparent density higher than the density of graphite. The properties that will be studied are the density ρ_m and magnetic susceptibility χ_m of the $MnCl_2$ solution.

$$\rho_s = \rho_m + \frac{\chi_m - \chi_s}{g\mu_0}(\vec{B} \cdot \vec{\nabla})\vec{B}$$

After these properties have been identified from literature, the force of gravity and the magnetic force that act on the liquid can be calculated, from which the apparent density ρ_s can be determined. This leads us to the following subquestion, that will be addressed in this chapter:

> SQ2: What density and magnetic susceptibility of $MnCl_2$ solutions are reported in the literature, are these sufficient for MagLev of graphite?

3.1. Reported density and magnetic susceptibility of $MnCl_2$ solutions

The magnetic solution most commonly used for magnetic density separation is $MnCl_2$, due to its affordability, high solubility, and relatively strong magnetic susceptibility. Therefore, $MnCl_2$ will be the solution of choice for this research.

The density of $MnCl_2$ solutions as a function of concentration has been previously investigated by Herrington, and by Rard and Miller [26, 63]. Both sources report the same densities as a function of the molality of $MnCl_2$ in the solution. The findings by Rard and Miller [63] are displayed in figure 3.1. By increasing the concentration up to $5.0929\,\mathrm{mol\,L^{-1}}$, a density of $1.49\,\mathrm{g\,cm^{-3}}$ can be achieved.

The magnetic susceptibility of $MnCl_2$ was measured by Egami et al. [15], and other values were used in calculations by Mirica et al. [50] and Miura et al. [51], taken from the CRC Handbook of Chemistry and Physics [41]. These sources report either the molar magnetic susceptibility of $MnCl_2$ ($\chi^M_{\mathrm{MnCl_2}}$), or the dimensionless magnetic susceptibility of $MnCl_2$ solutions ($\chi^V_{\mathrm{solution}}$).

The dimensionless magnetic susceptibility can be calculated from the molar magnetic susceptibility according to Egami et al. [15] through the equation below. In this equation, the dimensionless magnetic susceptibility of water is taken to be $\chi^{\mathrm{V}}_{\mathrm{H_2O}} = -9.05 \cdot 10^{-6}$ [10].

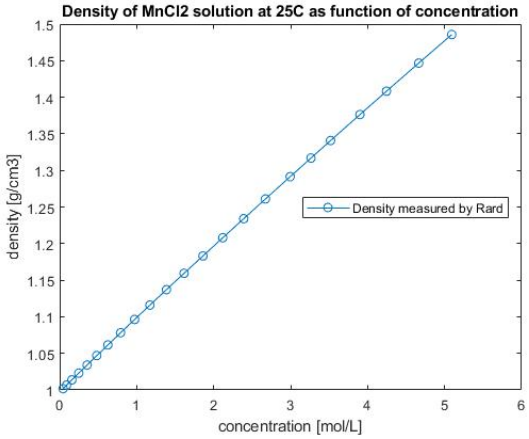

Figure 3.1: Density of $MnCl_2$ solutions as a function of concentration, as measured by Rard and Miller [63].

$$\chi^{\mathrm{V}}_{\mathrm{solution}} = \chi^{\mathrm{V}}_{\mathrm{H_2O}} + \chi^{\mathrm{M}}_{\mathrm{MnCl_2}} \cdot [\mathrm{MnCl_2}]$$

For the maximum solubility of $MnCl_2$, which is reported to be at $739\,\mathrm{g\,L^{-1}}$ at $20°\mathrm{C}$ by the supplier, Sigma Aldrich [68], and a molar mass of $M_{\mathrm{MnCl_2}} = 125.844\,\mathrm{g\,mol^{-1}}$, the maximum achievable magnetic susceptibility can also be calculated. The molar magnetic susceptibility, and the maximum dimensionless magnetic susceptibility that can be achieved at the saturation concentration of $MnCl_2$ in solution according to each source are displayed in table 3.1.

Source	Molar magnetic susceptibility $\chi^{\mathrm{M}}_{\mathrm{MnCl_2}}$	Max. magnetic susceptibility at saturation concentration $\chi^{\mathrm{V}}_{\mathrm{solution,max}}$
Egami [15]	$1.8 \cdot 10^{-4}\mathrm{L\,mol^{-1}}$	$1.048 \cdot 10^{-3}$
Mirica [50]	$1.435 \cdot 10^{-5}\mathrm{L\,mol^{-1}}$	$7.522 \cdot 10^{-5}$
Miura [51]	$1.188 \cdot 10^{-4}\mathrm{L\,mol^{-1}}$	$6.8859 \cdot 10^{-4}$

Table 3.1: Magnetic susceptibilities according to three different sources.

Since these values differ a lot, no definitive conclusion can be drawn about the actual magnetic susceptibility of a $MnCl_2$ solution. The magnetic susceptibility of a $MnCl_2$ solution scales with the $MnCl_2$ concentration in the solution, and is plotted for the values given by all three sources in the graph below:

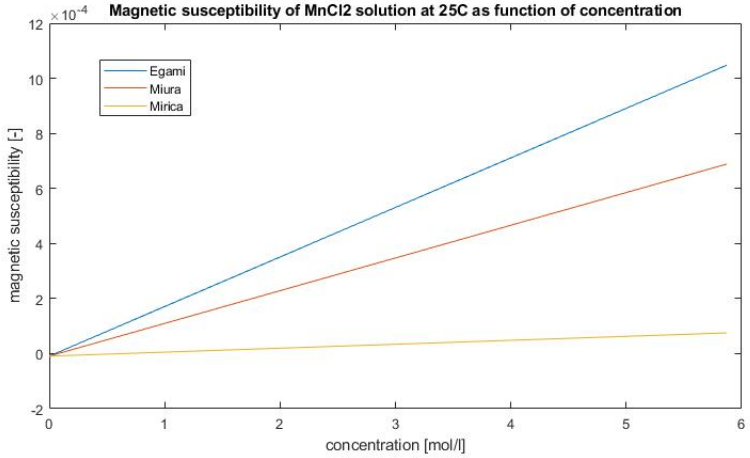

Figure 3.2: Magnetic susceptibility of a $MnCl_2$ solution as a function of the molarity, according to Egami [15], Miura [51] and Mirica [50].

3.2. Estimated apparent density according to literature data

From the magnetic susceptibility, the magnetic force that will act on the liquid can be determined. The calculation of this force is given by Mirica et al. [50] by the following equation:

$$\overrightarrow{F}_{mag} = \frac{(\chi_s - \chi_m)}{\mu_0} V(\overrightarrow{B} \cdot \overrightarrow{\nabla})\overrightarrow{B} \tag{3.1}$$

This equation shows that the magnetic force scales with the magnetic flux density B and the spatial derivative thereof. For a 3D Cartesian coordinate system with the z-axis aligned with the vector of gravity $\vec{g} = (0, 0, -g)$, the equation simplifies to the following:

$$\overrightarrow{F}_{mag} = \frac{(\chi_s - \chi_m)}{\mu_0} V(B_x \frac{\partial B_z}{\partial x} + B_y \frac{\partial B_z}{\partial y} + B_z \frac{\partial B_z}{\partial z}) = \frac{(\chi_s - \chi_m)}{\mu_0} V(B_z \frac{\partial B_z}{\partial z}) \tag{3.2}$$

In the previous chapter, it was found that the maximum absolute gradient magnetic field intensity that can be achieved at the surface of a cylindrical magnet is the following:

$$B_z \frac{\partial B_z}{\partial z} = -41.1\,\mathrm{T}^2\,\mathrm{m}^{-1}$$

Apart from the magnetic force, gravity also works on the system. These two forces combined determine the equilibrium height at which the particles will levitate inside the liquid. In a stationary fluid, the object will come to rest at the height where these forces are equal and opposite:

$$\overrightarrow{F}_g + \overrightarrow{F}_{mag} = (\rho_s - \rho_m) V \overrightarrow{g} + \frac{(\chi_s - \chi_m)}{\mu_0} V(B_z \frac{\partial B_z}{\partial z}) = 0 \tag{3.3}$$

Given the density from Rard [63] and magnetic susceptibility as a function of $MnCl_2$ concentration as reported by Egami [15], Mirica [50] and Miura [51], the apparent density as a function of the factor $B_z \frac{\partial B_z}{\partial z}$ that is present outside the surface of the magnet, can be calculated through equation 3.4.

$$\rho_s = \rho_m + \frac{\chi_m - \chi_s}{g\mu_0} (B_z \frac{\partial B_z}{\partial z}) \tag{3.4}$$

Since the magnetic susceptibility of graphite is usually reported to be negative and very small, the magnetic susceptibility of the suspended particles in the equation is taken to be 0. Plots of the apparent densities that can be levitated are displayed in figure 3.3.

After this chapter, the following research question can be answered:

> SQ2: What density and magnetic susceptibility of $MnCl_2$ solutions are reported in the literature, are these sufficient for MagLev of graphite?

The density of $MnCl_2$ as a function of the concentration have been described to be up to $1.5\mathrm{g\,cm}^{-3}$ for a solution close to saturation concentration. Values for magnetic susceptibility are ambiguous, as the minimum and maximum reported molar magnetic susceptibilities are reported to be $\chi^{\mathrm{M}}_{\mathrm{MnCl_2,Mirica}} = 1.435 \cdot 10^{-5}\mathrm{L\,mol}^{-1}$ and $\chi^{\mathrm{M}}_{\mathrm{MnCl_2,Egami}} = 1.8 \cdot 10^{-4}\mathrm{L\,mol}^{-1}$, respectively.

For the levitation of graphite, the apparent density that can be achieved within the liquid should be at least the density of graphite: $\rho_{\mathrm{graphite}} = 2.25\mathrm{g\,cm}^{-3}$. Assuming the magnetic susceptibility as reported by Mirica, the apparent density will not be sufficient to ensure levitation of graphite. However, if the magnetic susceptibility is as high as reported by Miura and Egami, not only the graphite can be levitated in the solution, but also some of the cathode material, at a lower equilibrium height.

Since it remains inconclusive whether MagLev of graphite can be achieved in the $MnCl_2$ solution with permanent magnets, further research is required, which will be executed in the following two chapters.

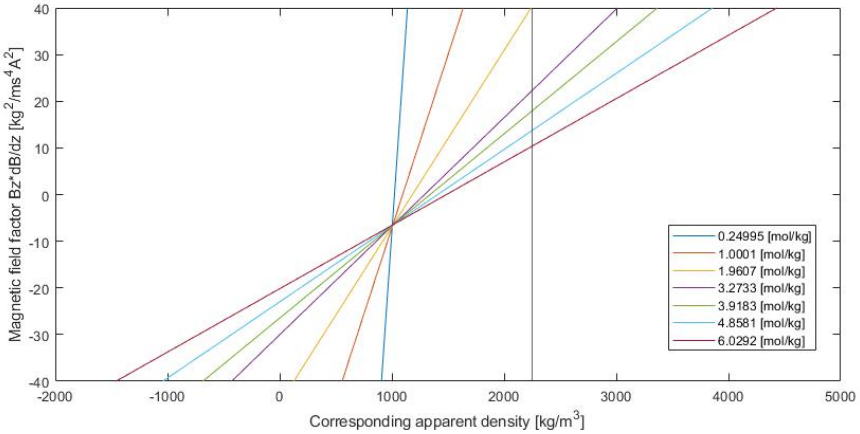

(a) The highest apparent density that can be achieved within the solution at saturation concentration, is 4978$\mathrm{kg\,m^{-3}}$, according to Egami [15].

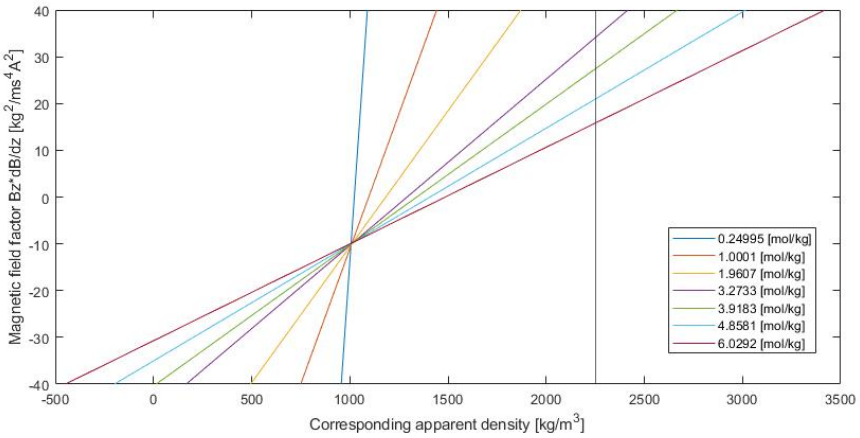

(b) The highest apparent density that can be achieved within the solution at saturation concentration, is 3781$\mathrm{kg\,m^{-3}}$, according to Miura [51].

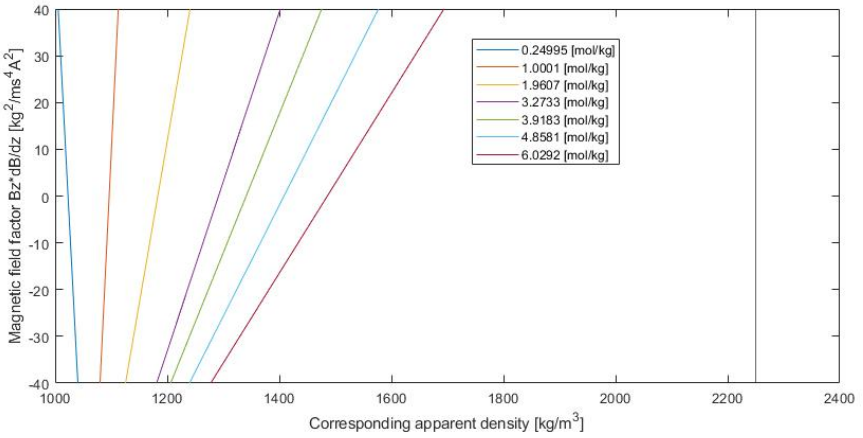

(c) The highest apparent density that can be achieved within the solution at saturation concentration, is 1737$\mathrm{kg\,m^{-3}}$, according to Mirica [50].

Figure 3.3: Apparent densities that can be achieved near the stack of permanent magnets, given a magnetic susceptibility of 0 of the suspended particles.

4

Preparation of the solution, experimental characterization and density measurements

This chapter focuses on the practical implications of handling $MnCl_2$ and preparing samples of $MnCl_2$ solutions at different concentrations. Since dissolution of the beads turned out to be more complicated than anticipated, and because the $MnCl_2$ was of limited purity, characterization experiments were performed to determine the elemental composition of the $MnCl_2$ and the manganese concentration. Finally, the density ρ_m of all solution samples was measured.

$$\rho_s = \rho_m + \frac{\chi_m - \chi_s}{g\mu_0}(\vec{B} \cdot \vec{\nabla})\vec{B}$$

At the end of this chapter, the following research question will be addressed:

> SQ3: What methods are required to prepare a transparent solution that does not precipitate, what issues related to the material are encountered, and what is the elemental composition and density of the solution?

4.1. Preparation of the solution and related challenges

For the experiments, 2kg of beads of anhydrous $MnCl_2$ of a purity of 98wt.% were purchased from Sigma-Aldrich, at a cost of €81. From this, 2.7 litres of $MnCl_2$ solution can be produced at the saturation concentration. For the static MagLev experiments at small scale only a few mL are required. Upon handling and dissolving the $MnCl_2$ beads in MilliQ, several problems were encountered.

It was aimed to prepare solutions of $MnCl_2$ by creating samples with concentrations of 20, 40, 60, 80 and 100% of the saturation concentration, which was reported to be $739\,\mathrm{g\,L^{-1}}$ at 20°C [68]. These solutions will be referred to as C-20, C-40, C-60, C-80 and C-100, respectively. An overview of the concentrations per sample is given in table 4.1. It was also attempted to prepare a solution at a concentration of 120%, but at this concentration a significant amount of the beads remained fully undissolved in suspension, indicating the saturation concentration had indeed been surpassed.

However, dissolving the $MnCl_2$ beads turned out to not be very straightforward, and the high solubility of $739\,\mathrm{g\,L^{-1}}$ at $20°$C that was indicated by the supplier could not be achieved without any additional steps. Upon trying to dissolve the beads in Milli-Q even at very low concentrations, an opaque, brown suspension was formed, the mixture heated up, and the gas pressure built up when the mixture was

Sample name	C-20	C-40	C-60	C-80	C-100
Concentration [$\mathrm{g}/100\mathrm{mL}$]	14.78	29.56	44.34	59.12	73.90
Molarity [$\mathrm{mol\,L^{-1}}$]	1.17	2.35	3.52	4.70	5.87

Table 4.1: Names, mass fraction and molality of each solution sample.

sealed. Initially, it was assumed the brown particles were MnO_2, indicating oxidation of the Mn^{2+} ion into Mn^{4+}, which might be prevented by lowering the pH, or decreasing the oxygen content in the water.

Several methods were performed to dissolve the turbidity: (ultrasonic) stirring at elevated temperature, lowering the pH by adding HNO_3 or HCl, and by pre-cooking the water for a few minutes to decrease the oxygen content in the water. Unfortunately, these efforts did not cause the $MnCl_2$ suspension to better dissolve and result into a clear solution.

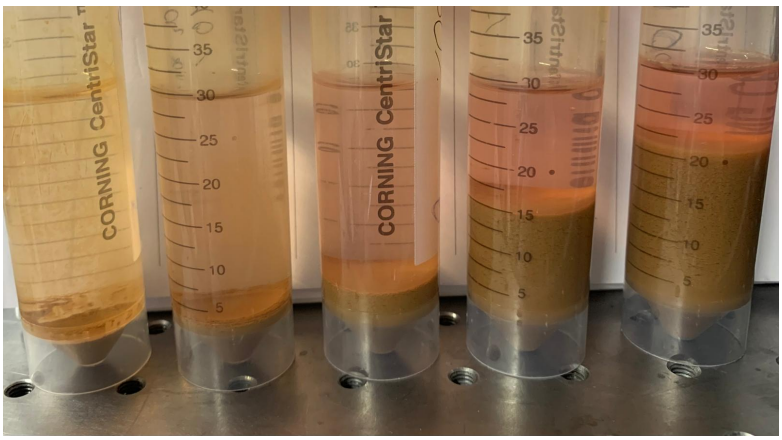

Figure 4.1: Vials of $MnCl_2$ suspensions at weight fractions of 20, 40, 60, 80 and 100% of the saturation concentration, sedimented due to gravity after one day.

Since the turbid suspensions were not suitable to apply in the experiments, due to lack of visibility of battery material particles inside, and because the suspended, undissolved particles settle over time due to gravity, these particles had to be removed. To achieve this, three methods were employed: filtration, centrifugation, and sedimentation by gravity. After the suspended particles had been removed, a clear, pink-red solution remained, which was darker red with increasing concentration, as can be seen in figure 4.1. To limit the number of process steps and parameters, sedimentation by gravity was used for the preparation of samples for all following experiments.

In hindsight, it was found that oxidation of Mn^{2+} ions could not be overcome by only lowering the pH, but also addition of a reducer was required. It turned out that adding a combination of H_2O_2 and HCl led to a clear, pale pink solution, similar of color to the remaining supernatant after sedimentation of the suspension. This indicates oxidation of the Mn^{2+} has occurred into Mn^{3+} and Mn^{4+}, by reacting with O_2 and OH^- from the solution in neutral to basic environment, for instance into MnO(OH), $MnO(OH)_2$ or $Mn(OH)_3$. By adding H_2O_2 as a reducer and HCl to provide an acidic environment, this reaction could be reversed. Unfortunately, this fact was only discovered after all experiments had been conducted, and this method for dissolving the beads was thus not applied to the solutions used in the experiments.

The pale pink solution was identified to be a solution of the $Mn(H_2O)_6{}^{2+}$ ion, which is known to be pale pink. Manganese ions in other oxidation states have different colors: Mn^{7+} is purple, Mn^{6+} is blue, Mn^{5+} is green, Mn^{4+} is brown and Mn^{2+} is colorless.

Later, during the characterization experiments, it was noted that the beads swell due to moisture from the air. This happens because the anhydrous form of $MnCl_2$ is relatively unstable and very hygroscopic, compared to the tetrahydrate variant: $MnCl_2(H_2O)_4$. Therefore, the beads should only be exposed to inert atmospheres, to remain anhydrous. Since the jar containing the beads has been opened under an atmosphere that was not inert, the beads have been exposed to moisture from the air, and therefore been partially hydrated. After this has occurred, the water content present in the beads is unknown,

but no longer zero. As a result, the molar mass of the hydrated beads has increased, and the number of moles of $MnCl_2$ that is present in a certain mass of beads, can no longer be exactly determined.

By assuming our initial material is of the anhydrous form with a molar mass of $M_{\mathrm{MnCl_2}} = 125.844\,\mathrm{g\,mol^{-1}}$, instead of the tetrahydrate with a molar mass of $M_{\mathrm{MnCl_2(H_2O)_4}} = 197.90\,\mathrm{g\,mol^{-1}}$, the number of moles $MnCl_2$ weighed, could be up to $100\% - \frac{125.844}{197.90} = 36.4\%$ lower, if the material is already fully hydrated. However, since the exposure time to air has been relatively short and the volume of air that enters the jar is relatively small compared the 2 kgs of $MnCl_2$ beads in the jar, it is assumed the fraction of the beads that is hydrated, is negligible. So, for all samples that were prepared, it was still assumed that the mass of beads weighed consists of pure anhydrous $MnCl_2$.

4.2. Elemental composition and manganese concentration

Since the beads had a purity of 98 wt.%, characterization methods were performed to reveal the impurities that were present in the $MnCl_2$ beads, the solution, and the deposits from the samples, and to determine the manganese concentration of each solution sample.

For the characterization of solid material, X-ray diffraction (XRD) and X-ray fluorescence (XRF) were performed. Before conducting the characterization of the beads, they had to be crushed, which was done using mortar and pestle. The sediment was dried by air before XRD and XRF characterizations could be performed. The clear, pale pink-red supernatant that could be taken after sedimentation was characterized using inductively coupled plasma-optical emission spectrometry (ICP-OES) measurements. First one solution sample at saturation concentration was analyzed. Later, the manganese content in the samples C-20, C-40, C-60, C-80 and C-100 was investigated.

Elemental composition of the $MnCl_2$ beads

The results from the XRF measurements on the $MnCl_2$ beads can be found in table 4.2. The measurements suggest a combined purity of 99.2 wt.% of Mn and Cl, and only very small fractions of other elements.

Component:	Cl	Mn	K	Fe	Ba	Ca	Si	Sr	S
Concentration (wt.%):	57.558	41.645	0.394	0.248	0.057	0.052	0.029	0.024	0.005
Absolute error (wt.%):	0.1	0.1	0.02	0.01	0.007	0.007	0.005	0.004	0.002

Table 4.2: Results XRF measurements $MnCl_2$ beads.

The mass fractions that were found can be converted into molar concentrations, which gives us the following values in the table below:

Component	Mass fraction (wt.%)	Molar mass (g/mol)	Molality (mol/kg)
Cl	57.558	35.453	16.24
Mn	41.645	54.938	7.58

A ratio of 2:1 is expected in the molality of Cl to Mn. However, the actual ratio is $16.24/7.58 = 2.14$. This deviation could be attributed to measurement errors due to the particle size of the beads. Ideally, powders of a particle size of at most $10\mu m$ can be accurately analyzed. The beads were crushed manually with mortar and pestle, but this method likely leaves some larger particles in the powder, which could lead to local measurement biases.

The full reports from the XRD and XRF analyses can be found in Appendix A and showed a pattern very similar to that of $MnCl_2(H_2O)_4$ as measured by Bouteiller et al. [11]. No other peaks related to other compounds could be identified, indicating no other compounds with a concentration larger than 1 wt.% were present in the sample.

It was already discovered that the assumption that the beads were purely anhydrous $MnCl_2$ was no longer valid. However, while performing the analyses, it was soon noted that the beads swell due to moisture from the air, which was not yet observed for the beads in the jar. Moreover, since the beads are exposed to a relatively large fraction of air for a long period of time during the XRD characterization, and only a relatively small quantity of air in the jar for storage, it is assumed to be more likely that the beads become hydrated mostly during the XRD analysis, rather than before in the jar.

Elemental composition of the $MnCl_2$ solution

The results of the ICP-OES characterization measurements of a solution at saturation concentration are given in table 4.4. Again, almost purely Mn and Cl are found, and the presence of other elements is only very limited.

Component:	Cl	Mn	K	SO_4	Na	Ba	Ca	Mg	Sr	Li
Concentration ($\mathrm{mg\,kg^{-1}}$):	232073	192810	1846	1705	848	354	326	132	76	7

Table 4.3: Results ICP-OES measurements $MnCl_2$ solution at saturation concentration.

These results show that the molar ratio between Mn and Cl is as follows:

Component	**Mass fraction ($\mathrm{mg\,kg^{-1}}$)**	**Molar mass ($\mathrm{g\,mol^{-1}}$)**	**Molality ($\mathrm{mol\,kg^{-1}}$)**
Cl	232073	35.453	6.546
Mn	192810	54.938	3.510

The ratio of Cl compared to Mn is $6.546/3.510 = 1.84$. Other than for the ratio of Mn compared to Cl for the beads, the concentration of Cl is lower than that would be expected. This could indicate that the Mn^{2+} ions might dissolve better from the beads into the Milli-Q than the Cl^- ions, and thus indeed a higher presence of Mn than Cl in the solution, or that Cl has reacted to a gas and thereby disappeared from the suspensions.

Further, for samples of each concentration, an analysis was performed of the manganese mass fraction in each sample. The results are displayed in table 4.4.

Sample:	**C-20**	**C-40**	**C-60**	**C-80**	**C-100**
Mass fraction Mn (wt.%):	5.74	10.50	14.29	17.74	20.34
Molality Mn ($\mathrm{mol\,kg^{-1}}$)	1.04	1.91	2.60	3.23	3.70
Increase molality per sample ($\mathrm{mol\,kg^{-1}}$)	1.04	0.87	0.69	0.63	0.47

Table 4.4: Results ICP-OES measurements Mn-concentration of all samples.

Elemental composition of the $MnCl_2$ sediment

Finally, XRD and XRF characterizations were performed on the sediment remaining after precipitation. The XRD results can be found in Appendix A. These results indicate a very high purity of $MnCl_2(H_2O)_4$, while two other peaks appeared as compared to the initial beads, for which the compound(s) could not be identified. The high purity of $MnCl_2(H_2O)_4$ in the sediment might indicate that the saturation concentration of the $MnCl_2$ has been surpassed.

Component:	Cl	Mn	K	Ba	Ca	Si	Sr	S
Concentration (wt.%):	51.573	48.07	0.176	0.077	0.044	0.038	0.015	0.007
Absolute error (wt.%):	0.1	0.2	0.01	0.008	0.006	0.006	0.004	0.002

Table 4.5: Results from XRF analysis of sediment.

The results from the XRF analysis are shown in table 4.5. These results show the same impurities as the analysis of the beads from table 4.2, but indicate a relatively larger concentration of Mn compared to Cl. This could indicate that the Cl dissolves into Cl^- ions more easily than the Mn dissolves into Mn^{2+} ions, or that the previous characterization of the beads was indeed inaccurate. Further, the concentration of the impurities is relatively smaller compared to that in the beads, indicating these impurities dissolve relatively more readily into ions than the $MnCl_2$ itself, or they have reacted out of the suspension. In particular Fe seems to be very easily soluble or reactive, as this compound is not measured anymore in the sediment.

When converting the mass fractions into molality again, the following values are obtained:

Compound	**Mass fraction (wt.%)**	**Molar mass ($\mathrm{g\,mol^{-1}}$)**	**Molality ($\mathrm{mol\,kg^{-1}}$)**
Cl	52.573	35.453	14.55
Mn	48.07	54.938	8.75

The ratio between Cl and Mn is $14.55/8.75 = 1.66$. Just as for the solution, the Mn concentration is relatively higher than that of the beads. Since a pressure increase was observed upon dissolving the beads, this strengthens the suspicion that some of the Cl has reacted out of the mixture through gas formation.

4.3. Density measurements

In this section the density of the samples will be measured and compared to the values reported in literature. Two methods were performed to study the density of the solutions for all different concentrations. Firstly, an empty vial was weighed and tared in a Mettler-Toledo lab scale. Then, a volume of $MnCl_2$ solution of a certain concentration was added, as precisely as possible up to a volume of $25\,\mathrm{mL}$. The change in weight of the partially filled vial was then weighed again. Since the volume indication on the vials is known to be quite inaccurate, this method was used to obtain an indication of the order of magnitude of each solution. To obtain a more precise and reliable value for the density of the samples, the ”DMA 5000 Density Meter” by Anton Paar was used for each different concentration.

The densities that were found, are displayed in table 4.6 below. Since the density and molality of each sample are now known, the molarity can also be determined, as calculated in table 4.7.

Sample	**Concentration** $(\mathrm{mol\,L^{-1}})$	**Volume** (mL)	**Mass** (g)	**Density (estimated)** $(\mathrm{g\,mL^{-1}})$	**Density (AP densitymeter)** $(\mathrm{g\,mL^{-1}})$
C-20	1.17	27.5	30.6983	1.116	1.11236
C-40	2.35	25.0	30.8156	1.233	1.22023
C-60	3.52	25.0	33.4723	1.339	1.33973
C-80	4.70	25.0	36.2678	1.451	1.45922
C-100	5.87	22.5	33.7223	1.499	1.54096

Table 4.6: Density of each sample, as estimated through mass/volume ratio, and measured by the Anton Paar Densitymeter.

Sample	**Density** $(\mathrm{kg\,L^{-1}})$	**Molality Mn** $(\mathrm{mol\,kg^{-1}})$	**Molarity Mn** $(\mathrm{mol\,L^{-1}})$	**Fraction** $(\%)$
C-20	1.11236	1.04	1.16	19.8
C-40	1.22023	1.91	2.33	39.7
C-60	1.33973	2.60	3.48	59.3
C-80	1.45922	3.23	4.71	80.2
C-100	1.54096	3.70	5.70	97.3

Table 4.7: Molarities corresponding to each sample from the density and molality of the samples, and how these compare to the saturation concentration.

The densities previously found by Rard and Miller [63] are displayed in the blue graph in figure 4.2, and are compared to the data experimentally found from the table above by the ’o’s’ in the graph. When comparing these datasets, it can be seen that the experimental result align well with the findings by Rard and Miller [63], and the density measured of the C-100 sample can be linearly extrapolated from their data. That further indicates that the saturation concentration was indeed not yet surpassed. Thus, it can be concluded that the densities measured and the manganese content measured correspond well to the expected values from literature.

Further, the concentration of manganese in the samples as fractions of the saturation concentration turns out to be quite close to the intended values, indicating the assumption that the hydration of the beads is indeed negligible and that practically all manganese is dissolved.

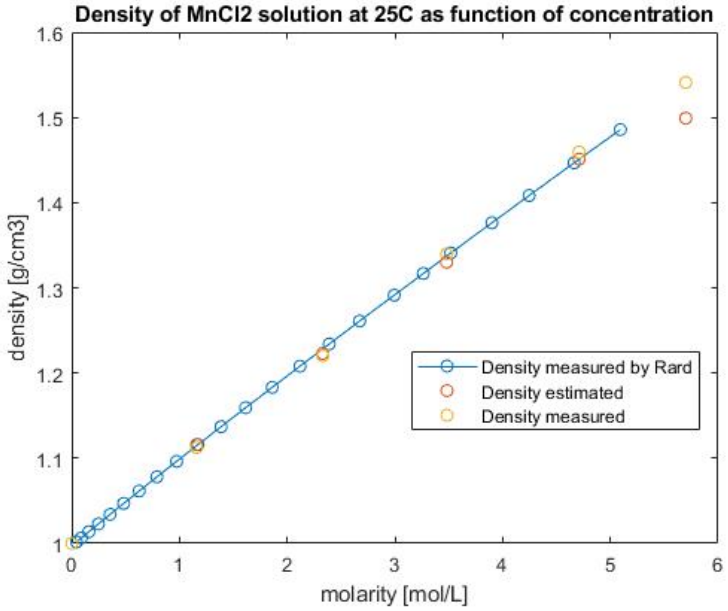

Figure 4.2: Densities measured by Rard and Miller (blue), experimentally found (orange, yellow).

4.4. Practical attainability of intended concentrations

In this chapter, it was intended to prepare samples of $MnCl_2$ solutions at various concentrations. Issues were encountered in dissolving the $MnCl_2$ beads, and because partial hydration of the beads has very likely occurred. Nonetheless, the measured manganese concentrations and the density measurements indicate that the samples are very close to the intended concentrations. This indicates that the water content in the beads is in fact negligible, and the manganese dissolves readily from the beads and only a negligible fraction of the manganese gets lost in the preparation of the solutions.

After this chapter, the following research question can be answered:

> SQ3: What methods are required to prepare a transparent solution that does not precipitate, what issues related to the material are encountered, and what is the elemental composition and density of the solution?

For the preparation of the samples, beads were dispersed in Milli-Q and stirred. A stable solution was achieved after letting the insoluble suspended particles sediment due to gravity. This could otherwise be achieved by adding H_2O_2 as a reducer under an acidic environment.

The solutions consist almost purely of $MnCl_2$ and only a negligible fraction of impurities. The density of the solutions vary approximately linearly with the molarity of the samples: from a density of $1.11\,\mathrm{kg\,L^{-1}}$ of sample C-20, to a density of $1.54\,\mathrm{kg\,L^{-1}}$ for sample C-100.

5

Magnetic pendant drop method for measuring the magnetic susceptibility

In this chapter, a method is developed to experimentally measure the magnetic susceptibility of a liquid, which was applied to determine the magnetic susceptibility χ_m of all samples.

$$\rho_s = \rho_m + \frac{\chi_m - \chi_s}{g\mu_0}(\vec{B} \cdot \vec{\nabla})\vec{B}$$

A straightforward, reproducible experimental setup is required for the measurement of the magnetic susceptibility of a liquid, as it became clear from chapter 3 that literature sources are in disagreement about the magnetic susceptibility of $MnCl_2$ solutions. The method that was developed, is an adjusted version of the pendant drop method, which will be first described in this chapter.

At the end of this chapter, the following research question will be addressed:

> SQ4: What method can be developed to measure the magnetic susceptibility of the solution, do the measured magnetic susceptibilities agree well with the values reported in literature, and what magnetic susceptibility of the solutions can be achieved?

5.1. Pendant drop method: measuring the ratio between gravity and surface tension

In pendant drop experiments, a drop is extruded below a needle, by which the shape of the drop is a result of the balance between surface tension forces at the surface of the drop, and gravity pulling the drop down. This is a method that has been studied since the 19th century, and following from the shape of the drop, the ratio between surface tension forces and gravity can be determined. For instance, Fordham [19] found a way to very precisely describe this ratio using only two variables from the shape of a pendant drop, as can be seen in figure 5.1a.

Further research into the pendant drop method has led to advanced developments in computational analysis of the shape and properties of pendant drops. One such research was performed by Berry et al. [9]. The research of Berry incorporates a full description of the shape of the pendant drop, as can be seen in figure 5.1b. The foundation of the computational analysis originates from the Young-Laplace equation, which relates the Laplace pressure across an interface with the curvature of the interface and the interfacial tension γ:

$$\gamma\left(\frac{1}{R_1} + \frac{1}{R_2}\right) = \Delta P = \Delta P_0 - \Delta\rho g z \tag{5.1}$$

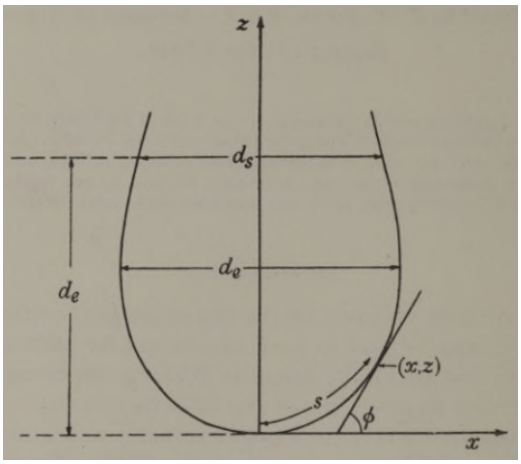

(a) Analysis of the shape of a pendant drop, by measuring only two variables. Reprinted from Fordham [19].

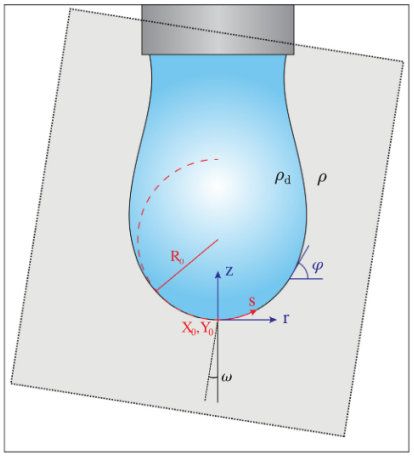

(b) A schematic of a pendant drop below a needle. The annotations show the associated variables used in the computational routine. Reprinted from Berry et al. [9].

Figure 5.1: Analysis of pendant drop shape to determine the Bond number and Interfacial Tension.

In this equation R_1 and R_2 are the principal radii of curvature, $\Delta P = P_{in} - P_{out}$ the Laplace pressure across the interface, $\Delta\rho$ the density difference between the drop phase and the continuous phase. When the needle is well aligned with the force of gravity, the shape of the drop should be axisymmetrical, and cylindrical coordinates can be applied, as shown in figure 5.1b: r, z, and tangent angle ϕ.

At the apex of the drop, at $z = 0$, the reference pressure is defined to be $\Delta P_0 = \frac{2\gamma}{R_0}$ and the hydrostatic pressure is $\rho g z$. The Bond number for a pendant drop is defined to be $\mathrm{Bo} = \frac{\rho g R_0^2}{\gamma}$. Given these conditions, the gravitational pressure difference at the apex can be expressed in terms of the Bond number:

$$\begin{aligned}\Delta P &= \frac{2\gamma}{R_0} - \rho g z \\ &= \frac{2\gamma}{R_0} - \frac{\mathrm{Bo}\cdot\gamma}{R_0^2}\cdot z \\ &= \frac{\gamma}{R_0}(2 - \mathrm{Bo}\cdot\frac{z}{R_0})\end{aligned}$$

Further, the interfacial tension (IFT) difference across the surface can be described using $\frac{1}{R_1} = \frac{d\phi}{ds}$ and $\frac{1}{R_2} = \frac{\sin\phi}{r}$.

$$\Delta P = \gamma(\frac{1}{R_1} + \frac{1}{R_2}) = \gamma(\frac{d\phi}{ds} + \frac{\sin\phi}{r})$$

When both expressions of the pressure difference are set equal to one another and are non-dimensionalized by dividing z, r and s by R_0, indicated with a bar, the following combined equation is obtained:

$$\begin{aligned}\gamma(\frac{d\phi}{ds} + \frac{\sin\phi}{r}) &= \frac{\gamma}{R_0}(2 - \mathrm{Bo}\cdot\frac{z}{R_0}) \\ R_0(\frac{d\phi}{ds} + \frac{\sin\phi}{r}) &= (2 - \mathrm{Bo}\cdot\frac{z}{R_0}) \\ \frac{d\phi}{d\bar{s}} + \frac{\sin\phi}{\bar{r}} &= 2 - \mathrm{Bo}\cdot\bar{z}\end{aligned}$$

From here, the full dimensionless system of equations to describe the shape of the drop can be derived:

$$\frac{d\phi}{d\bar{s}} = 2 - \mathrm{Bo} \cdot \bar{z} - \frac{\sin\phi}{\bar{r}} \tag{5.2a}$$

$$\frac{d\bar{r}}{d\bar{s}} = \cos\phi \tag{5.2b}$$

$$\frac{d\bar{z}}{d\bar{s}} = \sin\phi \tag{5.2c}$$

Further, a Matlab plugin was developed and made available by Berry et al. [9], which analyzes the shape of the drop and determines the IFT from the Bond number. The results of such an analysis is shown in figure 5.2a. From the shape of the drop interface, the software calculates the drop volume and surface area, the Bond number and the IFT.

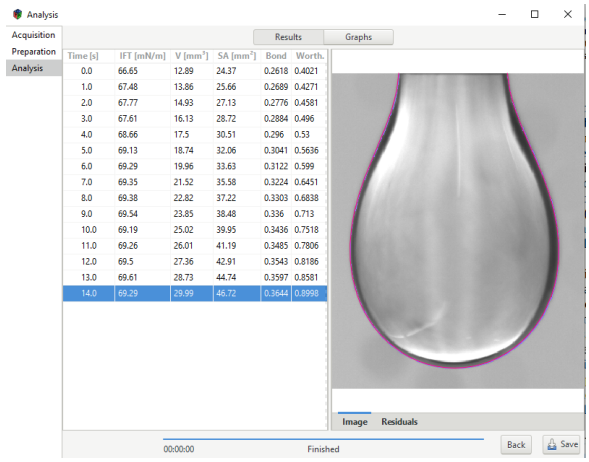

(a) Opendrop analysis of images of a drop of water of increasing drop volume.

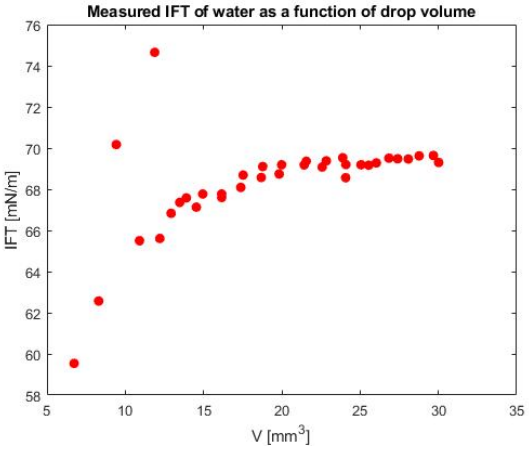

(b) Corresponding plot of measured IFT as a function of drop volume.

Figure 5.2: Results opendrop analysis.

One important fact to take into account from the surface tension measurements using the pendant drop method, is that the drop needs to be larger than a certain threshold size to provide accurate results. This is because for very small drops, the surface tension is dominant over the gravity, and a small change in the contribution of the force of gravity causes only very small deformations on the drop surface, which are difficult to accurately capture.

Berry et al. have indicated that the results for the surface tension measurements are reliable when the Worthington number is close to 1: $\mathrm{Wo} \sim 1$. The Worthington number describes the volume of the drop V_d, compared to the maximum volume V_{max} for which the drop is expected to fall from the needle, for a given interfacial tension, which can thus be no larger than 1. The maximum drop volume that can theoretically be sustained, was defined by Harkins and Brown [79] to be $V_{max} = \frac{\pi D_n \gamma}{\Delta\rho g}$, leading to the following definition of the Worthington number:

$$\mathrm{Wo} = \frac{\Delta\rho g V_d}{\pi\gamma D_n} \tag{5.3}$$

As can be seen in figure 5.2b, the calculated value for the IFT of water increases and converges to a value of approximately $69.5\,\mathrm{mN\,m^{-1}}$, with increasing drop volume and Worthington number, which is very close to the value reported in literature: $72\,\mathrm{mN\,m^{-1}}$. Thus, measurements need to be repeated for increasing drop volume, after which can be determined to what value the IFT converges.

A setup was built to perform the pendant drop experiments, which can be seen in figure 5.3a. Experiments were conducted to determine the IFT of the solutions for each concentration.

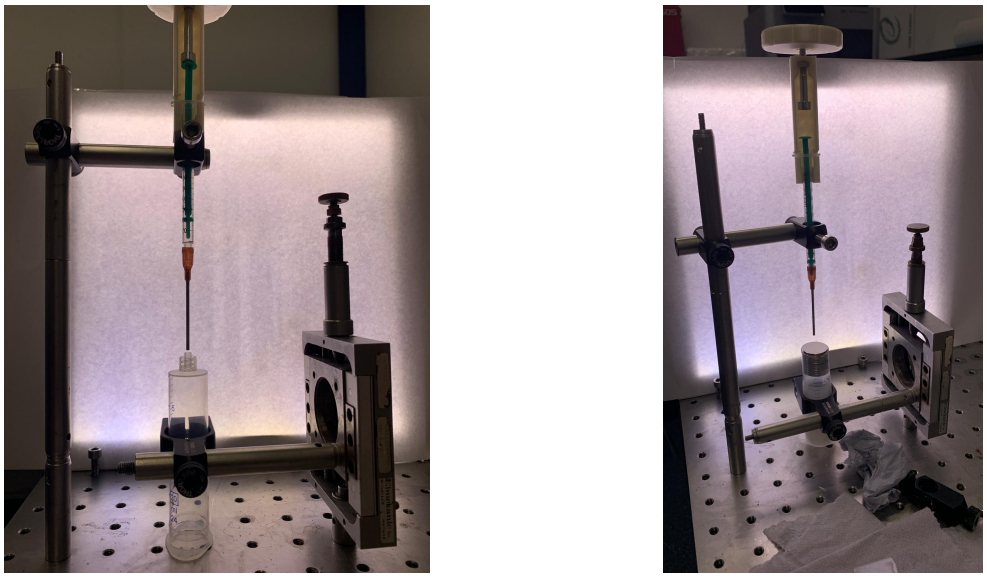

(a) Pendant drop experiments.

(b) Magnetic pendant drop experiments.

Figure 5.3: Setup for pendant drop experiments, with needle at fixed position aligned with the gravity and precise extrusion mechanism. Underneath a syringe is placed below the needle, in which the array of magnets can be placed and moved up closer and down further from the needle.

From the opendrop analysis, the IFT was measured for each sample. Plots taken directly from opendrop can be found in Appendix B. As convergence of the value of the IFT occurs for $\mathrm{Wo} \sim 1$, the following values of the IFT were determined for each concentration:

Sample	Water	C-20	C-40	C-60	C-80	C-100
IFT $(\mathrm{mN\,m^{-1}})$	69.5	73.5	76.5	81.0	85.5	87.5

These results indicate that increasing the $MnCl_2$ concentration leads to an increased IFT. Similar results have previously been found for various salts [34]. This can be explained due to the presence of the charged ions in the liquid, which have an even stronger interaction with the water molecules than the hydrogen bonds. Since the charged ions prefer to be surrounded by water, they are present in the bulk of the liquid, instead of at the surface. Because of this, the hydrogen molecules in the bulk interact more strongly with the ions and water molecules in the bulk, and less with the water molecules at the surface. As a results, the hydrogen bonds at the surface have an increased interaction among one another, leading to a higher IFT.

5.2. Magnetic pendant drop method for measuring the magnetic susceptibility

Besides the solution density, the second property of the $MnCl_2$ solution that dictates the apparent density that can be achieved, is the magnetic susceptibility, which will be determined in this section. An adjusted version of pendant drop measurements was developed to determine the magnetic susceptibility of the $MnCl_2$ solutions of different concentrations. The array of magnets was added to the pendant drop setup, as shown in figure 5.3b, which will be referred to as the magnetic pendant drop method.

With the addition of the magnet to the setup, not only the force of gravity acts to pull the drop down, but also the magnetic force experienced by the paramagnetic solution. By using the experiments performed as described in the previous subsection with no magnet near the drop, and comparing these results with the setup including the magnet, the deformation of the drop due to the magnetic force can be assessed, and from there the magnetic susceptibility of the drop is calculated. In figure 5.4 an example is shown of a drop of constant volume, which is elongated as the magnet is brought closer to the droplet.

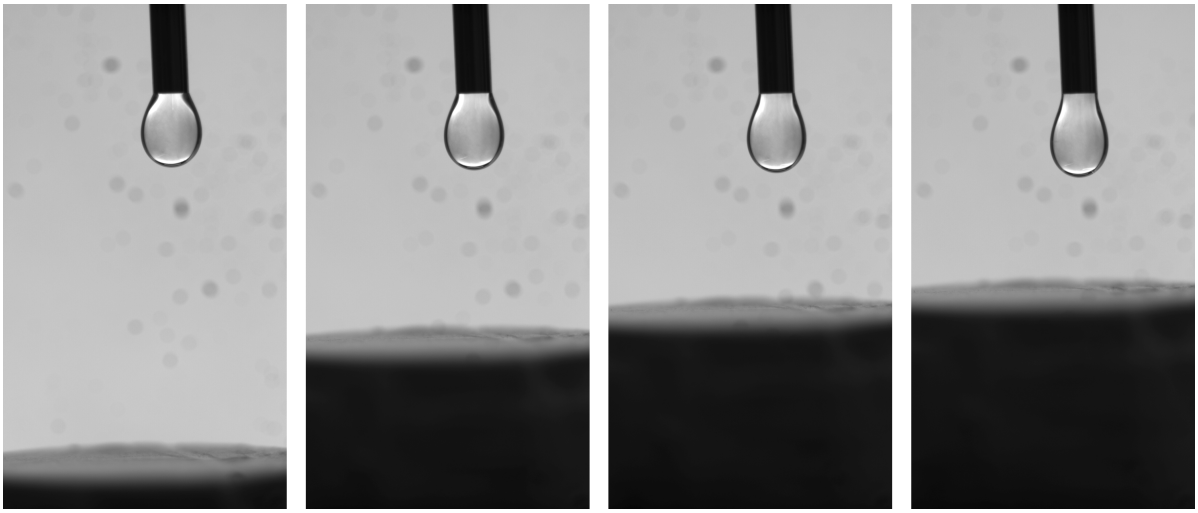

Figure 5.4: Deformations of a droplet of sample C-100 at constant volume $V = 18.50\,\mathrm{mm}^3$, due to the proximity of the magnet.

The force of gravity acting on the drop can be calculated as follows: $F_g = \rho_m g V_d$. For the given volume, the Bond number Bo can be found from the pendant drop experiments without magnet. When the experiment is repeated with the magnet below, a different Bond number is obtained, which will be referred to as the magnetic Bond number, $\mathrm{Bo}_{\mathrm{mag}}$. By analyzing the difference between both Bond numbers, the ratio of the magnetic force compared to the force of gravity can be calculated.

$$\mathrm{Bo} = \frac{F_g}{F_{\mathrm{IFT}}} \tag{5.4a}$$

$$\mathrm{Bo}_{\mathrm{mag}} = \frac{F_g + F_{\mathrm{mag}}}{F_{\mathrm{IFT}}} \tag{5.4b}$$

$$\frac{\mathrm{Bo}_{\mathrm{mag}} - \mathrm{Bo}}{\mathrm{Bo}} = \frac{F_{\mathrm{mag}}}{F_g} \tag{5.4c}$$

Since the force of gravity can be calculated from the density and volume of the drop, the magnetic force as a fraction of the force of gravity can be calculated from the above relations. The equation for the magnetic force in the direction of the gravity is the following:

$$F_{\mathrm{mag,z}} = \frac{\chi_m}{\mu_0} V B_z \frac{\partial B_z}{\partial z} \tag{5.5}$$

In the above equations, the magnetic force is described as a body force, which scales with the gradient magnetic field intensity $B_z \frac{\partial B_z}{\partial z}$. Since this intensity is not uniform in space, the force that the magnet exerts on the drop varies depending on the location within the drop. Especially when the magnet is very close to the drop, the gradient in the magnetic field intensity within the drop is relatively large, and the difference in magnetic pull on the drop might be significant. Further from the magnet, the gradient magnetic field intensity becomes more constant. The intensity as a function of the distance from the magnet's surface is derived from the one-dimensional Matlab calculation of $B_z \frac{\partial B_z}{\partial z}$ of the array of magnets, as displayed in figure 5.5a.

For simplicity of calculation, the value of the gradient magnetic field intensity is initially assumed to be constant in the entire volume of the drop. To assess whether this assumption is valid, the full range in magnetic field intensity over the height of the drop is evaluated to see whether the difference in magnetic field intensity between the top and bottom of the drop differs significantly. The magnetic susceptibility of the drop is thus calculated by taking the gradient magnetic field intensity at the height of the needle (d_{needle}), at the apex of the drop (d_{apex}), and at the widest part of the drop (d_{drop}), as illustrated in figure 5.5b.

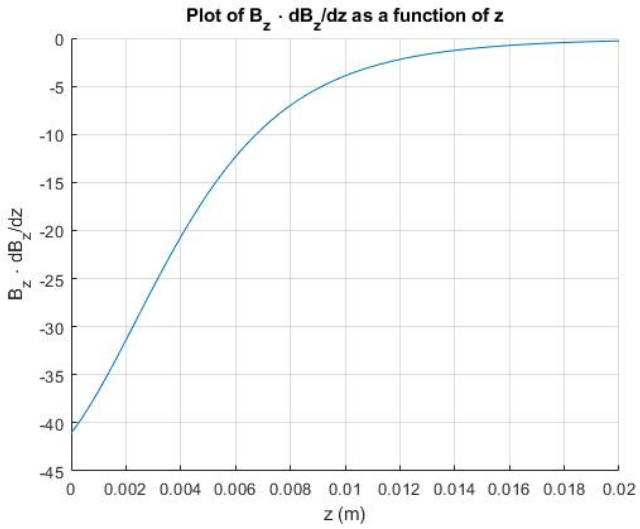

(a) Gradient magnetic field intensity $B_z \frac{\partial B_z}{\partial z}$ as a function of the distance from the magnet.

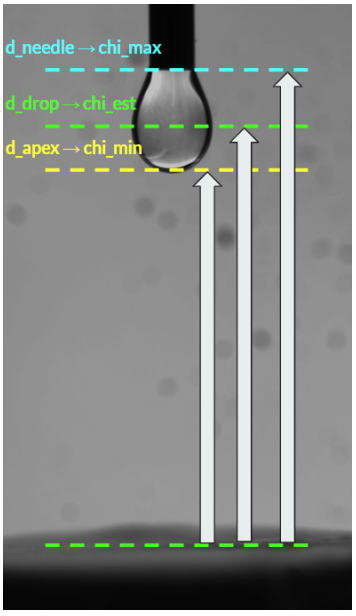

(b) Heights d_{needle}, d_{drop} and d_{apex}, at which the gradient magnetic field intensity is taken for magnetic susceptibility calculations.

Figure 5.5: Reading the gradient magnetic field intensity from the distance between the droplet and magnet.

5.2.1. Measured magnetic susceptibilities of the samples

First, the Bond numbers in absence of the magnet for an increasing drop volume were plotted for all concentrations, and are displayed in figure 5.6a. In the figures the dots represent the individual measurements, and the line is a second-order polynomial fit of the datapoints. As the concentration $MnCl_2$ increases, the graph moves up, which follows logically from the definition of the Bond number $\text{Bo} = \frac{\rho g R_0^2}{\gamma}$, given the relatively larger increase in density, as compared to the increase of the IFT that were previously measured for all samples.

The pendant drop experiments were repeated with magnets placed at a fixed distance d_{needle} from the magnet. The results of the Bond number as a function of the drop volume for all samples are displayed in figures 5.6b to 5.6f. The experiments are repeated for different distances between magnet and needle tip d_{needle}, which are displayed in different colors.

As the magnet is positioned closer to the pendant drop, the graph of the Bond number is translated upwards, compared to the pendant drops without magnet in the setup. This follows logically from the fact that the Bond number with the magnet does not only represent the ratio between gravity and surface tension, but the magnetic force is added, as explained in equation 5.4b. Most graphs show similar trends, except for the C-40 sample, for which the pink graph is not only translated as the magnet moves closer, but the slope of the graph actually seems to be increased significantly. Since this graph is deviant, it is expected this measurement is unreliable, and the results following from that measurement will not be processed.

By rewriting equation 5.5, the magnetic susceptibility can be derived. The magnetic susceptibility was eventually calculated through the following relations, for the gradient magnetic field intensity taken at a distance of d_{needle}, d_{apex}, and d_{drop}:

$$F_g = \rho V_d g \tag{5.6a}$$

$$F_{\text{mag}} = \frac{(\text{Bo}_{\text{mag}} - \text{Bo})}{\text{Bo}} F_g \tag{5.6b}$$

$$\chi = \frac{F_{\text{mag}} \mu_0}{V B_z \frac{\partial B_z}{\partial z}} \tag{5.6c}$$

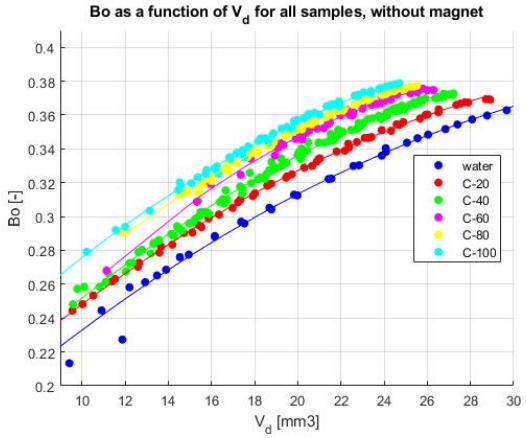

(a) Pendant drop measurements without magnet, for water and all $MnCl_2$ samples

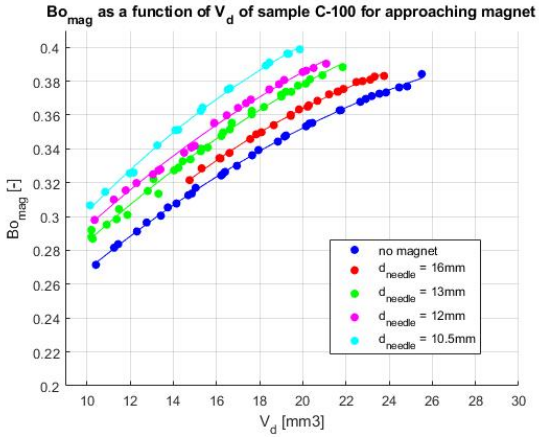

(b) C-100 sample magnetic pendant drop measurements for approaching magnet.

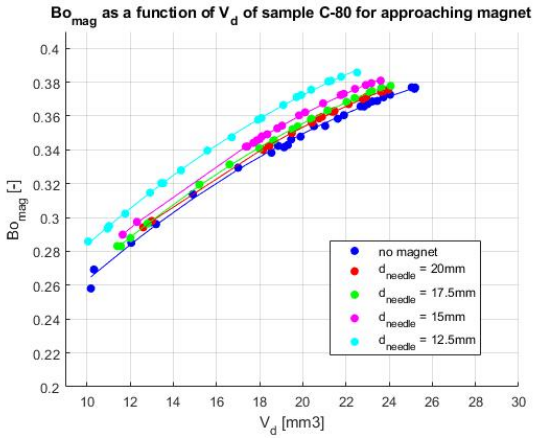

(c) C-80 sample magnetic pendant drop measurements for approaching magnet.

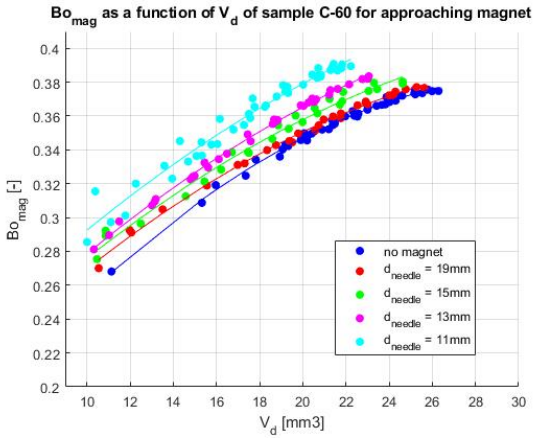

(d) C-60 sample magnetic pendant drop measurements for approaching magnet.

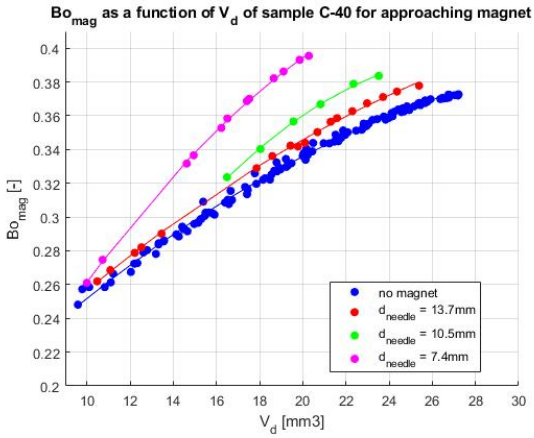

(e) C-40 sample magnetic pendant drop measurements for approaching magnet.

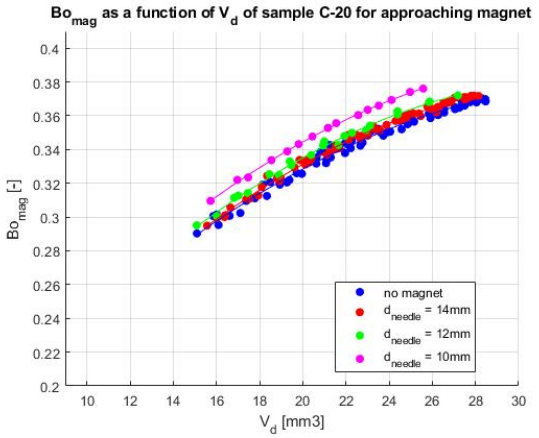

(f) C-20 sample magnetic pendant drop measurements for approaching magnet.

Figure 5.6: Graphs of (magnetic) Bond number as a function of drop volume, for different samples, without magnet, and for approaching magnet.

Since the Bond number is more accurate for larger drop sizes, only images of drops of at least 80% of the maximum achievable drop volume were evaluated. Not the Bond numbers obtained from individual measurements are used, but the Bond number and magnetic Bond number as calculated by the fit of the graphs at the given concentration. However, the individual images were inspected to determine the distance between magnet and needle, apex and drop center.

Further, since the magnetic field intensity in the drop further from the magnet has a smaller gradient than close to the magnet, these measurements are expected to give a more precise range of the actual magnetic susceptibility. For the sample C-100 the following results for the magnetic susceptibility were calculated:

V_{drop}	Bond number [$-$]		Force [mN]		Magnet distance [mm]			Mag. Susc. $\chi/10^{-4}$		
[mm^3]	Bo_{mag}	Bo	F_g	F_{mag}	d_{needle}	d_{apex}	d_{drop}	χ_{max}	χ_{min}	χ_{est}
19.28	0.3962	0.3476	0.287	0.040	10.67	6.75	8.35	8.12	2.62	4.14
20.00	0.3854	0.3523	0.298	0.028	12.18	8.29	9.86	8.37	2.73	4.31
19.01	0.3708	0.3458	0.283	0.021	13.08	9.39	10.96	8.46	2.90	4.56
21.64	0.3738	0.3623	0.323	0.010	16.29	12.35	14.03	8.47	2.96	4.69

Table 5.1: Calculation magnetic susceptibility for sample C-100.

From the obtained values for χ, it can be seen that most results indicate approximately the same value. Further, the range between χ_{min} and χ_{max} is not significantly influenced by the distance to the magnet. The average (μ) and standard deviation (σ) of the magnetic susceptibilities ($\chi_{\max}$, χ_{est}, $\chi_{\min}$) that were calculated for all samples are displayed in table 5.2. For each sample, $n = 4$ individual measurements were considered. For these limited datasets, the standard deviation of most samples is relatively small, except for sample C-40 and C-60.

Finally, the average magnetic susceptibilities and their corresponding standard deviations were plotted as a function of the Mn molarity in figure 5.7. A linear relation between both quantities is expected, which corresponds approximately with the trends of the graphs. The values of χ_{est} are assumed to best represent the actual magnetic susceptibility of the magnetic fluid.

Sample	Molarity Mn	$\chi_{\max}/10^{-4}$		$\chi_{\mathrm{est}}/10^{-4}$		$\chi_{\min}/10^{-4}$	
		μ	σ	μ	σ	μ	σ
C-20	1.16	1.2	0.30	0.60	0.15	0.36	0.09
C-40	2.33	3.1	1.16	1.6	0.60	0.89	0.32
C-60	3.48	5.8	1.22	3.3	0.66	2.1	0.44
C-80	4.71	7.4	0.30	4.2	0.34	2.7	0.27
C-100	5.70	8.4	0.16	4.4	0.25	2.8	0.16

Table 5.2: Resulting minimum, maximum and estimated magnetic susceptibilities of each sample.

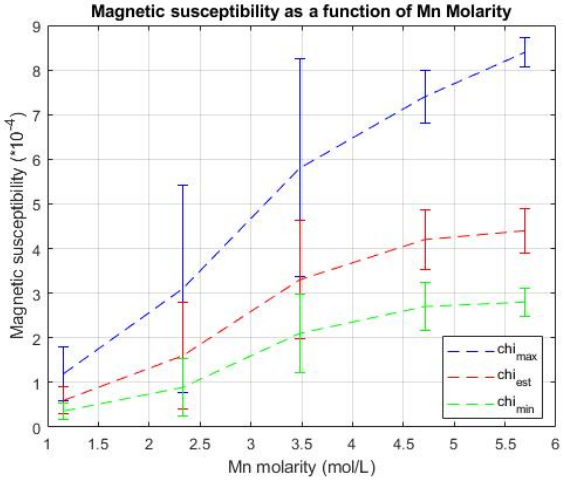

Figure 5.7: Results for the experimentally determined magnetic susceptibility of the $MnCl_2$ solutions of different concentrations. The error bars indicate $\mu \pm 2\sigma$.

5.2.2. Accuracy of the magnetic pendant drop measurements

The results obtained in the previous section can be compared to the values reported for the magnetic susceptibility in literature. Figure 5.8 shows how the experimentally obtained properties compare to the values from literature. The experimentally obtained value for the magnetic susceptibility lies well within the reported values from literature, closest to those reported by Miura [51]. Therefore, it is concluded that the magnetic pendant drop experiments are successful in getting the right order of magnitude of the magnetic susceptibility.

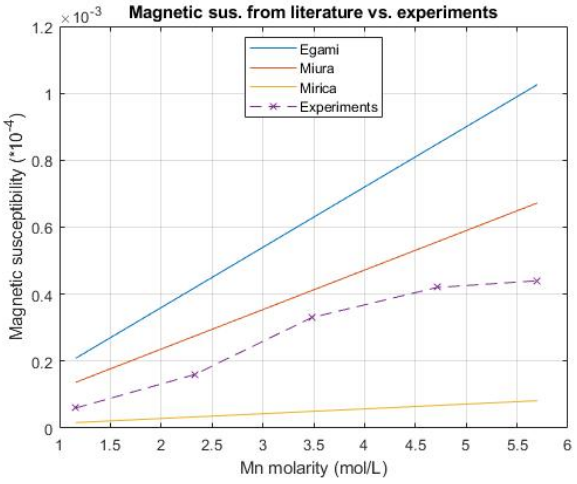

Figure 5.8: Comparison magnetic susceptibility as reported in literature and experimentally found.

At the beginning of this chapter, the following research question was stated:

> SQ4: What method can be developed to measure the magnetic susceptibility of the solution, do the measured magnetic susceptibilities agree well with the values reported in literature, and what magnetic susceptibility of the solutions can be achieved?

An adjusted version of the pendant drop method was developed to measure the magnetic susceptibility of liquids. The magnetic susceptibilities of the samples measured lie within the range of the values reported in literature, and are especially close to the values reported by Miura [51]. The magnetic susceptibility measured for the sample at saturation concentration was $\chi_m = 4.4 \cdot 10^{-4}$.

6

Estimation of the apparent density & validation using Magnetic Levitation

In this chapter the findings of the gradient magnetic field intensity $(\vec{B} \cdot \vec{\nabla})\vec{B}$ from chapter 2, the measured solution density ρ_m from chapter 4, and the measured magnetic susceptibility χ_m from chapter 5, are combined to calculate the apparent density ρ_s that can be achieved in the $MnCl_2$ solution samples.

$$\rho_s = \rho_m + \frac{\chi_m - \chi_s}{g\mu_0}(\vec{B} \cdot \vec{\nabla})\vec{B}$$

These calculations indicate whether MagLev of AAM can be achieved in each sample. To confirm these findings, MagLev experiments were conducted, not only with AAM and CAM, but also with chloroform: a high-density liquid that is immiscible in water. From these experiments the equilibrium height of the suspended materials can be measured, after which the magnetic susceptibility can be calculated again, and be compared to the values obtained from the magnetic pendant drop experiments. From this it can also be concluded whether the magnetic susceptibility of the suspended AAM χ_s has a significant effect on the levitation height, or that the magnetic susceptibility of the AAM is negligible, as initially assumed.

Further, at the end of this chapter, the following research questions will be answered:

SQ5: What apparent densities can be achieved in a static MagLev setup, and can levitation of graphite be achieved?

SQ6: Will the graphite particles themselves be attracted or repelled by the magnetic field significantly, overshadowing the effect of magnetic buoyancy?

SQ7: What opportunities and limitations have been identified for scaling the method into a continuous process?

6.1. Estimated apparent density from experimentally determined properties

In chapter 4 and 5 the density and magnetic susceptibility of the magnetic $MnCl_2$ samples were determined experimentally. A summary of the properties is given in table 6.1. The densities were very similar to those reported in literature by Rard and Miller [63] and by Herrington [26]. The values obtained for the magnetic susceptibilities, fall within the range as reported by Mirica [50], Miura [51] and Egami [15].

Sample	Density ρ [g cL^{-3}]	Magnetic susceptibility $\chi/10^{-4}$
C-20	1.11236	0.60 ± 0.30
C-40	1.22023	1.6 ± 1.20
C-60	1.33973	3.3 ± 1.32
C-80	1.45922	4.2 ± 0.68
C-100	1.54096	4.4 ± 0.50

Table 6.1: Summary of magnetic fluid properties experimentally determined.

These properties can be used to solve the equation for the apparent density in the magnetic liquid as a function of the gradient magnetic field intensity:

$$\rho_s = \rho_m + \frac{\chi_m - \chi_s}{g\mu_0}(\vec{B} \cdot \vec{\nabla})\vec{B}$$

By solving the equation for the measured properties of all samples, the following apparent densities are expected to be achievable within the magnetic solution near a single cylindrical magnet, as illustrated in figure 6.1. The horizontal line indicates the density of graphite.

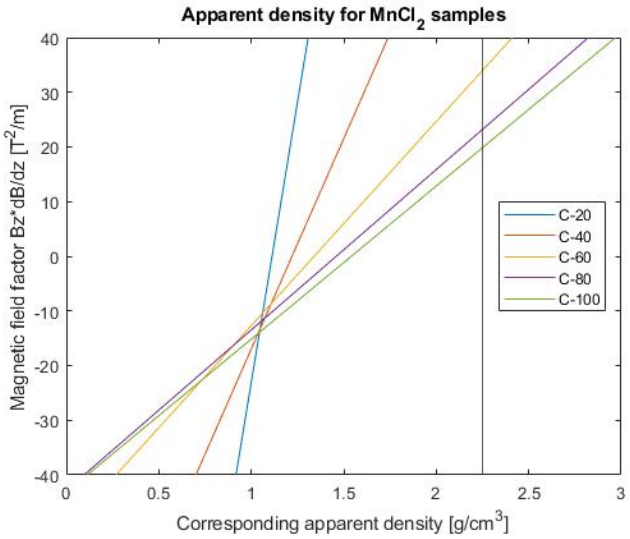

Figure 6.1: Achievable apparent density in the $MnCl_2$ solution samples.

Thus, from this graph it seems that levitation of anodic graphite should most likely be possible in samples C-100 and C-80, and probably just at a very short equilibrium height for sample C-60.

6.2. MagLev setup

For the MagLev experiments, two setups were used, and three materials were attempted to be levitated in the samples. The first setup that was built, consisted of microscope slides, glued together at a distance of the thickness of one microscope slide apart. Such a very thin beaker is referred to as a 'Hele-Shaw Cell', in which flows in 2D can be observed. These cells were placed in a holder on top of the array of magnets. Secondly, small glass vials were filled with the samples and placed on top of a magnet. Both setups are shown in figure 6.2.

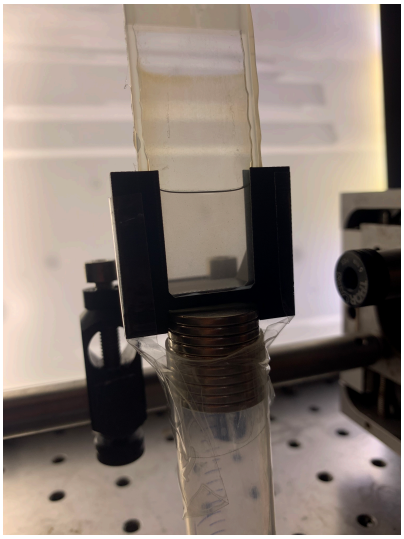

(a) Hele Shaw Cell filled with $MnCl_2$ sample.

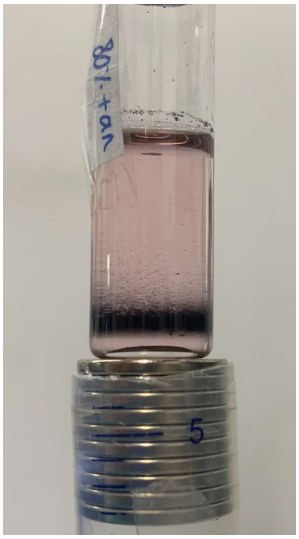

(b) Glass vial filled with $MnCl_2$ sample.

Figure 6.2: MagLev setup.

To achieve a calibration of the equilibrium heights corresponding to the various apparent densities, materials of different densities were suspended in the samples: drops of chloroform ($\rho = 1.48\mathrm{g\,cm^{-3}}$), AAM and CAM. In the Hele-Shaw Cell setup, anode material dropped to the bottom for all samples. Since these results were different than for the vials, it was assumed these experiments were influenced by wall effects. Because of this, it was decided to continue with the setup with the vials. For this setup levitation of materials was possible. MagLev of chloroform droplets in the C-40, C-60 and C-80 samples is shown in figure 6.3, and MagLev of anodic graphite is shown in figure 6.4.

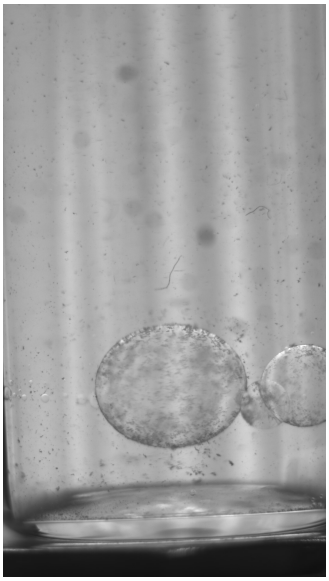

(a) Chloroform droplet in C-40 sample.

(b) Chloroform droplet in C-60 sample.

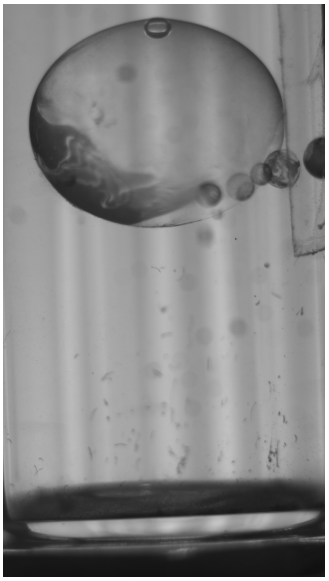

(c) Chloroform droplet in C-80 sample.

Figure 6.3: MagLev of chloroform droplet in $MnCl_2$ solution samples.

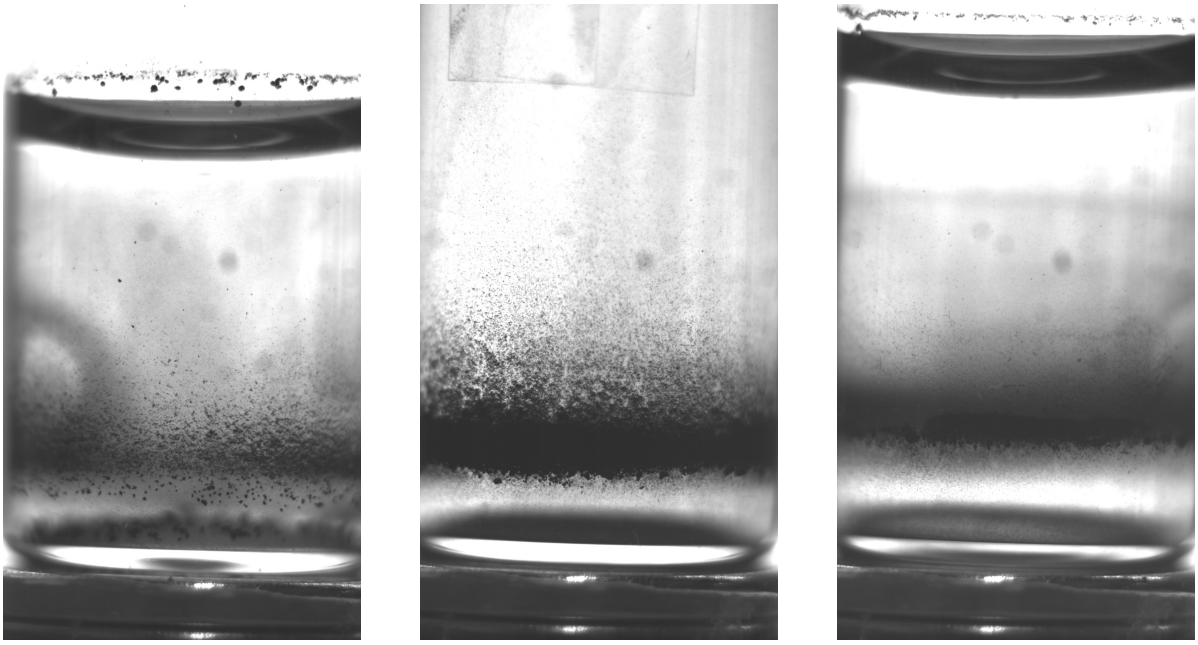

(a) Anodic graphite in C-60 sample. **(b)** Anodic graphite in C-80 sample. **(c)** Anodic graphite in C-100 sample.

Figure 6.4: MagLev of anodic graphite in $MnCl_2$ solution samples.

In table 6.2 below, the heights at which the materials were levitated are summarized for all samples.

Sample	Levitation height [mm]		
	Chloroform	Anode	Cathode
C-20	sinks	sinks	sinks
C-40	7	sinks	sinks
C-60	10	3, or sinks	sinks
C-80	18*	5	sinks
C-100	floats**	6	sinks

Table 6.2: Equilibrium height at which the suspended materials levitate above the magnet.
* Some of the chloroform floats, due to very similar density of chloroform and C-80 sample.
** After some time, a large amount of the $MnCl_2$ crystallizes from the solution (salting out effect).

As expected from the sample properties, MagLev of anodic graphite is possible in samples C-60 (partially), C-80 and C-100, and MagLev of CAM is impossible in all samples.

By rewriting the apparent density equation, the magnetic susceptibility could also be estimated from these results, assuming $\rho_{\mathrm{chloroform}} = 1.48\mathrm{g\,cm^{-3}}$ and $\rho_{\mathrm{anode}} = 2.25\mathrm{g\,cm^{-3}}$:

$$(\chi_m - \chi_s) = \frac{(\rho_s - \rho_m)}{B_z \frac{\partial B_z}{\partial z}} g\mu_0 \tag{6.1}$$

By filling in this equation for the levitated materials, the following values for the magnetic susceptibilities are estimated, as displayed in table 6.3. It is difficult to draw conclusions from these calculations, since the exact densities of the chloroform and the AAM are uncertain. However, the new magnetic susceptibilities compared to those found in the previous two chapters are plotted in figure 6.5.

The magnetic susceptibilities are slightly higher than calculated using the magnetic pendant drop method. This could indicate that the graphite itself has a small, negative magnetic susceptibility (χ_s). However, both measurement techniques are associated with significant error margin, and no interaction between dry powder of graphite and the magnet was observed. Further, the values stated in literature indicate that the magnetic susceptibility is very small. Thus, it is assumed the value of χ_s will be negligible.

Experiment	$(\rho_s - \rho_m)$ [$\mathrm{kg\,m^{-3}}$]	h [mm]	$B_z \frac{\partial B_z}{\partial z}$ [$\mathrm{T^2\,m^{-1}}$]	$(\chi_m - \chi_s)$ [–]
Chloroform in C-40	260	7	9.374	$3.436 \cdot 10^{-4}$
Chloroform in C-60	140	10	3.920	$4.403 \cdot 10^{-4}$
Chloroform in C-80	21	18	0.4593	$5.636 \cdot 10^{-4}$
Anode in C-60	910	3	25.883	$4.334 \cdot 10^{-4}$
Anode in C-80	791	5	16.117	$6.050 \cdot 10^{-4}$
Anode in C-100	709	6	12.336	$7.085 \cdot 10^{-4}$

Table 6.3: Levitation heights and magnetic susceptibility estimated from MagLev experiments.

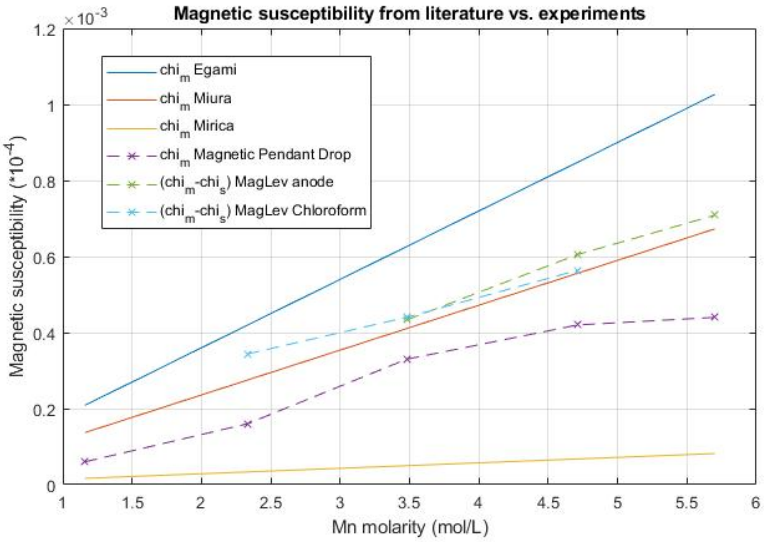

Figure 6.5: Magnetic susceptibilities as calculated from the MagLev experiments.

The levitation heights that were measured from the magnet surface, were rounded to the nearest mm. Especially for levitation heights close to the magnet, a small measurement inaccuracy is associated with a relatively large difference in the gradient magnetic field intensity: at $7\,\mathrm{mm}$, the intensity is approximately $9.3\,\mathrm{T^2\,m^{-1}}$, while at $8\,\mathrm{mm}$ the intensity is only $7.0\,\mathrm{T^2\,m^{-1}}$: a difference of 33%. Thus, there might exist a significant uncertainty in the magnetic susceptibilities calculated for the samples at low levitation height.

Nonetheless, the values calculated from the chloroform and anodic graphite levitation experiments are very similar to one another, and lie very close to the values reported by Miura [51]: on average 8% higher. So for these measurements, there is no reason to assume significant uncertainties in the magnetic susceptibilities calculated from the MagLev experiments. The values resulting from the MagLev experiments are on average 53% higher than the values measured using the magnetic pendant drop method.

6.3. Conclusion apparent density through MagLev experiments

The results from the MagLev experiments align very well with the expected outcomes from the previous chapter. Now, the final subquestions of the research question can be addressed:

> SQ4: What apparent densities can be achieved in a static MagLev setup, and can levitation of graphite be achieved?

For samples C-60, C-80 and C-100 levitation of anodic graphite can be achieved in the solution. The levitation height is very close to the magnet: at most $6\,\mathrm{mm}$. Since it is desirable to have the material levitate as far from the magnet as possible, the maximum density that can be achieved is approximately

that of graphite: $\rho = 2250 \mathrm{kg\,m^{-3}}$.

SQ5: Will the graphite particles themselves be attracted or repelled by the magnetic field significantly, overshadowing the effect of magnetic buoyancy?

No significant interaction of anodic graphite with the magnet is observed. However, the graph of ($\chi_m - \chi_s$) from MagLev of anode material in the samples does lie slightly higher than the graph of χ_m as obtained from the magnetic pendant drop method. Since both experiments contain some uncertainties, no conclusions can be drawn on the exact magnetic susceptibility of graphite, but it is assumed to be negligible.

SQ6: What opportunities and limitations have been identified for scaling the method into a continuous process?

While static MagLev for the separation between anode and cathode on small scale might show some promising results, the following challenges have been identified for scaling the experiments into a large-scale, continuous setup:

- Small particles settle very slowly to their equilibrium height, as the terminal velocity following from Stokes' Law depends on the particle size to the power two:

$$v = \frac{2}{9} \frac{(\rho_s - \rho_m)}{\mu} g R^2 \tag{6.2}$$

  In this equation, μ is the dynamic viscosity of the fluid and R is the radius of the (spherical) particle;
- Generating a magnetic field, which is uniform in height is very challenging;
- The height at which the anode material levitates is very close to the bottom, where the cathode lies, thus collecting them separately might be challenging;
- Aggregates of mixed anode and cathode particles could form, which need to be liberated;
- The flow should move very slowly, to maintain the laminar regime, such that the particles will not mix;
- The cathode material sinks, and should thus be collected from the bottom;
- Subsequent collection and cleaning from the BM might be very costly;
- On a large scale, a lot of $MnCl_2$ waste will be produced, which needs to be handled and disposed of carefully.

7

Conclusion

In this chapter an overview of the findings from this thesis research are presented, as well as the most relevant contributions from the research. Finally, the limitations of the research are stated, and recommendations for future work are given.

7.1. Summary and conclusions

The goal of this research was to investigate whether Magnetic Levitation (MagLev) of battery materials could be achieved. In order to have anodic graphite levitate, a high apparent density inside a paramagnetic solution needs to be generated. To achieve a high apparent density, several factors play a role: the gradient magnetic field that can be generated, the density of the paramagnetic medium, and the magnetic susceptibility of the paramagnetic medium. These factors were individually investigated.

For the generation of the gradient magnetic field, permanent NdFeB magnets were purchased, as these have the advantage that they do not require input of energy to generate the magnetic field. Simulations were performed using COMSOL Multiphysics and discussed in chapter 2, to find out which configuration was most suitable for the purpose of this research. The optimal choice for a small-scale, static MagLev setup was an array of disc magnets. The gradient magnetic field intensity that could be achieved using this simple magnetic configuration, was$(\overrightarrow{B} \cdot \overrightarrow{\nabla})\overrightarrow{B} = 41\mathrm{T}^2\,\mathrm{m}^{-1}$. The density of the solution was measured with a densitymeter and was approximately $\rho_m = 1.54\mathrm{g}\,\mathrm{cm}^{-3}$ at saturation concentration.

It was found from literature [15, 50, 51] that the magnetic susceptibility is a property which is very difficult to measure. In order overcome this, a new measurement technique was developed, which was described in chapter 5: the magnetic pendant drop method. Similar to the conventional pendant drop method, it analyzes the shape of the surface of a pendant drop to determine the ratio between the forces working on the droplet. In the conventional pendant drop method, the ratio between surface tension and gravity working on the droplet is determined. In the magnetic pendant drop method, a magnet is added to the setup below the drop, due to which an additional vertical force acts on the drop. The magnetic susceptibilities obtained through this method were very close to the values reported in literature, as can be seen in figure 5.8.

Finally, MagLev experiments were conducted to validate the measured magnetic susceptibilities and confirm whether levitation could indeed be achieved. The anodic graphite could be levitated at $6\,\mathrm{mm}$ above the magnet, as shown in figure 6.4c. The magnetic susceptibilities that were calculated from this method were again close to the values reported in literature and measured with the magnetic pendant drop method. After this, the research question could be addressed, which was formulated in section 1.3.

Research question

Can a sufficiently high apparent density be obtained by static MagLev for the levitation of graphite, indicating MDS to be a promising separation method for the separation between AAM and CAM?

The research question can be answered as follows: it was found that anodic graphite could be levitated up to 6 above the magnet in a small-scale static MagLev setup containing a high concentration $MnCl_2$ solution, as shown in figure 6.4. Cathode materials would sediment to the bottom in the MagLev setup. The movement of the particles to their equilibrium height initially occurred quite rapidly. However, once the materials had been submerged for some time, the particles moved to their equilibrium height less rapidly, especially the smaller particles. It remains uncertain why this change occurs, but it is assumed it might be because the porous graphite particles absorb some of the magnetic solution.

To ensure a larger difference in equilibrium height between anode and cathode material, a solution of higher magnetic susceptibility should be used, or a stronger gradient magnetic field should be generated. The $MnCl_2$ solutions in this research were already prepared at approximately the saturation concentration, so no $MnCl_2$ solution of higher magnetic susceptibility could be prepared, and another magnetic fluid would have to be used to enhance the magnetic susceptibility.

$GdCl_3$ and $DyCl_3$ are alternative magnetic salts that can be used to prepare paramagnetic solutions. The molar magnetic susceptibility of $GdCl_3$ is approximately twice as large as that of $MnCl_2$, and that of Dy in several compositions is reported to be up to six times the molar magnetic susceptibility of $MnCl_2$. However, the solubility of these salts in water and their corresponding densities were unknown. If the same concentration could be achieved as for $MnCl_2$ and the density will also be comparable, a magnetic force of up to six times higher could be generated within the solution, and particles of densities of $4.5\,\mathrm{g\,cm^{-3}}$ could be levitated at $5\,\mathrm{mm}$ above the magnet. On the downside, the cost of these salts are much higher than that of $MnCl_2$.

In addition to increasing the magnetic susceptibility of the solution, the density might also be increased. This was for instance attempted by Mirica [50] by adding sucrose or $NaCl_2$ to the solution. However, when the solution is already (almost) saturated, it is expected that not much of the added solute will still dissolve.

Further, the gradient magnetic field that was generated in the experiments could not be increased much further. Using a different configuration of permanent magnets can only induce a slightly a slightly higher magnetic flux density. So, this will only result in a slightly larger magnetic force. On the other hand, by applying electromagnets or superconducting magnets, a much stronger magnetic field can be generated. For instance, Miura et al. [51] were able to levitate precious metals of densities above $\rho = 20\,\mathrm{g\,cm^{-3}}$ using superconducting magnets. These magnets do require a high energy consumption to maintain the field, resulting in higher operating cost.

Due to these limitations, scaling the static MagLev setup into a continuous MDS separation method between anode and cathode materials will be very challenging. However, these challenges have also been encountered in continuous MDS of other materials, such as plastics. This separation method has been extensively researched and optimized, indicating there is also room for improvement in MDS for the separation of BM. A suggestion for a continuous setup is shown in figure 7.1. To facilitate the movement of the (graphite) particles to the right, a very slow flow from left to right is required, as well as a small inclination of the magnets, due to which the graphite particles experience a small force to the right. The magnets do not form a continuous surface, but contain gaps within or between the magnets, through which the cathode particles will fall. Thus, the anode particles can be collected above the magnets, while the cathode particles aer collected below.

The selectivity of the separation method relies on many factors, but it is assumed a relative high purity can be obtained through MDS, because of the large difference in densities between the anode and cathode. Since there is an urgent need to improve the recovery of battery materials from battery waste, it is definitely relevant to perform further research into the selectivity of the method. Even if the selectivity of the method itself is limited, it could most likely be a useful step in a chain of separation steps, since the purity requirements of battery materials are very high. First, some separation method of low selectivity

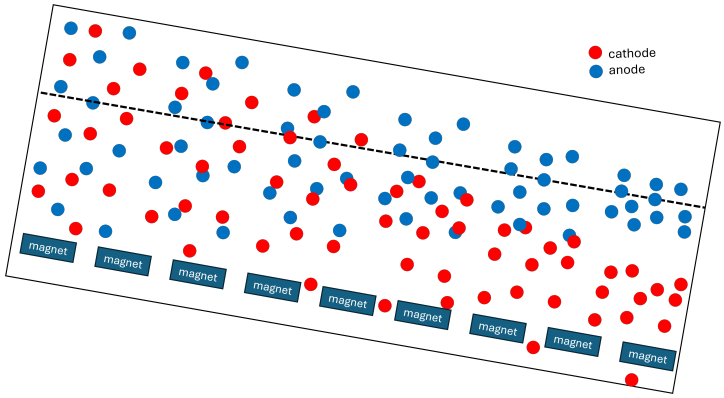

Figure 7.1: Option for design of a flow chamber for a continuous MDS process, with gaps between/inside the magnets. The anode material (blue) is collected above the magnets, while the cathode material (red) falls through the magnets.

could be performed, such as froth flotation (FF) or a dry method. Next, MDS could be performed to improve the purity of the graphite and realize benification of the cathode material from the BM, such that not all BM material should be subjected to the metallurgic separation, saving cost and waste production.

Moreover, some novel materials are being explored to be used as electrodes. For instance, the Dutch company E-Magy is developing nano-porous silicon anodes. While silicon's intrinsic density is approximately $\rho = 2.33\,\mathrm{g\,cm^{-3}}$ and thus slightly higher than that of graphite, the porous structure of the silicon might reduce the bulk density of the electrode material significantly, allowing for a larger distance in levitation height between anode and cathode, and therefore a more selective separation. The reported void fraction is $35\%_{\mathrm{vol.}}$ [48], resulting in a bulk density of $\rho \approx 1.5\,\mathrm{g\,cm^{-3}}$. Since this is significantly lower than the density of graphite, these particles could be more easily levitated at much higher equilibrium height than graphite. Thus, nanoporous silicon might be much simpler to separate from cathode materials through MDS than graphite.

In conclusion, the method shows promise on the lab-scale, but will require careful design considerations in a continuous process, and possibly a different choice of magnets and paramagnetic medium. Although application on current anode and cathode materials might be challenging, better separation efficiency could be obtained for possible future electrode materials. More generally, the method can be applied for separation between micron-scale particles with a significant difference in density, of which at least one should have a density below that of graphite.

Finally, several difficulties were encountered during the research. These issues might have led to some uncertainties in the results, and should therefore be noted:

- The $MnCl_2$ concentration was difficult to determine exactly, due to issues with solubility and unknown water content in the $MnCl_2$ beads;
- There is a large range of values of magnetic susceptibility of $MnCl_2$ reported in the literature, so the outcomes of the magnetic susceptibility experiments could not be validated according to the literature;
- The results of the magnetic susceptibilities of the samples are not proportional to the manganese concentration from the ICP-OES measurements;
- Some issues were encountered during the pendant drop experiments, which were difficult to identify, for instance: the drop could slowly adhere to the outside of the needle, during the measurements. This was only discovered upon processing of the measurements, which might have led to some unreliable measurements;
- The exact density and magnetic susceptibility of graphite and chloroform are not known, so only estimations of the magnetic susceptibility could be derived from the MagLev experiments;
- The magnetic field in the experiments was assumed to be one dimensional and uniform in height, while in reality the field has a gradient and propagates in three dimensions, which likely causes a small uncertainty in the results.

7.2. Contributions

The most relevant contributions that have been developed and discovered in this research, are the following:

Magnetic Pendant Drop Method

The magnetic pendant drop method was developed to study the magnetic susceptibility of paramagnetic solutions, as described in chapter 5. By comparing the shape of the drop of a magnetic liquid with and without a magnet underneath it and the corresponding Bond number, the magnetic susceptibility of the liquid could be determined quite accurately. The method was performed under the assumption that the magnetic force on the drop was a uniform body force, defined based on the gradient magnetic field intensity at the widest part of the droplet, while in reality a gradient in the intensity exists within the droplet. By implementing this non-uniformity in the calculation, the method could be further improved.

MagLev of micro-scale particles (anodic graphite)

All research into MagLev reported in the literature has only applied it on mm_3 scale droplets of immiscible liquids, or solid materials of mm scale or larger. In this research it was confirmed that MagLev can also be applied to solid materials of micron-scale. Logically, the settling time of these smaller particles to reach their equilibrium height is exponentially longer.

However, the resultant force that works on the suspended particles scales with the distance to their equilibrium height. Thus, the initial velocity of particles that are far from their equilibrium height is relatively large, and will thus rapidly move close to their equilibrium height. If the densities of both materials are far enough apart, they are not required to settle fully to their respective equilibrium heights, but they will be separated sufficiently before reaching their equilibrium height. This fact is illustrated in figure 7.2 below.

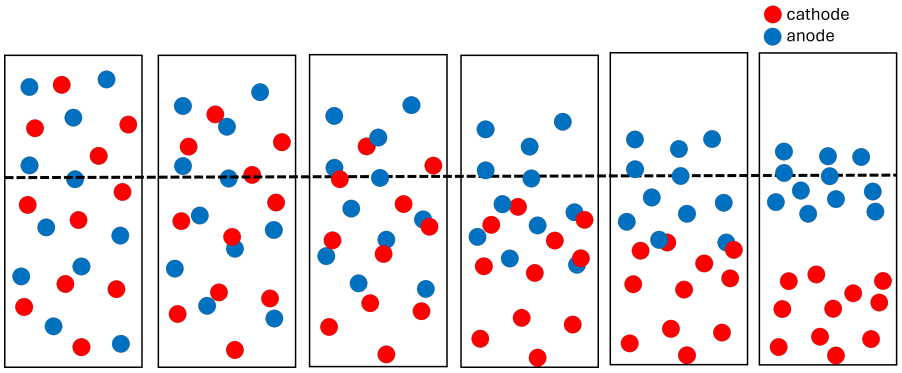

Figure 7.2: Settling of anode (blue) and cathode (red) particles over time to their respective equilibrium height: the dashed line and the bottom. Particles that are far from their equilibrium height experience a larger force, and will therefore move at higher velocity. Before the particles reach their equilibrium height, they can already be fully separated. In this image it is assumed the particles are well liberated.

Magnetic field configurations and their limitations of permanent magnets.

By performing simulations of magnetic field intensities for many different configurations of permanent magnets, it was found that a very limited gradient magnetic field intensity can be achieved for any configuration. The maximum field intensity that can be obtained is limited by the 'grade' of the magnet. This material property can only be increased to reach a magnetic remanence of $B_r = 1.42\,\mathrm{T}$.

By studying several configurations, an overview is given showing the trade-off between the gradient magnetic field intensity and the depth to which the gradient magnetic field intensity is significant, as displayed in table 2.1. For the small-scale, static MagLev setup, a single cylindrical magnet was selected as best option. For a continuous setup, the gradient magnetic field should be as uniform as possible at a given height above the magnet(s), which turned out to be difficult to achieve in practice.

7.3. Recommendations for future work

In this section, improvements of different aspects of this research are proposed, and suggestions are made for other separation methods, which could be applied for the separation of BM materials.

Improvements for the Magnetic Pendant Drop analysis

Firstly, the analysis of the magnetic pendant drop method could be improved, by implementing the fact that the magnetic field within the drop is not uniform in height, but that there exists a gradient in the magnetic field within the drop. This could for instance be implemented in the opendrop software of Berry [9], by having the Bond number vary as a function of z, corresponding to the gradient magnetic field intensity at the given height.

In reality the gradient magnetic field is not only non-uniform in height, but also not unidirectional. In order to be completely precise, the components perpendicular to the gravity should also be taken into account, but this will once again add to the complexity of the analytic solver. Finally, the results of the method cannot accurately be validated, as there exists large disagreement on the value of the magnetic susceptibilities that are reported for most materials.

Magnetic sessile drop experiments

Instead of studying the deformation of a pendant drop under the influence of a magnetic field, a sessile drop under the influence of a magnetic field could also be investigated. This optical method was initially proposed because the volume can be controlled more precisely, than that of a drop suspended from a syringe. This method has been previously investigated by Basaran and Wohlhuter [7]. A challenging factor of this method, is that pinning of the contact line of the drop to the support plate also plays a role in how the drop deforms. The method would be associated with similar challenges as mentioned of the magnetic pendant drop method.

Magnetic Levitation capacity of novel electrode materials

The equilibrium height at which anodic graphite levitates in the given setup is limited, as was visualized in figure 6.4. Fortunately, novel electrode materials are being explored, such as porous silicon anodes that are being developed by E-magy. It would be interesting to explore the potential of these alternative materials to levitate in the MagLev setup, as compared to the conventional electrode materials, to assess which materials might be more easily separated.

Magnet design for gradient magnetic field uniform in height

One of the main challenges in scaling the setup into a continuous process, is generating a gradient magnetic field which is (approximately) uniform in height, such that the material can levitate through the setup at constant equilibrium height. In the patent by Polinder and Rem [61] such a magnet was designed for the purpose of MDS of plastic waste. Since the density of plastic is close to that of water, this application requires a weaker magnetic force than for battery materials. Thus, designing a similar method generating a much stronger field is a very challenging job. Besides configurations of permanent magnets, also superconducting magnets or electromagnets should be investigated for this purpose.

Flow chamber design

Another challenge related to continuous MDS, is maintaining a laminar flow regime. In the thesis of Dellaert [13] turbulence in a MDS application was studied, and design recommendations were given to prevent turbulence and mixing of particles. His thesis was also aimed towards MDS for plastic waste sorting, which concerns material of a morphology very different from that of BM. Therefore, it would be interesting to perform research into the behavior of BM particles in a continuous MDS as well, to determine the best flow regime to make sure the particles have enough time to settle to their equilibrium height, while also preventing turbulence.

Aggregation visualisation

Another challenge that is encountered in handling powder BM materials both dry and in water, is aggregation. At this point it remains unknown what mechanisms cause aggregation to take place, and to what extent aggregation of mixed anode and cathode materials occurs. Exploratory experiments were performed with an optical microscope, in which the movement of anodic graphite particles in water was

observed. Since the samples which could be observed under the microscope were of very small scale, several issues were encountered.

First, graphite particles in a sessile drop were observed. In this setup, the particles soon moved towards the edge and the surface of the drop, due to convection as a result of evaporation, and the hydrophobicity of the particles. Thus, this does not give a representative result for behavior of graphite particles in the bulk. Afterwards, graphite particles in a cuvette filled with water were observed. Nonetheless, an issue was encountered, as the larger particles sediment very rapidly to the bottom of the cuvette. This problem might be mitigated by using a medium of higher density than water.

It would be useful to better understand this mechanism for individual anode and cathode particles and a mix of both. By understanding the adhesion of particles, a method could be developed to better liberate the particles, which could improve separation efficiency for all hydromechanical separation methods.

Separation by sedimentation

Following the research by Van Rooijen [67], separation by sedimentation could also be further investigated. One limitation encountered in his research, was that only low volume fractions of BM could be used for sedimentation tracking, as the suspensions would become opaque at higher solid loadings, and thus the sedimentation could no longer be measured optically.

During this thesis work, MRI visualisation was used to track sedimentation of BM in water. From these preliminary experiments it was found that both anode and cathode materials could be identified in MRI measurements, and thus sedimentation experiments at higher solid loadings could be performed. The intensity plots of several measurements is shown in figure 7.3. The intensity represents the water concentration at the given location, and is thus the inverse of the graphite and/or cathode concentration. It should be noted that the bottom of the vial was a sharp point, in which much of the graphite remained stuck. Measurements of well-dispersed samples should be used to calibrate the solid concentration.

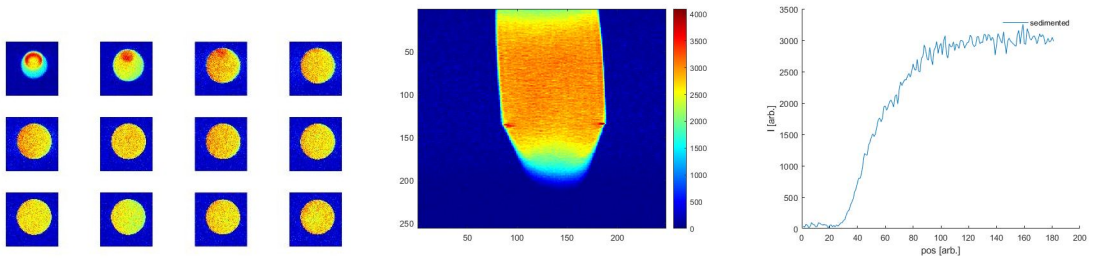

(a) Intensity plot of slices of graphite in $MnCl_2$ solution vial.

(b) Sideview intensity plot of graphite in $MnCl_2$ solution vial.

(c) Intensity as a function of height within the vial.

Figure 7.3: MRI intensity measurements, indicating the concentration of graphite at the given location.

Further, the battery materials used in the experiments were manually retrieved from a powerbank and further ground for different durations. Since this process does not correspond well to how BM is obtained in industry, it would be useful to perform sedimentation experiments with commercial BM. Not only sedimentation by gravity, but also by centrifugation can be performed, which offers better opportunities for a continuous process design.

Shaking table separation

Finally, a separation method is proposed, which is used in mineral processing: shaking table separation. This is a method that can easily be scaled up to continuous/industrial scale, and is used for concentration of heavy minerals, such as searching for gold. It can be applied on very fine particles, both wet and dry, but some limits exist regarding the particle sizes and ratios between densities which can be separated. Many sources [2, 5, 24, 45, 46, 73, 82] have investigated the opportunities and limitations of this method and how it can be optimized for several materials. It is recommended to apply their findings to research the applicability of this method for the separation of BM materials.

References

[1] IEA (2023). *Battery demand by region, 2016-2022*. 2023. URL: https://www.iea.org/data-and-statistics/charts/battery-demand-by-region-2016-2022.

[2] George Blankson Abaka-Wood et al. “A study of the feasibility of upgrading rare earth elements minerals from iron-oxide-silicate rich tailings using Knelson concentrator and Wilfley shaking table”. In: *Powder Technology* 344 (Feb. 15, 2019), pp. 897–913. ISSN: 0032-5910. DOI: 10.1016/j.powtec.2018.12.005. URL: https://www.sciencedirect.com/science/article/pii/S0032591018310428 (visited on 06/26/2024).

[3] Mozaffar Abdollahifar et al. “Graphite Recycling from End-of-Life Lithium-Ion Batteries: Processes and Applications”. In: *Advanced Materials Technologies* 8.2 (2023). _eprint: https://onlinelibrary.wiley.com/doi/pdf/1 p. 2200368. ISSN: 2365-709X. DOI: 10.1002/admt.202200368. URL: https://onlinelibrary.wiley.com/doi/abs/10.1002/admt.202200368 (visited on 01/25/2024).

[4] Jakob Asenbauer et al. “The success story of graphite as a lithium-ion anode material – fundamentals, remaining challenges, and recent developments including silicon (oxide) composites”. In: *Sustainable Energy & Fuels* 4.11 (2020). Publisher: Royal Society of Chemistry, pp. 5387–5416. DOI: 10.1039/D0SE00175A. URL: https://pubs.rsc.org/en/content/articlelanding/2020/se/d0se00175a (visited on 01/09/2024).

[5] Ata Bahrami and Seyed Mohammad Raouf Hosseini. *THE SHAKING TABLE CONCENTRATOR: INFLUENCE OF TABLE PARAMETERS ON MANGANESE SEPARATION*. Sept. 24, 2008.

[6] EJ Bakker, L Muchova, and PC Rem. “Separation of precious metals from MSWI bottom ash: 6th International Industrial Minerals Symposium Izmir”. In: *Proceedings of 6th International Industrial Minerals Symposium* (2007). Ed. by M.M. Odasi and Y. Kurulu. Place: s.l. Publisher: Altindag Grafik Matbaacilik, pp. 322–327. ISSN: 978-9944-89. URL: http://www.6iims.org/eng/default.asp (visited on 02/08/2024).

[7] Osman A. Basaran and Fred K. Wohlhuter. “Effect of nonlinear polarization on shapes and stability of pendant and sessile drops in an electric (magnetic) field”. In: *Journal of Fluid Mechanics* 244 (Nov. 1992), pp. 1–16. ISSN: 1469-7645, 0022-1120. DOI: 10.1017/S0022112092002945. URL: https://www.cambridge.org/core/journals/journal-of-fluid-mechanics/article/effect-of-nonlinear-polarization-on-shapes-and-stability-of-pendant-and-sessile-drops-in-an-electric-magnetic-field/0ED998A3D914B1BEDECCB431130839BF (visited on 08/22/2024).

[8] Emily Benson and Thibault Denamiel. “China’s New Graphite Restrictions”. In: (Oct. 23, 2023). URL: https://www.csis.org/analysis/chinas-new-graphite-restrictions (visited on 03/12/2024).

[9] Joseph D Berry. “Measurement of surface and interfacial tension using pendant drop tensiometry”. In: *Journal of Colloid and Interface Science* (2015).

[10] O. Beuf et al. “Magnetic Resonance Imaging for the Determination of Magnetic Susceptibility of Materials”. In: *Journal of Magnetic Resonance, Series B* 112.2 (Aug. 1, 1996), pp. 111–118. ISSN: 1064-1866. DOI: 10.1006/jmrb.1996.0120. URL: https://www.sciencedirect.com/science/article/pii/S106418669690120X (visited on 08/14/2024).

[11] Hugo Bouteiller, Mathieu Pasturel, and Pierric Lemoine. “On the Crystal Structures of the Polymorphs of Manganese(II) Chloride Tetrahydrate: α-MnCl2·4H2O and β-MnCl2·4H2O”. In: *Journal of Chemical Crystallography* 51.3 (Sept. 1, 2021), pp. 311–316. ISSN: 1572-8854. DOI: 10.1007/s10870-020-00856-z. URL: https://doi.org/10.1007/s10870-020-00856-z (visited on 07/08/2024).

[12] J. Červenka, M. I. Katsnelson, and C. F. J. Flipse. “Room-temperature ferromagnetism in graphite driven by two-dimensional networks of point defects”. In: *Nature Physics* 5.11 (Nov. 2009). Number: 11 Publisher: Nature Publishing Group, pp. 840–844. ISSN: 1745-2481. DOI: 10.1038/nphys1399. URL: https://www.nature.com/articles/nphys1399 (visited on 01/30/2024).

[13] Rik Anton Dellaert. “Turbulence and particle behavior in a magnetic density separation application: Studied with LDV, PIV & PTV”. ISBN: 9789038653860. PhD thesis. Eindhoven: Eindhoven University of Technology, Nov. 26, 2021.

[14] Erle C. Donaldson and Waqi Alam. *Wettability*. Google-Books-ID: EQ1BAQAAQBAJ. Elsevier, Nov. 25, 2013. 361 pp. ISBN: 978-0-12-799990-6.

[15] Shigeki Egami, Hideaki Monjushiro, and Hitoshi Watarai. “Magnetic Susceptibility Measurements of Solutions by Surface Nanodisplacement Detection”. In: *Analytical Sciences* 22.9 (Sept. 2006), pp. 1157–1162. ISSN: 0910-6340, 1348-2246. DOI: 10.2116/analsci.22.1157. URL: https://link.springer.com/10.2116/analsci.22.1157 (visited on 05/14/2024).

[16] Timothy W. Ellis and Joshua A. Montenegro. “Magnetic separation of electrochemical cell materials”. U.S. pat. 9156038B2. RSR Technologies Inc. Oct. 13, 2015. URL: https://patents.google.com/patent/US9156038B2/en (visited on 01/25/2024).

[17] P. Esquinazi et al. “Ferromagnetism in oriented graphite samples”. In: *Physical Review B* 66.2 (July 19, 2002). Publisher: American Physical Society, p. 024429. DOI: 10.1103/PhysRevB.66.024429. URL: https://link.aps.org/doi/10.1103/PhysRevB.66.024429 (visited on 01/30/2024).

[18] Richard P. Feynman, Robert B. Leighton, and Matthew Sands. *The Feynman Lectures on Physics, Volume II: Mainly Electromagnetism and Matter*. Sicth. Vol. II. United States of America: Basic Books, Feb. 1977.

[19] Fordham. *On the calculation of surface tension from measurements of pendant drops | Proceedings of the Royal Society of London. Series A. Mathematical and Physical Sciences*. URL: https://royalsocietypublishing.org/doi/10.1098/rspa.1948.0063 (visited on 07/12/2024).

[20] Linda Gaines. “Lithium-ion battery recycling processes: Research towards a sustainable course”. In: *Sustainable Materials and Technologies* 17 (Sept. 1, 2018), e00068. ISSN: 2214-9937. DOI: 10.1016/j.susmat.2018.e00068. URL: https://www.sciencedirect.com/science/article/pii/S2214993718300629 (visited on 01/24/2024).

[21] Shencheng Ge and George Whitesides. ““Axial” Magnetic Levitation Using Ring Magnets Enables Simple Density-Based Analysis, Separation, and Manipulation”. In: *Analytical Chemistry* 90 (Oct. 1, 2018). DOI: 10.1021/acs.analchem.8b03493.

[22] CIRS Group. *China Imposes Export Control Measures on Graphite Materials - Regulatory News - Chemicals - CIRS Group*. URL: https://www.cirs-group.com/en/chemicals/china-imposes-export-control-measures-on-graphite-materials (visited on 03/12/2024).

[23] Varun Gupta et al. “Direct recycling industrialization of Li-ion batteries: The pre-processing barricade”. In: *Next Energy* 2 (Jan. 1, 2024), p. 100091. ISSN: 2949-821X. DOI: 10.1016/j.nxener.2023.100091. URL: https://www.sciencedirect.com/science/article/pii/S2949821X2300090X (visited on 01/10/2024).

[24] Iwata H. et al. *Segregation or Demixing of Solid Particles on Inclined Vibrated Plates*. July 14, 1996.

[25] Yaqun He et al. “Recovery of LiCoO2 and graphite from spent lithium-ion batteries by Fenton reagent-assisted flotation”. In: *Journal of Cleaner Production* 143 (Feb. 1, 2017), pp. 319–325. ISSN: 0959-6526. DOI: 10.1016/j.jclepro.2016.12.106. URL: https://www.sciencedirect.com/science/article/pii/S0959652616321709 (visited on 01/22/2024).

[26] Thelma M. Herrington, Michael G. Roffey, and David P. Smith. “Densities of aqueous electrolytes manganese dichloride, cobalt dichloride, nickel dichloride, zinc chloride, and cadmium chloride from 25 to 75.degree.C at 1 atm”. In: *Journal of Chemical & Engineering Data* 31.2 (Apr. 1, 1986). Publisher: American Chemical Society, pp. 221–225. ISSN: 0021-9568. DOI: 10.1021/je00044a025. URL: https://doi.org/10.1021/je00044a025 (visited on 04/17/2024).

[27] *How do you calculate the magnetic flux density?* https://www.supermagnete.nl/eng/faq/How-do-you-calculate-the-magnetic-flux-density. Accessed: 2024-04-20.

[28] B. Hu. “Magnetic Density Separation of Polyolefin Wastes”. In: (2014). URL: https://repository.tudelft.nl/islandora/object/uuid%3A0c3717fa-8000-4de0-a938-d65605bf2a96 (visited on 02/07/2024).

[29] B. Hu, N. Fraunholz, and P. Rem. “Wetting Technologies for High-Accuracy Sink-Float Separations in Water- Based Media”. In: *The Open Waste Management Journal* 3.1 (Dec. 14, 2010). URL: https://benthamopen.com/ABSTRACT/TOWMJ-3-71 (visited on 02/06/2024).

[30] Bin Hu et al. “Recycling of WEEE by Magnetic Density Separation”. In: (2011).

[31] Zhicheng Hu et al. “High-intensity magnetic separation for recovery of LiFePO4 and graphite from spent lithium-ion batteries”. In: *Separation and Purification Technology* 297 (Sept. 15, 2022), p. 121486. ISSN: 1383-5866. DOI: 10.1016/j.seppur.2022.121486. URL: https://www.sciencedirect.com/science/article/pii/S1383586622010425 (visited on 01/10/2024).

[32] Zhe Huang et al. “A novel technology of recovering magnetic micro particles from spent lithium-ion batteries by ultrasonic dispersion and waterflow-magnetic separation”. In: *Resources, Conservation and Recycling* 164 (Jan. 1, 2021), p. 105172. ISSN: 0921-3449. DOI: 10.1016/j.resconrec.2020.105172. URL: https://www.sciencedirect.com/science/article/pii/S0921344920304894 (visited on 01/22/2024).

[33] Zhe Huang et al. “Characterization of the Materials in Waste Power Banks and the Green Recovery Process”. In: *ACS Sustainable Chemistry & Engineering* 6.3 (Mar. 5, 2018). Publisher: American Chemical Society, pp. 3815–3822. DOI: 10.1021/acssuschemeng.7b04175. URL: https://doi.org/10.1021/acssuschemeng.7b04175 (visited on 01/24/2024).

[34] Grinnell Jones and Wendell A. Ray. “The Surface Tension of Solutions of Electrolytes as a Function of the Concentration. I. A Differential Method for Measuring Relative Surface Tension”. In: *Journal of the American Chemical Society* 59.1 (Jan. 1937), pp. 187–198. ISSN: 0002-7863, 1520-5126. DOI: 10.1021/ja01280a048. URL: https://pubs.acs.org/doi/abs/10.1021/ja01280a048 (visited on 09/09/2024).

[35] Joonsoo Jun et al. “Optimal linear generator with Halbach array for harvesting of vibration energy during human walking”. In: *Advances in Mechanical Engineering* 8 (May 19, 2016). DOI: 10.1177/1687814016649880.

[36] Y. Kopelevich et al. “Ferromagnetic- and Superconducting-Like Behavior of Graphite”. In: *Journal of Low Temperature Physics* 119.5 (June 1, 2000), pp. 691–702. ISSN: 1573-7357. DOI: 10.1023/A:1004637814008. URL: https://doi.org/10.1023/A:1004637814008 (visited on 01/30/2024).

[37] Alexander Kraytsberg and Yair Ein-Eli. “Conveying Advanced Li-ion Battery Materials into Practice The Impact of Electrode Slurry Preparation Skills”. In: *Advanced Energy Materials* 6.21 (2016). _eprint: https://onlinelibrary.wiley.com/doi/pdf/10.1002/aenm.201600655, p. 1600655. ISSN: 1614-6840. DOI: 10.1002/aenm.201600655. URL: https://onlinelibrary.wiley.com/doi/abs/10.1002/aenm.201600655 (visited on 02/09/2024).

[38] Arno Kwade et al. “Current status and challenges for automotive battery production technologies”. In: *Nature Energy* 3.4 (2018). Publisher: Nature, pp. 290–300. URL: https://ideas.repec.org//a/nat/natene/v3y2018i4d10.1038_s41560-018-0130-3.html (visited on 01/12/2024).

[39] Jia Li, Guangxu Wang, and Zhenming Xu. “Environmentally-friendly oxygen-free roasting/wet magnetic separation technology for in situ recycling cobalt, lithium carbonate and graphite from spent LiCoO2/graphite lithium batteries”. In: *Journal of Hazardous Materials* 302 (Jan. 25, 2016), pp. 97–104. ISSN: 0304-3894. DOI: 10.1016/j.jhazmat.2015.09.050. URL: https://www.sciencedirect.com/science/article/pii/S0304389415301047 (visited on 01/22/2024).

[40] Jianlin Li, Claus Daniel, and David Wood. “Materials processing for lithium-ion batteries”. In: *Journal of Power Sources* 196.5 (Mar. 1, 2011), pp. 2452–2460. ISSN: 0378-7753. DOI: 10.1016/j.jpowsour.2010.11.001. URL: https://www.sciencedirect.com/science/article/pii/S037877531001904X (visited on 01/11/2024).

[41] D.R. Lide. *CRC Handbook of Chemistry and Physics, 89th Edition*. Taylor & Francis, 2008. ISBN: 9781420066791. URL: https://books.google.nl/books?id=KACWPwAACAAJ.

[42] Jiangshan Liu et al. “Recovery of LiCoO2 and graphite from spent lithium-ion batteries by cryogenic grinding and froth flotation”. In: *Minerals Engineering* 148 (Mar. 15, 2020), p. 106223. ISSN: 0892-6875. DOI: 10.1016/j.mineng.2020.106223. URL: https://www.sciencedirect.com/science/article/pii/S0892687520300431 (visited on 01/26/2024).

[43] Junjie Liu et al. “Critical strategies for recycling process of graphite from spent lithium-ion batteries: A review”. In: *Science of The Total Environment* 816 (Apr. 10, 2022), p. 151621. ISSN: 0048-9697. DOI: 10.1016/j.scitotenv.2021.151621. URL: https://www.sciencedirect.com/science/article/pii/S0048969721066973 (visited on 01/25/2024).

[44] Yangtao Liu et al. “Current and future lithium-ion battery manufacturing”. In: *iScience* 24.4 (Apr. 23, 2021), p. 102332. ISSN: 2589-0042. DOI: 10.1016/j.isci.2021.102332. URL: https://www.sciencedirect.com/science/article/pii/S258900422100300X (visited on 01/11/2024).

[45] Moghiseh M et al. “CONCENTRATION AND RECYCLING OF RARE EARTH ELEMENTS (REES) FROM IRON MINE WASTE USING A COMBINATION OF PHYSICAL SEPARATION METHODS”. In: 7.2 (Jan. 1, 2016). Publisher: JOURNAL OF MINING AND ENVIRONMENTAL (INTERNATIONAL JOURNAL OF MINING & ENVIRONMENTAL ISSUES), pp. 195–203. URL: https://www.sid.ir/paper/256355/fa (visited on 06/26/2024).

[46] R. J. Manser, R. W. Barley, and B. A. Wills. “The shaking table concentrator — The influence of operating conditions and table parameters on mineral separation — The development of a mathematical model for normal operating conditions”. In: *Minerals Engineering* 4.3 (Jan. 1, 1991), pp. 369–381. ISSN: 0892-6875. DOI: 10.1016/0892-6875(91)90142-I. URL: https://www.sciencedirect.com/science/article/pii/089268759190142I (visited on 06/26/2024).

[47] Arumugam Manthiram, Bohang Song, and Wangda Li. “A perspective on nickel-rich layered oxide cathodes for lithium-ion batteries”. In: *Energy Storage Materials* 6 (Jan. 1, 2017), pp. 125–139. ISSN: 2405-8297. DOI: 10.1016/j.ensm.2016.10.007. URL: https://www.sciencedirect.com/science/article/pii/S2405829716302112 (visited on 01/11/2024).

[48] Fabio Maroni et al. “Near-Zero Volume Expansion Nanoporous Silicon as Anode for Li-ion Batteries”. In: *Journal of The Electrochemical Society* 169.8 (Aug. 1, 2022), p. 080506. ISSN: 0013-4651, 1945-7111. DOI: 10.1149/1945-7111/ac8628. URL: https://iopscience.iop.org/article/10.1149/1945-7111/ac8628 (visited on 10/15/2024).

[49] Yanio E. Milian et al. “A comprehensive review of emerging technologies for recycling spent lithium-ion batteries”. In: *Science of The Total Environment* 910 (Feb. 1, 2024), p. 168543. ISSN: 0048-9697. DOI: 10.1016/j.scitotenv.2023.168543. URL: https://www.sciencedirect.com/science/article/pii/S0048969723071711 (visited on 01/24/2024).

[50] Katherine A. Mirica et al. “Measuring Densities of Solids and Liquids Using Magnetic Levitation: Fundamentals”. In: *Journal of the American Chemical Society* 131.29 (July 29, 2009). Publisher: American Chemical Society, pp. 10049–10058. ISSN: 0002-7863. DOI: 10.1021/ja900920s. URL: https://doi.org/10.1021/ja900920s (visited on 02/06/2024).

[51] O. Miura, K. Yamagishi, and D. Yamamoto. “Magneto-Archimedes levitation of precious metals under a high magnetic field gradient”. In: *Journal of Physics: Conference Series* 1054.1 (July 2018). Publisher: IOP Publishing, p. 012086. ISSN: 1742-6596. DOI: 10.1088/1742-6596/1054/1/012086. URL: https://dx.doi.org/10.1088/1742-6596/1054/1/012086 (visited on 02/15/2024).

[52] A. W. Mombrú et al. “Multilevel ferromagnetic behavior of room-temperature bulk magnetic graphite”. In: *Physical Review B* 71.10 (Mar. 11, 2005). Publisher: American Physical Society, p. 100404. DOI: 10.1103/PhysRevB.71.100404. URL: https://link.aps.org/doi/10.1103/PhysRevB.71.100404 (visited on 01/30/2024).

[53] Bahar Moradi and Gerardine G. Botte. “Recycling of graphite anodes for the next generation of lithium ion batteries”. In: *Journal of Applied Electrochemistry* 46.2 (Feb. 1, 2016), pp. 123–148. ISSN: 1572-8838. DOI: 10.1007/s10800-015-0914-0. URL: https://doi.org/10.1007/s10800-015-0914-0 (visited on 01/09/2024).

[54] Kazuhiko Mukai and Takao Inoue. “Magnetic susceptibility measurements on Li-intercalated graphite: Paramagnetic to diamagnetic transitions in C12Li induced by magnetic field”. In: *Carbon* 123 (Oct. 1, 2017), pp. 645–650. ISSN: 0008-6223. DOI: 10.1016/j.carbon.2017.08.012. URL: https://www.sciencedirect.com/science/article/pii/S0008622317307984 (visited on 01/29/2024).

[55] Manuel Mundszinger et al. “Morphology and texture of spheroidized natural and synthetic graphites”. In: *Carbon* 111 (Jan. 1, 2017), pp. 764–773. ISSN: 0008-6223. DOI: 10.1016/j.carbon.2016.10.060. URL: https://www.sciencedirect.com/science/article/pii/S0008622316309228 (visited on 03/08/2024).

[56] V. Murariu, J. Svoboda, and P. Sergeant. “The modelling of the separation process in a ferrohydrostatic separator”. In: *Minerals Engineering* 18.4 (Apr. 1, 2005), pp. 449–457. ISSN: 0892-6875. DOI: 10.1016/j.mineng.2004.06.015. URL: https://www.sciencedirect.com/science/article/pii/S0892687504001669 (visited on 02/08/2024).

[57] Seung-Taek Myung et al. “Nickel-Rich Layered Cathode Materials for Automotive Lithium-Ion Batteries: Achievements and Perspectives”. In: *ACS Energy Letters* 2.1 (Jan. 13, 2017). Publisher: American Chemical Society, pp. 196–223. DOI: 10.1021/acsenergylett.6b00594. URL: https://doi.org/10.1021/acsenergylett.6b00594 (visited on 03/05/2024).

[58] J. Oberteuffer. “Magnetic separation: A review of principles, devices, and applications”. In: *IEEE Transactions on Magnetics* 10.2 (June 1974). Conference Name: IEEE Transactions on Magnetics, pp. 223–238. ISSN: 1941-0069. DOI: 10.1109/TMAG.1974.1058315. URL: https://ieeexplore.ieee.org/abstract/document/1058315 (visited on 01/22/2024).

[59] K. Ohzeki et al. “Shape modification of graphite particles by rotational impact blending”. In: *Carbon* 43.8 (July 1, 2005), pp. 1673–1679. ISSN: 0008-6223. DOI: 10.1016/j.carbon.2005.02.007. URL: https://www.sciencedirect.com/science/article/pii/S0008622305000977 (visited on 03/11/2024).

[60] Marek Pawlik. “Fundamentals of froth flotation”. In: *ChemTexts* 8.4 (Oct. 18, 2022), p. 19. ISSN: 2199-3793. DOI: 10.1007/s40828-022-00170-5. URL: https://doi.org/10.1007/s40828-022-00170-5 (visited on 03/01/2024).

[61] Hendrik Polinder and Peter Carlo Rem. “Magnet and device for magnetic density separation”. European pat. 2978535A1. Urban Mining Corp BV. Feb. 3, 2016. URL: https://patents.google.com/patent/EP2978535A1/en (visited on 06/10/2024).

[62] S. Ramachandra Rao. *Surface Chemistry of Froth Flotation: Volume 1: Fundamentals*. Google-Books-ID: FqrTBwAAQBAJ. Springer Science & Business Media, June 29, 2013. 793 pp. ISBN: 978-1-4757-4302-9.

[63] Joseph A. Rard and Donald G. Miller. “Densities and apparent molal volumes of aqueous manganese, cadmium, and zinc chlorides at 25.degree.C”. In: *Journal of Chemical & Engineering Data* 29.2 (Apr. 1984), pp. 151–156. ISSN: 0021-9568, 1520-5134. DOI: 10.1021/je00036a016. URL: https://pubs.acs.org/doi/abs/10.1021/je00036a016 (visited on 06/17/2024).

[64] Carlo Rigoni et al. “Division of Ferrofluid Drops Induced by a Magnetic Field”. In: *Langmuir* 34.33 (Aug. 21, 2018). Publisher: American Chemical Society, pp. 9762–9767. ISSN: 0743-7463. DOI: 10.1021/acs.langmuir.8b02399. URL: https://doi.org/10.1021/acs.langmuir.8b02399 (visited on 08/22/2024).

[65] *RMIS - Battery supply chain challenges*. RMIS - Raw Materials Information System. URL: https://rmis.jrc.ec.europa.eu/analysis-of-supply-chain-challenges-49b749 (visited on 01/31/2024).

[66] Abel van Rooijen. “Separation of anode material from black mass of spent lithium-ion batteries”. In: ().

[67] Abel van Rooijen. “Towards Circular Batteries: Investigating Particle Size-Based Separation of Active Materials from spent Li-ion batteries”. In: ().

[68] *Safety Data Sheet*. 328146. Version 7.3. Sigma-Aldrich. Mar. 2024.

[69] Aliza Marie Salces et al. “Joint recovery of graphite and lithium metal oxides from spent lithium-ion batteries using froth flotation and investigation on process water re-use”. In: *Minerals Engineering* 184 (June 30, 2022), p. 107670. ISSN: 0892-6875. DOI: 10.1016/j.mineng.2022.107670. URL: https://www.sciencedirect.com/science/article/pii/S0892687522002801 (visited on 03/29/2024).

[70] Silvia Serranti et al. “An innovative recycling process to obtain pure polyethylene and polypropylene from household waste”. In: *Waste Management* 35 (Jan. 1, 2015), pp. 12–20. ISSN: 0956-053X. DOI: 10.1016/j.wasman.2014.10.017. URL: https://www.sciencedirect.com/science/article/pii/S0956053X14005017 (visited on 02/06/2024).

[71] Hammad Al-Shammari and Siamak Farhad. “Heavy liquids for rapid separation of cathode and anode active materials from recycled lithium-ion batteries”. In: *Resources, Conservation and Recycling* 174 (Nov. 1, 2021), p. 105749. ISSN: 0921-3449. DOI: 10.1016/j.resconrec.2021.105749. URL: https://www.sciencedirect.com/science/article/pii/S092134492100358X (visited on 01/26/2024).

[72] Roberto Sommerville et al. “A review of physical processes used in the safe recycling of lithium ion batteries”. In: *Sustainable Materials and Technologies* 25 (Sept. 1, 2020), e00197. ISSN: 2214-9937. DOI: 10.1016/j.susmat.2020.e00197. URL: https://www.sciencedirect.com/science/article/pii/S2214993719303501 (visited on 01/25/2024).

[73] G. G. Tarnekar and K. Ravindranath. “Recovery of Economic Minerals from Graphite Float of Rajpura Dariba mines”. In: ed. by P. Bhattacharyya et al. Num Pages: 306. Jamshedpur: NML Jamshedpur, 1997, pp. 57–63. ISBN: 978-81-87053-25-5. URL: https://eprints.nmlindia.org/2863/ (visited on 06/27/2024).

[74] N. Traore and S. Kelebek. “Characteristics of Spent Lithium Ion Batteries and Their Recycling Potential Using Flotation Separation: A Review”. In: *Mineral Processing and Extractive Metallurgy Review* 44.3 (Apr. 3, 2023). Publisher: Taylor & Francis _eprint: https://doi.org/10.1080/08827508.2022.2040497, pp. 231–259. ISSN: 0882-7508. DOI: 10.1080/08827508.2022.2040497. URL: https://doi.org/10.1080/08827508.2022.2040497 (visited on 01/11/2024).

[75] Anna Vanderbruggen et al. “A contribution to understanding the flotation behavior of lithium metal oxides and spheroidized graphite for lithium-ion battery recycling”. In: *Colloids and Surfaces A: Physicochemical and Engineering Aspects* 626 (Oct. 5, 2021), p. 127111. ISSN: 0927-7757. DOI: 10.1016/j.colsurfa.2021.127111. URL: https://www.sciencedirect.com/science/article/pii/S0927775721009808 (visited on 03/04/2024).

[76] Anna Vanderbruggen et al. “Improving Separation Efficiency in End-of-Life Lithium-Ion Batteries Flotation Using Attrition Pre-Treatment”. In: *Minerals* 12 (Jan. 6, 2022). DOI: 10.3390/min12010072.

[77] Anna Vanderbruggen et al. “Lithium-Ion Battery Recycling–Influence of Recycling Processes on Component Liberation and Flotation Separation Efficiency”. In: *ACS ES&T Engineering* 2.11 (Nov. 11, 2022). Publisher: American Chemical Society, pp. 2130–2141. DOI: 10.1021/acsestengg.2c00177. URL: https://doi.org/10.1021/acsestengg.2c00177 (visited on 03/05/2024).

[78] Valentin Wenzel, Hermann Nirschl, and Dorit Nötzel. “Challenges in Lithium-Ion-Battery Slurry Preparation and Potential of Modifying Electrode Structures by Different Mixing Processes”. In: *Energy Technology* 3.7 (2015). _eprint: https://onlinelibrary.wiley.com/doi/pdf/10.1002/ente.201402218, pp. 692–698. ISSN: 2194-4296. DOI: 10.1002/ente.201402218. URL: https://onlinelibrary.wiley.com/doi/abs/10.1002/ente.201402218 (visited on 01/11/2024).

[79] D. WILLIAM, D. HARKINS, and F.-E. BROWN. “The Determination of surface tension (free surface energy), and the weight of falling drops: the surface tension of water and benzene by the capillary height method”. In: (1919), vol. 41 (no 4), pp. 499–524.

[80] Biwei Xiao and Xueliang Sun. “Surface and Subsurface Reactions of Lithium Transition Metal Oxide Cathode Materials: An Overview of the Fundamental Origins and Remedying Approaches”. In: *Advanced Energy Materials* 8.29 (2018). _eprint: https://onlinelibrary.wiley.com/doi/pdf/10.1002/aenm.201802057, p. 1802057. ISSN: 1614-6840. DOI: 10.1002/aenm.201802057. URL: https://onlinelibrary.wiley.com/doi/abs/10.1002/aenm.201802057 (visited on 03/05/2024).

[81] Xinmei Yang et al. “Correlation between the vacancy defects and ferromagnetism in graphite”. In: *Carbon* 47.5 (Apr. 1, 2009), pp. 1399–1406. ISSN: 0008-6223. DOI: 10.1016/j.carbon.2009.01.032. URL: https://www.sciencedirect.com/science/article/pii/S0008622309000505 (visited on 01/30/2024).

[82] Keshun You and Huizhong Liu. “Research on optimization of control parameters of gravity shaking table”. In: *Scientific Reports* 13.1 (Jan. 20, 2023). Publisher: Nature Publishing Group, p. 1133. ISSN: 2045-2322. DOI: 10.1038/s41598-023-28171-5. URL: https://www.nature.com/articles/s41598-023-28171-5 (visited on 06/26/2024).

[83] Jiadong Yu et al. “A promising physical method for recovery of LiCoO2 and graphite from spent lithium-ion batteries: Grinding flotation”. In: *Separation and Purification Technology* 190 (Jan. 8, 2018), pp. 45–52. ISSN: 1383-5866. DOI: 10.1016/j.seppur.2017.08.049. URL: https://www.sciencedirect.com/science/article/pii/S1383586617320178 (visited on 01/25/2024).

[84] Jiadong Yu et al. “Effect of the secondary product of semi-solid phase Fenton on the flotability of electrode material from spent lithium-ion battery”. In: *Powder Technology* 315 (June 15, 2017), pp. 139–146. ISSN: 0032-5910. DOI: 10.1016/j.powtec.2017.03.050. URL: https://www.sciencedirect.com/science/article/pii/S0032591017302668 (visited on 02/05/2024).

[85] Ruiting Zhan and Lei Pan. “A cycling-insensitive recycling method for producing lithium transition metal oxide from Li-ion batteries using centrifugal gravity separation”. In: *Sustainable Materials and Technologies* 32 (July 1, 2022), e00399. ISSN: 2214-9937. DOI: 10.1016/j.susmat.2022.e00399. URL: https://www.sciencedirect.com/science/article/pii/S2214993722000136 (visited on 02/07/2024).

[86] Guangwen Zhang et al. “Pyrolysis-Ultrasonic-Assisted Flotation Technology for Recovering Graphite and LiCoO2 from Spent Lithium-Ion Batteries”. In: *ACS Sustainable Chemistry & Engineering* 6.8 (Aug. 6, 2018). Publisher: American Chemical Society, pp. 10896–10904. DOI: 10.1021/acssuschemeng.8b02186. URL: https://doi.org/10.1021/acssuschemeng.8b02186 (visited on 01/26/2024).

[87] Guangwen Zhang et al. “Recycling of electrode materials from spent lithium-ion battery by pyrolysis-assisted flotation”. In: *Journal of Environmental Chemical Engineering* 9.6 (Dec. 1, 2021), p. 106777. ISSN: 2213-3437. DOI: 10.1016/j.jece.2021.106777. URL: https://www.sciencedirect.com/science/article/pii/S2213343721017541 (visited on 02/05/2024).

[88] Tao Zhang et al. “Characteristics of wet and dry crushing methods in the recycling process of spent lithium-ion batteries”. In: *Journal of Power Sources* 240 (Oct. 15, 2013), pp. 766–771. ISSN: 0378-7753. DOI: 10.1016/j.jpowsour.2013.05.009. URL: https://www.sciencedirect.com/science/article/pii/S0378775313007866 (visited on 03/01/2024).

[89] Yu Zhang et al. “Application of Falcon centrifuge in the recycling of electrode materials from spent lithium ion batteries”. In: *Journal of Cleaner Production* 202 (Nov. 20, 2018), pp. 736–747. ISSN: 0959-6526. DOI: 10.1016/j.jclepro.2018.08.133. URL: https://www.sciencedirect.com/science/article/pii/S0959652618324776 (visited on 01/22/2024).

[90] Yanyan Zhao et al. “A Review on Battery Market Trends, Second-Life Reuse, and Recycling”. In: *Sustainable Chemistry* 2.1 (Mar. 2021). Number: 1 Publisher: Multidisciplinary Digital Publishing Institute, pp. 167–205. ISSN: 2673-4079. DOI: 10.3390/suschem2010011. URL: https://www.mdpi.com/2673-4079/2/1/11 (visited on 01/31/2024).

[91] Xuehu Zhong et al. “Pyrolysis and physical separation for the recovery of spent LiFePO4 batteries”. In: *Waste Management* 89 (Apr. 15, 2019), pp. 83–93. ISSN: 0956-053X. DOI: 10.1016/j.wasman.2019.03.068. URL: https://www.sciencedirect.com/science/article/pii/S0956053X19302119 (visited on 02/05/2024).

A

Results XRD and XRF measurements $MnCl_2$ beads and sediment from suspension

X-RAY FACILITIES GROUP

Dr. Amarante Böttger

Dhr. Ruud Hendrikx
Drs. Richard Huizenga

Delft University of Technology, Faculty of ME
Department of Materials Science and Engineering
Mekelweg 2, NL-2628 CD Delft, the Netherlands, phone +31(0)152789459

XRD identification of $MnCl_2$ powders

Author	:	Ruud Hendrikx
Date	:	05 july 2024
Researcher	:	Irene Hooijkaas, ME
Research question	:	Phase identification

"Project on the separation of anode and cathode materials from spent battery materials".

Samples
The samples are solid beads (straight from the jar and slurry remaining after centrifugation or filtering, see figure 1.

Specimens
A thin layer of powdered material was deposited on a Si510 zero-background wafer in holder SP52.

Experimental
Instrument: Bruker D8 Advance diffractometer Bragg-Brentano geometry with graphite monochromator and Vantec position sensitive detector. Co Kα radiation. Divergence slit V20mm, scatter screen height 9 mm, 40 kV 40 mA.

Measurement
Coupled θ -2θ scan 10° - 110°, step size 0.04° 2θ, counting time per step 4 s.
Sample spinning 30rpm.

Data evaluation
Bruker software DiffracSuite.EVA vs 7.1.

.

Results

Figures 2 and 3 show the measured XRD patterns, after background subtraction and displacement correction. The colored sticks give the peak positions and intensities of the possibly present phases, using the ICDD pdf5 database.

In the pattern of the slurry deposits two small peaks are present that could not be identified.

sample	*compound*	
beads	kappa-Manganese dichloride tetrahydrate	$MnCl_2(H_2O)4$
slurry deposits	kappa-Manganese dichloride tetrahydrate	$MnCl_2(H_2O)4$

Table 1.

Figures

Figure 1 beads slurry deposits

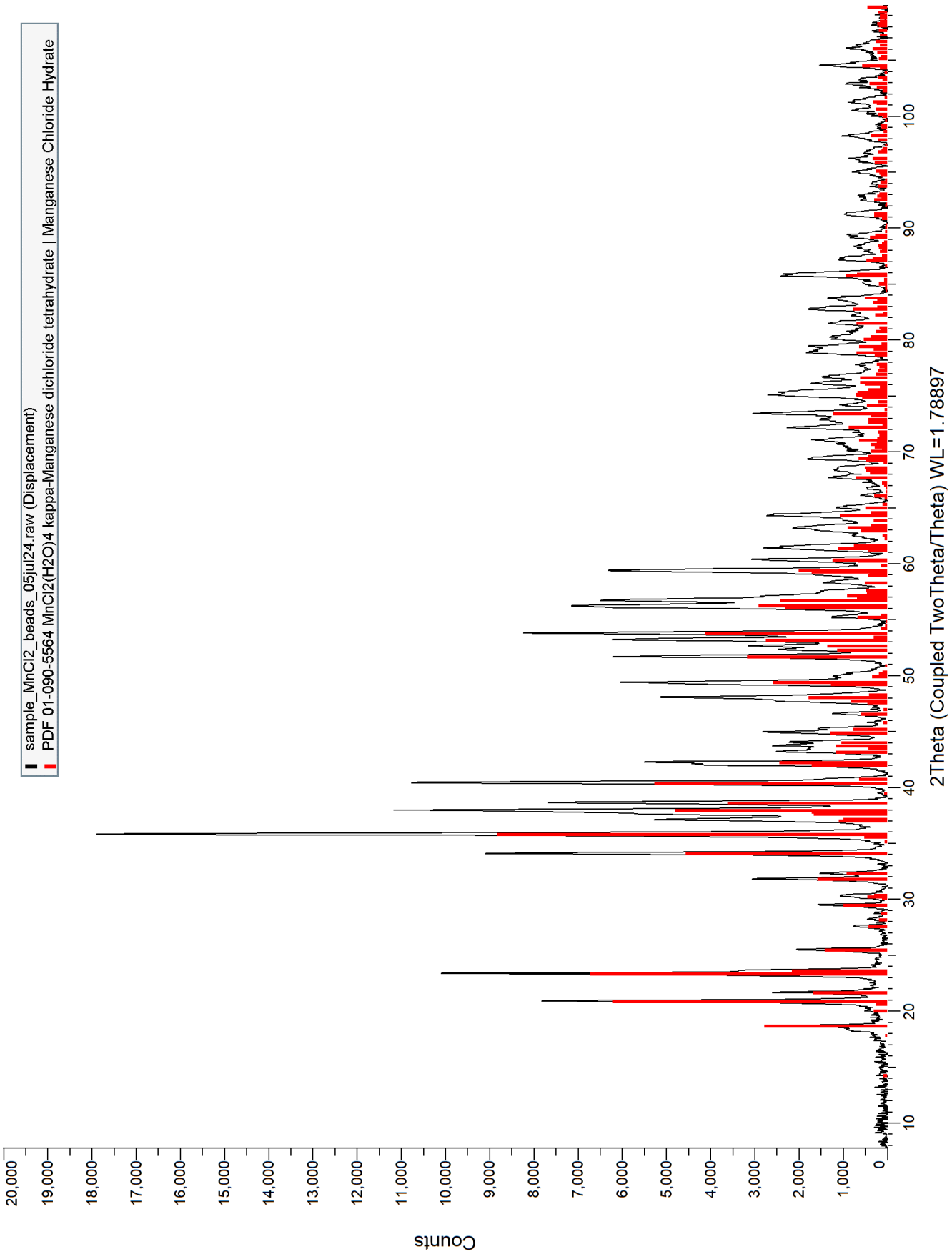

Figure 2 XRD pattern sample " $MnCl_2$-beads"

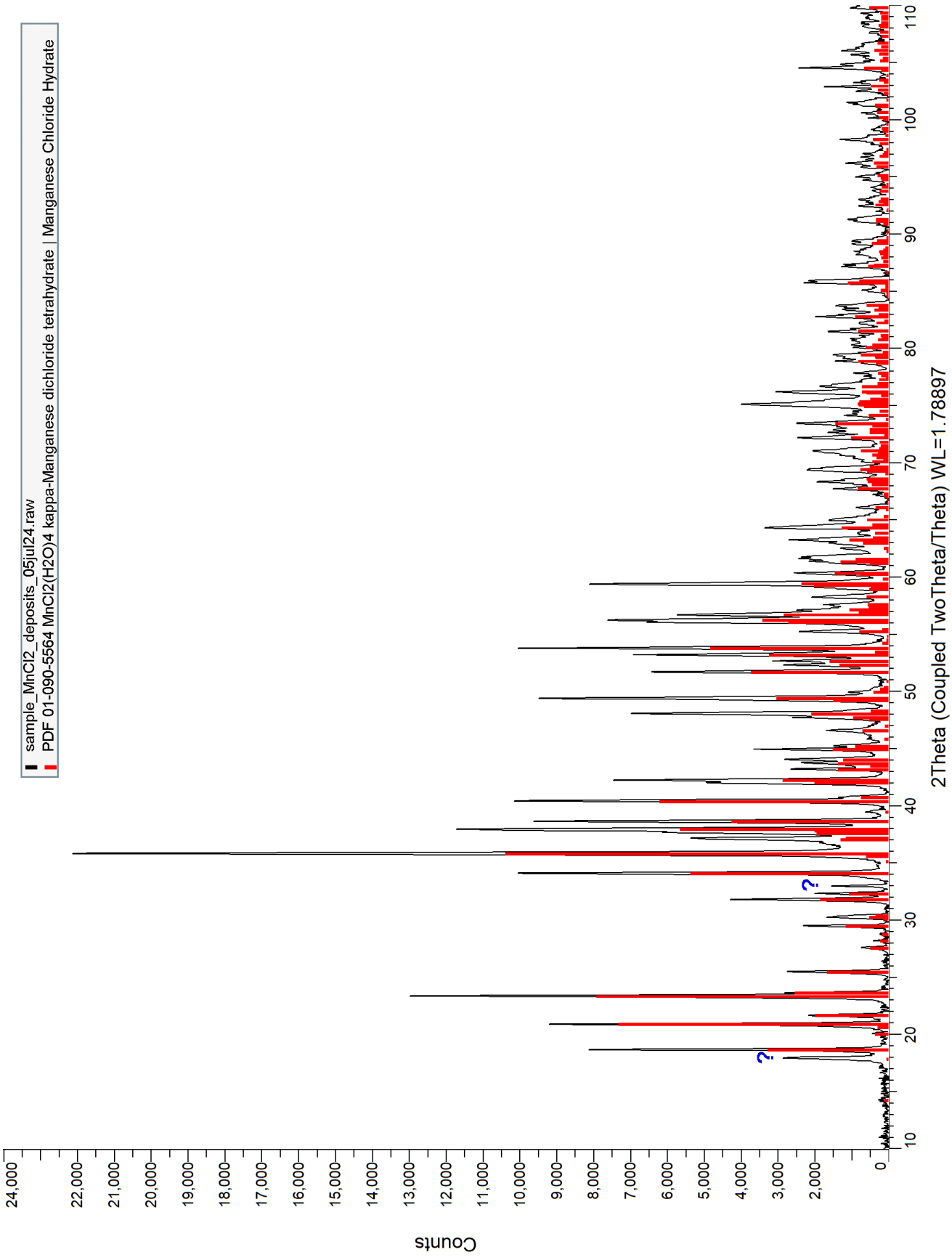

Figure 3 XRD pattern sample " MnC_{l2} slurry deposits "

Materials Science and Engineering
TUDelft, Faculty of 3mE
Mekelweg 2
2628 CD Delft, The Netherlands
Tel:015-2789459
Email: R.W.A.Hendrikx@tudelft.nl

X- ray diffraction facilities

Experimental conditions:

For XRF analysis the measurements were performed with a Panalytical Axios Max WD-XRF spectrometer and data evaluation was done with SuperQ5.0i/Omnian software. 18/12/2015 09:37:03

7/5/2024 10:57:16 AM

PANalytical

I. Hooijkaas, Quantification of sample "MnCl2 deposits", 05jul24

Sum before normalization: 66.7 wt%

Normalised to: 100.0 wt%

Sample type: Loose powder

Correction applied for medium: Yes

Correction applied for film: Yes

Results database: omnian 4kw 27he

Results database in: c:\panalytical\superq\userdata

	Compound Name	Conc. (wt%)	Absolute Error (wt%)
1	Cl	51.573	0.1
2	Mn	48.071	0.2
3	K	0.176	0.01
4	Ba	0.077	0.008
5	Ca	0.044	0.006
6	Si	0.038	0.006
7	S	0.015	0.004
8	Sr	0.007	0.002

7/5/2024 11:28:38 AM

PANalytical

I. Hooijkaas: Quantification of sample "MnCl2 beads", 05jul24

Sum before normalization: 84.5 wt%

Normalised to: 100.0 wt%

Sample type: Loose powder

Correction applied for medium: Yes

Correction applied for film: Yes

Results database: omnian 4kw 27he

Results database in: c:\panalytical\superq\userdata

	Compound Name	Conc. (wt%)	Absolute Error (wt%)
1	Cl	57.558	0.1
2	Mn	41.645	0.1
3	K	0.394	0.02
4	Fe	0.248	0.01
5	Ba	0.057	0.007
6	Ca	0.052	0.007
7	Si	0.029	0.005
8	Sr	0.014	0.004
9	S	0.005	0.002

Use of our XRD or XRF analysis:
In a publication: 'PersonX at the Department of Materials Science and Engineering of the Delft University of Technology is acknowledged for the X-ray analysis. If it is an important part of the publication: a co-authorship is preferred. It is useful to involve us in the preparation of any presentation!

B

interfacial tension (IFT) results

This appendix shows plots the results of the 'interfacial tension' as taken from opendrop for all concentrations. As the drop grows, the IFT value increases until it plateaus at its actual value.

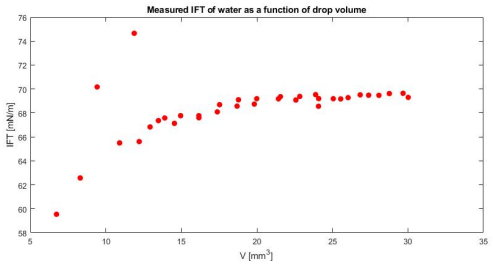

(a) Sample water.

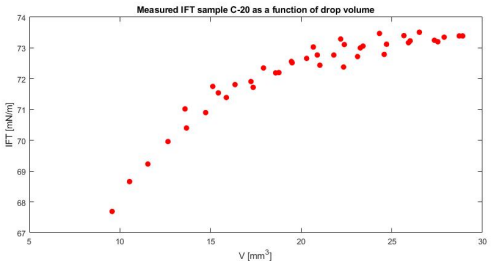

(b) Sample C-20.

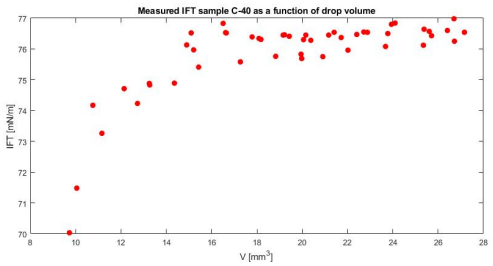

(c) Sample C-40.

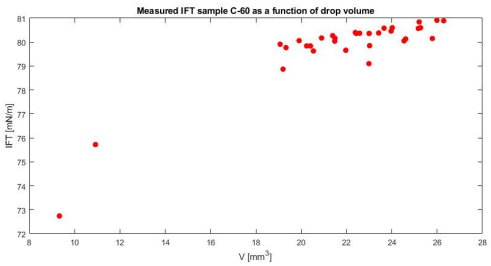

(d) Sample C-60.

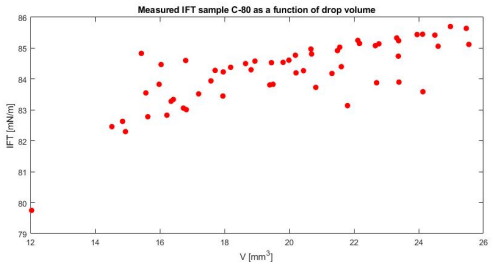

(e) Sample C-80.

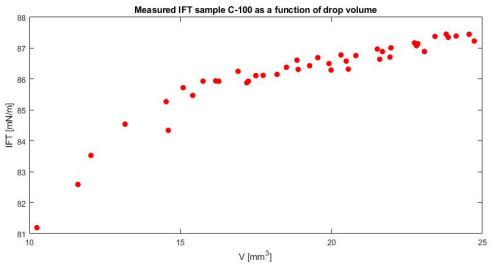

(f) Sample C-100.

Figure B.1: IFT plots of different samples from pendant drop experiments.